A COMPARISON OF STRAIN GRADIENT AND CONVENTIONAL PLASTICITY THEORIES FOR THEIR APPLICATION TO SURFACE TEXTURING

A COMPARISON OF STRAIN GRADIENT AND CONVENTIONAL PLASTICITY THEORIES FOR THEIR APPLICATION TO SURFACE TEXTURING

By

JING PENG, B.A., M.S.

A Thesis Submitted to the School of Graduate Studies in

Conformity with the Requirements for the Degree of

Master of Applied Science

McMaster University

Master of Applied Science (2012), Mechanical Engineering, McMaster University, Canada

Master of Science (2007), Engineering Mechanics, Tsinghua University, China

Bachelor of Science (2004), Engineering Mechanics, Tsinghua University, China

TITLE: A comparison of strain gradient and conventional plasticity theories and their application to surface texturing

AUTHOR: Jing Peng, B.A., M.S.

SUPERVISOR: Professor Peidong Wu

NUMBER OF PAGES: xv, 102

Abstract

There have been considerable requirements for improved products of sheet metal in automobile industry. A quick and economical route to new products is to design novel surface textures of varying scales for improved product enhancement in better optical appearance and formability. The critical deformation in the surface texturing is on the order of only a few microns, and can not be accurately predicted by the classical plasticity due to the size effect. The theory of strain gradient plasticity has been developed to capture the size effect based on the concept of geometrically necessary dislocations (GNDs). A selected strain gradient theory has been implemented into the finite element (FE) model to simulate the surface texturing process. We developed a 3D FE model to simulate the rolling process of sheet metal which has band-type feature on the original surface. The numerical results show that a textured roller can efficiently modify the band-type feature without changing the whole mechanical property of the sheet. Size effect has significant contribution to the magnitude of the rolling force. We also developed a FE model to simulate the tensile test of the sheet with textured surface. A textured surface of the sheet is prepared through the indention on the sheet surface. The results show that the textured surface becomes harder due to the strain gradient effect, and finally improves the formability of the sheet.

Acknowledgments

I would like to thank my supervisor Professor Peidong Wu for allowing me to complete this study; I am grateful for his support and guidance throughout the past five years. I would like to thank Professor Jain for plenty of helpful suggestion to my thesis. Also, I would like to thank Dr. Huamiao Wang who was always available to help and for discussion regardless of the time or day.

I would like to thank my parents who encouraged me to insist on the research when I met difficulties.

Finally, I would like to thank my many lab colleagues who were always very supportive and made my graduate experience memorable.

Table of Contents

List of Figures

List of Symbols

H indentation hardness

H_0 indentation hardness at large indentation depth

h indentation depth

h^* characteristic length of the material

R_{rms} root mean square roughness

R_a average surface roughness

f_s thermodynamic surface stress

e_c dissipation energy per contact project area

k , g parameters related to indenter geometry

ε_{ij} strain tensor

η_{ijk} strain gradient tensor

$\delta\varepsilon_{ij}$ strain increment

$\delta\eta_{ijk}$ strain gradient increment

ξ overall effective strain

ε_e the second invariant of strain

$\dot{\varepsilon}_{ij}^{e}$ elastic strain rate

$\dot{\varepsilon}_{ij}^{p}$ plastic strain rate

$\dot{\varepsilon}^{p}$ equivalent plastic strain rate

$\dot{\varepsilon}_{ij}'$ deviatoric strain rate

$\bar{\varepsilon}_{ij}$ strain tensor at micro-scale

d^{p} effective strain rate

E^{e} elastic strain

H^{p} plastic strain

E^{P} plastic stretching

Ω^{p} plastic rotation

η effective strain gradient

χ_e the second invariant of the curvature

η^S symmetric part of η

$\eta^{(1)}, \eta^{(2)}, \eta^{(3)}$ components of strain gradient tensor

σ_{ij} Cauchy stress tensor

τ_{ijk} higher-order stress tensor

$\overline{\sigma}_{ij}$ stress tensor at micro-scale

$\overline{\sigma}'_{ij}$ deviatoric part of stress $\overline{\sigma}_{ij}$

σ'_{ij} deviatoric part of stress σ_{ij}

σ_{e} von Mises effective stress

σ_{flow} flow stress

σ_{Y} initial yield stress

T stress

S microscopic stress

$\sigma^{\mathrm{E}}, \tau^{\mathrm{E}}$ energetic stresses

$\sigma^{\mathrm{D}}, \tau^{\mathrm{D}}$ dissipative stresses

w strain energy density

δw work increment per unit volume

D_j surface gradient operator

f_k body force per unit volume

t_k surface traction

r_k double stress traction

χ_{ip} curvature tensor

$\theta_{i,p}$ spatial gradient of material rotation

κ constant (larger than zero)

c_1, c_2, c_3 constants to scale the three quadratic invariants for η_{ijk}

e_{ijk} , η_{ij} permutation tensor

l_1, l_2, l_3 constitutive length

b magnitude of the Burgers vector

f non-dimensional function of plastic strain ε^p

α empirical coefficient

ρ_{T} total dislocation density

ρ_{S} density of statistically stored dislocations

ρ_{G} density of geometrically necessary dislocations

μ shear modulus

K bulk modulus

m rate-sensitivity exponent

n work hardening exponent

N number of indentations

ϕ energy potential

η^{p} effective plastic strain gradient

$\bar{r}$ Nye factor

l_{ε} cell size

ψ free energy potential

β a constant (larger than 1)

l intrinsic material length

M Taylor factor

L_{yield} mean spacing between statistically stored dislocations at yielding

Chapter 1: Introduction

There has been considerable societal and government legislative pressure on the North American automotive producers to reduce the fuel consumption and exhaust gas emissions from vehicles. One of the most effective ways to achieve this is by the weight reduction that can be obtained by replacing steel with aluminum, magnesium or advanced high strength steel in the vehicle structure and body panels. However, these materials have a number of perceived and real technological limitations. It is believed that this could be eliminated by the development of improved materials, or must be circumvented by the development of new application methods, so that they can be used effectively in the volume manufacturing of reduced weight automobiles.

A quick and economical route to new products is to design novel surface textures of varying scales for improved product enhancement in better optical appearance and formability. The critical deformation mechanism in the surface texturing is at a length scale of only a few microns. Experiments have shown that materials display strong size effects when the characteristic length scale associated with non-uniform plastic deformation is in the order of microns. The classical plasticity theories cannot predict the size dependence of material behaviour at the micron scale because their constitutive models possess no internal length scale. The current design tools, such as finite element analysis (FEA) and computer aided design (CAD), are based on classical continuum theories, which are not suitable at such a small length scale. On the other hand, it is still not possible to perform quantum and atomistic simulations on realistic time and length scales required for the micron level structures. Improved continuum plasticity models for micron level applications, or strain

gradient plasticity theories, have been thus developed to bridge the gap between classic continuum theories and atomistic simulations.

1.1 Size effect observed in experiment: nano-indentation

The size effect has been observed in various experiments, such as the micro/nano indentation test which shows an increase in hardness with decreasing in indentation depth. Nix and Gao (1998) established a linear relation between micro-indentation hardness H^2 and the reciprocal of indentation depth $1/h$, i.e.,

$$(H/H_0)^2 = 1 + h^*/h \qquad (1)$$

where H_0 is the indentation hardness for a large indentation depth, h^* is a characteristic length dependent on the indenter shape and material prosperities.

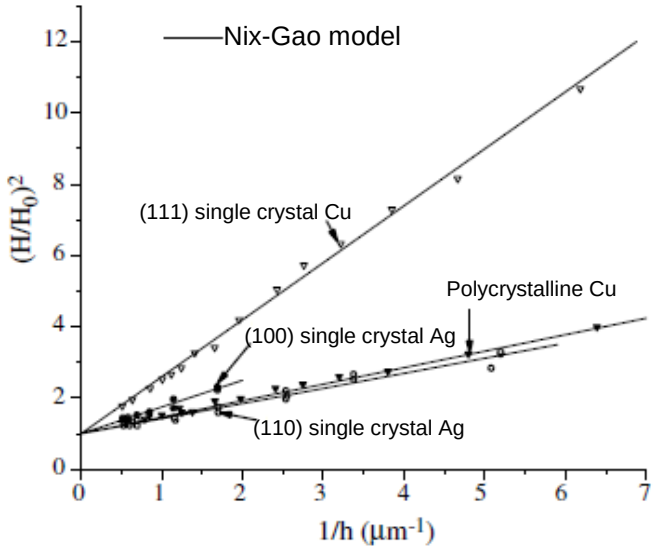

Figure 1.1: Micro-indentation hardness data for single crystal and polycrystalline copper as well as for single crystal silver. [McElhaney et al. (1998); Ma and Clarke (1995)]

The Nix-Gao model is based on the concept of geometrically necessary dislocations (GNDs), that is, dislocations that exist near the indentation to accommodate the material displaced by the indenter at the surface. Fig.1 shows that the Nix-Gao relation fits well with the indentation hardness of single crystal Cu, cold worked polycrystalline Cu, and single crystal Ag when the data for depths larger than 0.2 μm. It should note that, the geometrically necessary dislocations (GNDs), are stored for the compatible requirement deformation when the material is undergoing non-uniform deformation. The density of GNDs can be related to the strain gradient of the plastic deformation via the Burgers vector, therefore, the increase of the indentation hardness at micro/nano scale can be attributed to the strain gradient effect.

Swadener et al. (2002) extended Nix and Gao model to the case of spherical indenters. Their data show that, for a spherical indenter, the hardness is not dependent on the indentation depth, but depends on the radius of the indenter. The formula of the hardness is given by replacing h^* and h in Eq. (1) with R^* and R as $(H/H_0)^2 = 1 + R^*/R$.

However, some recent nanoindentation hardness data for a sharp, conical indenter does not obey the Nix–Gao relation Eq. (1). Lim and Chaudhri's (1999) nano-indentation hardness data for annealed copper start to deviate from Eq. (1) when the indentation depth is on the order of 100 nm. Swadener et al. (2002) also showed that the nano-indentation hardness data for annealed iridium are smaller than that predicted by Eq. (1) when the indentation depth becomes submicron.

Qu et al. (2004) studied this deviation by using a unified model of conical indenter with a spherical tip of various radii. The numerical results show that the indenter tip radius may be partially responsible for the deviation of nano-indentation hardness from the Nix–

Gao relation Eq. (1). Another reason for discrepancy between Eq. (1) and nano-indentation hardness data is probably the surface roughness. The surface topography has been a major concern for many material researches because they contribute not only to the surface mechanical properties but also to the life cycle of the active components. The measurement of topography is now possible over a wide range of length scales, down to atomic scales using atomic force microscopy (AFM). The nano-indentation could be influenced by the surface properties where the scale of indentation is comparable to that of the topography.

Bobji et al. (1998, 1999) studied the hardness of rough surface by modeling it as asperities of small radii riding on the back of asperities of larger radii. In this model, they assumed that penetration of indenter on the surface brings asperities of small radius into play first. Asperities of larger radius are encountered with increasing penetration, and then the measured hardness change with penetration. Bobji et al. (1999) conducted the nano-indentation experiments on a prepared rough surface which consists of fabricated pyramidal asperities, and found the hardness of a rough surface can be captured by introducing an error term into the indentation depth, such as

$$H = (1 - \frac{k}{h / R_{rms}})^n H_0 \qquad (2)$$

where k and n depend on indenter geometry, R_{rms} is the root mean square roughness. Eq. (2) shows that the indentation hardness becomes lower with considering the effect of surface roughness. Wei et al. (2004) studied the influence of surface roughness on hardness for single-crystal copper specimen and for surface-nanocrystallized Al-alloy specimen by using the atomic force microscopy (AFM) technique. Wei et al. (2004) revised the method

of Bobji et al. (1999) by replacing the original depth with an effective indent depth and gave the hardness for the Berkovich indenter by considering both the effect of surface roughness and the size effect as

$$H = (1 - \frac{h_e}{h})^2 \sqrt{1 + \frac{h^*}{h - h_e}} H_0 \tag{3}$$

where $h_e = kR_{rms}$, R_{rms} is the root mean square roughness shown in Eq. (2). Wang et al. (2010) simulated the nano-indentation of a nanodot-patterned surface (NDPS) covered with an ordered array of nanodots which forms the ‘‘roughness” on the NDPS (see Fig. 2). A FEM model of single-asperity contact between a nanodot and an indenter tip was developed to establish the relationship between the displacement of a single nanodot and the load applied on it. The numerical results show that the contact force between the indenter tip and the Ni NDPS is nearly 3 times larger than that between the tip and a smooth substrate for the indentation depth within 100 nm. This implies that the nano-hardness of the indented material will become lower with the nanodot on the surface.

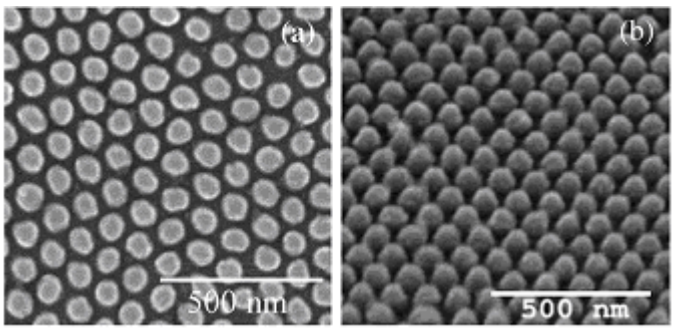

Figure 1.2: Images of a Ni NDPS showing its topography: (a) view from the top; (b) view from 45° oblique-angles. [Wang et al. (2010)]

However, some other experiments showed the opposite results for the hardness on a rough surface: higher than that of a smooth surface. Zhang et al. (2004) introduced an apparent surface stress F, which represents the energy dissipated per unit contact area, to study the surface effect and modified the Nix-Gao relation (Eq. (1)) as

$$\frac{H}{H_0} = \sqrt{1 + \frac{h^*}{h}} + \frac{gf}{h}, \quad f = 2e_c / g + f_s \tag{4}$$

where g is a numerical factor that depends on the indenter tip, e_c is the dissipation energy per contact project area, and f_s is the thermodynamic surface stress, which is related to the increase of the surface energy. Considering the e_c and f_s in Zhang's model (Eq. (4)) are difficult to be measured experimentally, Kim et al. (2007) developed a more easily applicable relation between the indentation hardness and the surface roughness

$$\frac{H}{H_0} = \sqrt{1 + \frac{h^*}{h_c - 2.46R_a}} + \frac{0.39R_a}{h_c - 2.46R_a} \tag{5}$$

where R_a is the average surface roughness. The model (Eq. (5)) is applied to nano-indentation results for Ni samples with different surface-roughness and seems be valuable in characterizing the size effect for contact depths less than a critical contact depth.

From the modified Nix-Gao model (Eq. (3)-(5)), we could see that, both the size effect (strain gradient effect) and the rough surface have significant influence on the nano-indentation hardness. For the sheet forming process: surface texturing, which is used to create new characteristic feature on the sheet surface, the plastic deformation of the sheet is confined on the surface region and is comparable to the magnitude of surface

roughness which is usually at the micro/nano scale. Therefore, the strain gradient effect should be taken into account in such a surface texturing process.

1.2 Effect of surface texturing on the formability of sheet metal

The enhancement of the formability is an important objective in sheet metal forming. In the forming process, such as uniaxial/biaxial tensile, sheet material is subjected to plastic deformations. In the beginning, the plastic deformation is homogenous but after this initial stage the deformation becomes unstable and localization of the strain occurs in a narrow region of the specimen. Such phenomenon is called necking, which will ultimately lead to the onset of fracture. The presence of necking has key influence on the forming process and therefore has attracted significant research effort over the years.

The phenomenon of necking has been studied by theoretical and numerical analysis. As a pioneer work, Needleman (1972) studied a cylindrical bar in uniaxial tension with two boundary conditions: shear-free ends and clamped ends. Based on Needleman's work, Brunig (1998) analyzed by finite element analysis the tensile test of a cylindrical bar with various initial imperfections by applying rigid displacement boundary condition by at the two ends.

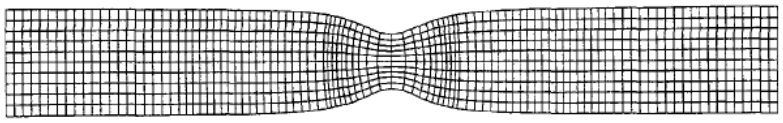

Figure 1.3: Localized necking of tensile specimen. [Brunig (1998)]

Experimental work on necking of sheet materials has mainly focused on two aspects: (1) determination of the entire true stress-strain relation as well as the material properties, such as the Young's modulus, the hardening rate and the yield stress (Zhang et al., 1999; Cabezas and Celentano, 2004), and (2) establishment of the forming limit diagrams (FLD). In sheet forming processes forming limit diagrams (FLD) are often used to predict limiting combination of major and minor principal strains in the plane of the stretched sheet, which the material can experience without failure. The establishment of such diagrams includes study of the necking under more general conditions than the uniaxial tensile test. Brunet et al. (1998) and Brunet and Morestin (2001) determined the FLD of anisotropic sheet by using experimental and analytical approaches. A necking criterion including modified Gurson-Tvergaard damage model is proposed. The theoretical FLD curves of aluminum alloy are obtained based on this necking criterion with and without damage. Their results show that the theoretical curve with damage matches better the experimental data.

The macroscopic property of the material, i.e., the work hardening rate, is a main factor for determining the occurrence of necking. According to the Considere criterion, the necking should occur when the true strain reaches the work hardening exponent. Therefore, the material with a higher work hardening exponent would have a larger necking strain (Needleman, 1972). For the sheet metal with a thin thickness equal to a few microns, the strain gradient effect should be taken into account. Niordson and Redanz (2004) studied the necking of the plane strain sheet through the strain gradient plasticity theory proposed by Fleck and Hutchinson (2001). The results predicted by the strain gradient theory have a significant delay on necking compared to those for conventional plasticity theory. Safikhani

et al. (2009) incorporated the strain gradient theory into the Marciniak and Kuczynski method to analyze the deformation localization and to predict the corresponding FLD. The results show that the predicted FLD that take into account the strain gradient effects are hardly dependent on the assumed initial imperfection factor.

Buck crystallographic texture and microstructure have been shown to affect formability of sheet materials (Wu et al., 2004; Lademo et al., 2008). Compared to changing the whole texture of the material, surface texturing could be a simpler way to improve the formability via only modifying the surface property of the sheet. The plastic deformation during surface texturing is localized in the sheet surface region which is regularly at a scale of micron. Therefore, strain gradient effect becomes significant and the stiffness of the material on the surface region could be greatly increased due to strain gradient hardening, resulting in the delay of necking for the whole sheet.

1.3 Surface texturing in sheet metal rolling

Sheet rolling is a metal forming process which is usually treated as a plane-strain stationary process. In rolling process, the surfaces of the rolled sheet are subjected to interfacial flattening and shearing under the applied force by the work rolls. This involves both the formation of new surfaces and partial disappearance of the original surfaces. The transfer of the surface feature is one of the main objectives in the production process of sheet metal. The surface feature does not only influence the mechanical behavior in further process but also the optical appearance of the finished product, and therefore it

has a decisive influence on the quality of the product. Therefore, Surface texturing has gained more and more importance in the production process of sheet metal.

Ma et al. (2002) studied surface transfer in cold rolling of carbon steel strip with different rolling condition. The experiments show that smooth surface was obtained for small reduction and lubrication contributes to a decrease in the sharpness of surface. Ike et al. (2002) studied the rolling of aluminum sheet at a thickness reduction of 5–13% and observed the tool–specimen interface by using a "visual rolling system" which is composed of a small CCD camera with a macro-lens into the upper roll. From observation of the rolling interface with image processing, Ike et al. (2002) proposed a model of surface texture which shows that the reduction of thickness determines the formation of ridges and valleys on the surface, and therefore influences emission of lubricant at the outlet of the roll. Andersson et al. (2006) studied the surface transfer from silicon nitride rolls to stainless steel wire in cold rolling. The experiments were carried out using a cold-rolling mill with four consecutive work rolls which has higher surface quality, while the steel wire has relatively rough surfaces (the average roughness R_a of wire sample is in the range of 50-90 nm). The experiments show that, the peak value of the roll surface, R_{p}, shows good correlation with the valley depth of the wire surface, R_{v}, at the end of the main tests. The transfer of the R_a value from the ceramic roll onto the rolled steel wire took place with an accuracy of approximately 60 nm or better for all the wire samples. Kang et al. (2008) analyzed the change of the sheet surface topography by using 'surface texture anisotropy ratio' (STAR), which is defined

as the ratio of the square of the longitudinal roughness to transverse roughness. The STAR parameter can account for frictional changes observed in cold rolling of aluminum.

The above experiments are performed by using the conventional rolling mill with relatively smooth roller. However, in order to obtain desired surface feature, textured rollers with specially designed pattern is required in the rolling process. Currently, the common methods used to texture work rolls are Shot Blasting Texturing (SBT), Laser Texturing (LT), Electron Beam Texturing (EBT) and Electrical Discharge Texturing (EDT). In conventional SBT operations, the texture on the roll surface is produced by the impact of hard shot (e.g. chilled cast iron). The problem of SBT is that there is little control over the created surface texture due to the large and diverse number of variables involved in the process. LT, EDT and EBT have significant advantages over SBT in that roll surface texture can be accurately specified in advance and consistent features are obtained between rolls which are working in pairs in the mill.

Electrical discharge texturing (EDT) is an eroding and removing process of the material from the surface by transient action of electric sparks which are used to produce die cavities. In EDT, this process is achieved by applying consecutive spark discharges between a rotating roll and electrodes moving in radial direction. Simão et al. (1994, 1996) studied the surface texture transfer of cold reduced steel sheet by using the electrical discharge textured (EDT) rolls. The experiments show that the degree of topography transfer is a function of reduction rate: higher reduction rates produce a more efficient transfer of the original roll texture on the steel sheet. Miller et al. (2000) found out that stochastic EDT surface textures improve the paint appearance by reducing orange

peel defects**.** Tobiyama and Abotani (2004) found out that EDT is beneficial for producing steel sheets with excellent press formability by changing the roughness profile of the rolls. Fig. 1.4 shows the surface of an EDT sheet. It is seen that, the EDT textured sheet has a stochastic pattern of isolated pocket structure.

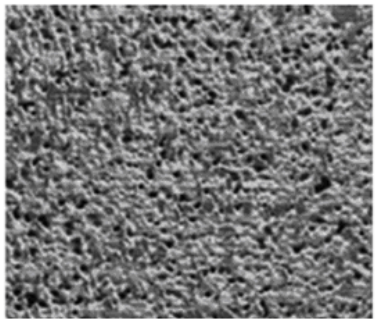

Figure 1.4: Surface of an EDT sheet. [Zhou et al. (2011)]

In laser texturing (LT) process, a beam from a high energy gas laser is focused on to the roll surface. The high energy density causes local melting of the roll, resulting in the formation of a discrete crater. The depth and size of the crater can be controlled by the energy and dwell time of the beam. The electron beam texturing (EBT) technology is a similar process which uses an electron beam instead of a laser. Vermeulen et al. (1995) studied the 3D feature of EBT sheet surface which is characterized by some geometrical parameters, e.g., the surface roughness R_a and peak count P_c. The measured textures show that the EBT is able to produce a much larger range of R_a and P_c combinations because the intensity and the density of the electron beams can be varied independently over a large range. Xie et al. (1999) studied the three-dimensional surface topography of several steel sheets processed by different technologies, such as SBT, EBT and EDT. The characterizing parameters and functions of the surface topography (e.g. areal power

spectrum density function) are calculated by using statistical and signal processing techniques. The measured data show that the surfaces of EDT have relatively small roughness compared to the surfaces of SBT steel sheets.

Recently, deterministic surface textures on the micro-scale level have been studied experimentally. Geiger et al. (2002) investigated the effect of laser surface texturing based on asymmetrical upsetting tests and demonstrated that surface texturing can increase the tool life in cold forging. Etsion et al. (2004) investigated the performance of parallel-thrust bearings with surface textures and clear performance enhancements in terms of increased clearance and reduced friction were found. Kovalchenko et al. (2005) examined friction between a flattened steel ball and laser textured steel disk, through which the friction reduction effect of dimples on the disk were found to be more apparent in situations with higher sliding speeds. Fig. 1.5 shows the optical micrographs of disc surfaces after various treatments. Fig. 1.5a shows the surface polished smooth; Fig. 1.5b shows the ground surface; Fig. 1.5c shows the surface produced by laser surface texturing (LST), and Fig. 1.5d shows the textured surface with higher dimple density. Wan and Kumar et al. (2008) investigated the effect of roughness of various kinds of dimpled surfaces on friction, and found that the friction coefficient varied considerably with surface textures. Liewald et al. (2010) investigated the friction behaviors of EDT sheets under relatively low contact pressures using a rotating friction tester. The results show that the friction behavior is influenced by angles between sheet rolling direction and sliding direction.

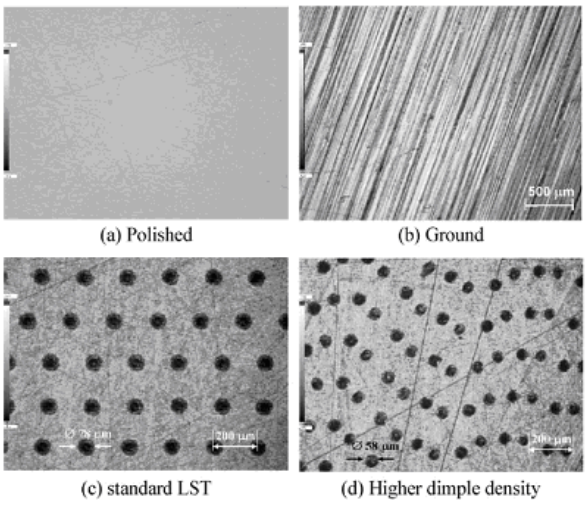

Figure 1.5: Optical micrographs of disc surfaces after various treatments.
[Kovalchenko et al. (2005)]

As the surface texturing includes an immense variety of materials, dimensions, textured rollers with complex surface features, it is practically impossible to make a prediction by experimental rolling tests for each variant. Therefore, it is necessary to develop a simulation model which allows a precise prediction of the transfer behaviour.

Finite element method (FEM) has been widely used to simulate many kinds of rolling processes, such as slab rolling and strip rolling. Bunten et al. (1996) developed a FEM model to analyze the transfer behaviour of sheet surface by using the electron-beam texturing technique (EBT). The FEM model is able to describe the change of microscopic geometry on the surface, which shows a good agreement with the experimental result. The numerical results also reveal some basic transfer mechanism (e.g. penetration processes and reverse extrusion phenomena). Bunten et al. also applied a substitute profile model to explain the transfer behaviour. Huart et al. (2004) developed a model to predict the local behaviour of surface asperities during cold rolling and found that the forward slip and

reduction ratio has important influence on the plastic deformation of the asperity through pressure and shear force. Their simulation also includes the trapping of lubricant which fills the cavity on the surface and avoids a total flattening of the asperities. Kijima et al. (2008a, b) studied the influence of tool roughness in skin-pass rolling of steel strip by using elasto-plastic FE analysis, and the results show that smaller tool roughness and larger pitch lead to larger transfer of tool roughness to workpiece surface.

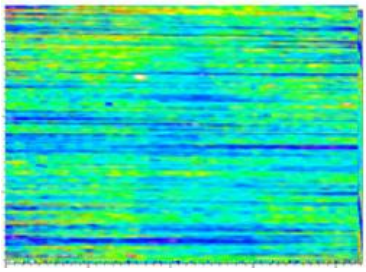

Figure 1.6: Mill-Finish (MF) surface. [Liewald et al. (2010)]

Normally, the surface of aluminum sheet is not textured but has a mill finish. Fig. 1.6 shows the Mill-Finish (MF) surface which exhibits strong linear structure (or band-type feature), caused by the rolls dressed in circumferential direction. In order to achieve a better surface appearance for the sheet, a further processing with textured roller is necessary so as to modify such a band-type feature. In the following, we will simulate this surface texturing by using textured rolls with plateaus on the roll surfaces. A quantitative analysis of the deformed sheet surface will reveal that the textured rolls could effectively change the sheet surface and produce a relatively random feature. Textured rolls with different shapes of plateaus are considered in our numerical model. The numerical results show that the shapes of plateaus and the number of the plateaus have significant influence on the deformed sheet surface. The size of the plateaus is taken on the order of micron, which is comparable to the

magnitude of the surface roughness, so that surface texturing occurs only in the surface region. In other words, the total mechanical properties of the sheet are not changed in surface texturing.

It should point out that, the plastic deformation during surface texturing is confined in the surface region, which is usually on the order of micron or submicron. Therefore, the strain gradient effect maybe plays an important role in the formation of the surface texture.

As a summary, the surface texturing is mainly used to improve the optical appearance of the sheet surface or to enhance the formability. In chapter 2, a brief review of the development of the strain gradient plasticity theory is presented. A selected theory of strain gradient plasticity will be employed to the numerical simulation of the surface texturing process. In chapter 3, the nano-indentation on a rough surface is studied by using a FEM model based on implemented strain gradient theory. The numerical results show that the both the surface roughness and the strain gradient effect has significant influence on the nano-indentation hardness. In chapter 4, a FE model is developed to simulate the tensile test of the sheet with textured surface. A textured surface of the sheet is prepared through the indention on the sheet surface. The results show that the textured surface becomes harder due to the strain gradient effect, and delays the onset of localized necking. In chapter 5, 3D FE model is developed to simulate the surface texturing of sheet metal by rolling process. The results show that textured rollers could effectively modify the original sheet surface which have typical band-type feature along the rolling direction. Strain gradient effect has been taken into account in the rolling process to predict the deformed surface.

Chapter 2: A review of strain gradient plasticity theory

Many experiments have shown that, metals exhibit strongly size dependent mechanical behavior at the micron and submicron scales. For example, the micro-indentation hardness of metallic materials increases by a factor of 2–3 as the indentation depth decreases to microns and sub-microns (e.g., Nix, 1989, 1997; Stelmashenko et al., 1993; Ma and Clarke, 1995; Poole et al., 1996; McElhaney et al., 1998; Suresh et al., 1999; Swadener et al., 2002); the plastic hardening rate increases in the torsion of thin copper wires as the wire diameter decreases from 170 to 12 μm (Fleck et al., 1994); the strength of aluminum matrix (reinforced by micron-size silicon carbide particles) increases with the reduction of the reinforcing particle size when the particle volume fraction is constant (Lloyd, 1994). More evidence of the strength increase has been observed in the micro-bend tests of nickel foils (Stolken and Evans, 1998) and sub-micron thick aluminum beams (Haque and Saif, 2003), and in a micro-electro-mechanical system (MEMS) which is used for the design of micromechanical parts contained in tiny machine (Douglass, 1998).

The aforementioned size effect can be explained by the dislocations from the microscopic viewpoint of the plasticity. There are two types of dislocations generated and stored when the material is deformed. One is called statistically stored dislocations, which accumulate randomly during a general plastic deformation; the other one is called geometrically necessary dislocations, which is stored for the compatible requirement deformation when the material is undergoing inhomogeneous deformation. The size effects have been attributed to geometrically necessary dislocations which is associated

with plastic strain gradient. Discrete dislocation simulations have been used to model and confirm the size effect in micro-scale deformation (e.g., Cleveringa et al., 1997, 1998, 1999a, b).

The conventional plasticity theory can not predict the size effect of material behavior at micron scale. Therefore, the continuum theory for the size effect is necessary for the applications to materials and structures with micron-scale plastic deformation, such as in micro-components and MEMS, micro-electronic packages, micro-machining, and composite materials. Based on the notion of geometrically necessary dislocations in the dislocation theory (Nye, 1953; Cottrell, 1964; Ashby, 1970; Arsenlis and Parks, 1999; Gurtin, 2000), the continuum approach to model the size effect has been developed via the strain gradient plasticity theory.

The existing strain gradient plasticity theories can be divided into two classes. The first method of modeling size effects is to formulate a plastic strain-gradient-dependent work-hardening law (Acharya and Bassani, 2000; Bassani, 2001; Huang et al., 2004; Brinckmann et al., 2006). In this class of theories, only the plastic modulus is modified by incorporating the plastic strain-gradients. Thus, the formulation of the boundary condition remains the same as the conventional model, i.e., it is sufficient to consider the conventional surface traction and prescribed displacement conditions at the boundaries. This class is called ‘‘lower-order” theories.

The second class is ‘‘higher-order” extension of the conventional plasticity theory (Mindlin, 1964, 1965). Most of higher-order strain-gradient plasticity theories have introduced an extended virtual work, which postulates existence of higher-order stress

work-conjugate to the plastic strain gradient (Fleck and Hutchinson, 1993, 1997, 2001; Fleck et al., 1994, Gao et al., 1999; Chen and Wang, 2000, 2002; Huang et al., 2000a, b; Gurtin, 2000, 2002; Hwang et al., 2002, 2003a). The order of equilibrium equations are higher than that in the conventional continuum theories, therefore, additional boundary conditions are required, i.e., additional force balance law and a corresponding extra traction condition are imposed on the boundaries.

2.1 Mindlin (1964, 1965)

Mindlin (1964, 1965) proposed the couple stress theory which is a more general isotropic –hardening theory based on all the quadratic invariants of the strain gradients.

The generalized strain variables are the symmetric strain tensor $\varepsilon_{ij} = \frac{1}{2}(u_{i,j} + u_{j,i})$ and the second gradient of displacement $\eta_{ijk} \equiv u_{k,ij}$. The increment of strain energy density of material due to an arbitrary variation of displacement u is

$$\delta w = \sigma_{ij}\delta\varepsilon_{ij} + \tau_{ijk}\delta\eta_{ijk} \tag{6}$$

where the symmetric Cauchy stress σ_{ij} is the work conjugate of the strain variation $\delta\varepsilon_{ij}$ and the higher-order stress τ_{ijk} is the work conjugate of the strain gradient variation $\delta\eta_{ijk}$. The higher-order stress tensor is composed of components of both couple stresses and double stresses.

An isotropic deformation theory of plasticity is then developed for the case that the strain energy density w depends on both the second-order symmetric strain tensor ε

and the third-order strain gradient tensor η. Eq. (6) implies that the second-order stress σ is given by $\sigma_{ij} = \partial w / \partial \varepsilon_{ij}$ and the third-order stress τ is given by $\tau_{ijk} = \partial w / \partial \eta_{ijk}$.

Following the strategy of Mindlin, the work increment for a volume V is given as

$$\begin{aligned}\int_V [\delta\, w] dV &= \int_V [\sigma_{ij}\delta\varepsilon_{ij} + \tau_{ijk}\delta\eta_{ijk}]dV \\ &= -\int_V [\partial_i(\sigma_{ik} - \partial_j \tau_{ijk})]\delta u_k dV + \int_S [n_i(\sigma_{ik} - \partial_j \tau_{ijk})]\delta u_k dS + \int_S [n_i \tau_{ijk}(\partial_j \delta u_k)]dS\end{aligned} \tag{7}$$

where n_i is the unit normal to the surface S of the body. The term $\partial_j \delta u_k$ in Eq. (7) can be resolved into a surface-gradient, $D_j \delta u_k$, and a normal gradient, $n_j D\delta u_k$, such as

$$\partial_j \delta u_k = D_j \delta u_k + n_j D\delta u_k \tag{8}$$

where the surface gradient operator D_j, and the normal gradient operator D are given as

$$D_j \equiv (\delta_{jk} - n_j n_k)\partial_k, \quad D \equiv n_k \partial_k \tag{9}$$

We substitute Eq. (8) and Eq. (9) into Eq. (7) and use the Stokes's surface divergence theory to obtain the final form of the principle of virtual work

$$\begin{aligned}&\int_V [\sigma_{ij}\delta\varepsilon_{ij} + \tau_{ijk}\delta\eta_{ijk}]dV \\ &\qquad = \int_V [f_k \delta u_k]dV + \int_S [t_k \delta u_k]dS + \int_S [r_k (D\delta u_k)]dS\end{aligned} \tag{10}$$

Where the body force per unit volume is f_k. The equilibrium relation in V is

$$f_k + \partial_i\left(\sigma_{ik} - \left(\partial_j \tau_{ijk}\right)\right) = 0 \tag{11}$$

The surface traction t_k on the surface S is

$$t_k = n_i\left(\sigma_{ik} - \left(\partial_j \tau_{ijk}\right)\right) + n_i n_j \tau_{ijk}(D_p n_p) - D_j(n_i \tau_{ijk}) \tag{12}$$

and the double stress traction r_k on S is

$$r_k = n_i n_j \tau_{ijk} \tag{13}$$

We conclude from Eq. (10) that the displacement u must satisfy three equilibrium equations given by Eq. (11) and six boundary conditions given by Eq. (12) and Eq. (13).

2.2 Fleck and Hutchinson (1993, 1997)

Fleck and Hutchinson (1993) developed a phenomenological theory of strain gradient plasticity based on rotation gradients which fits with the couple stress theory.

The strain tensor ε is related to the material displacement u via $\varepsilon_{ij} = (u_{i,j} + u_{j,i})/2$, and the curvature χ is spatial gradient of the material rotation θ:

$$\chi_{ip} = \theta_{i,p} = \frac{1}{2} e_{ijk} u_{k,jp} = e_{ijk} \varepsilon_{kp,j} \tag{14}$$

where e_{ijk} is the permutation tensor. The yield strength is assumed to depend on the 'overall effective strain' quantity ξ which is defined as

$$\xi = \sqrt{\varepsilon_e^2 + l^2 \chi_e^2} \tag{15}$$

where ε_e is the second invariant of strain, $\varepsilon_e = \sqrt{2\varepsilon_{ij}\varepsilon_{ij}/3}$; and χ_e is the second invariant of the curvature, $\chi_e = \sqrt{2\chi_{ij}\chi_{ij}/3}$. The material length scale l is introduced as required for dimensional consistency.

Fleck and Hutchinson (1997) defined the effective strain gradient as

$$\eta = \sqrt{c_1 \eta_{iik}\eta_{jjk} + c_2 \eta_{ijk}\eta_{ijk} + c_3 \eta_{ijk}\eta_{kji}} \tag{16}$$

where the three constants c_1, c_2, c_3 scale the three quadratic invariants for the third order tensor η_{ijk}. They also showed that the strain gradient tensor η_{ijk} can be decomposed as

$$\eta = \eta^{(1)} + \eta^{(2)} + \eta^{(3)} \tag{17}$$

Where

$$\eta^{(1)}_{ijk} = \eta^{S}_{ijk} - \tfrac{1}{5}[\delta_{ij}\eta^{S}_{kpp} + \delta_{jk}\eta^{S}_{ipp} + \delta_{ki}\eta^{S}_{jpp}]$$

$$\eta^{(2)}_{ijk} = \tfrac{1}{6}[e_{ikp}e_{jlm}\eta_{lpm} + e_{jkp}e_{ilm}\eta_{lpm} + 2\eta_{ijk} - \eta_{jki} - \eta_{kij}]$$

$$\eta^{(3)}_{ijk} = \tfrac{1}{6}[-e_{ikp}e_{jlm}\eta_{lpm} - e_{jkp}e_{ilm}\eta_{lpm} + 2\eta_{ijk} - \eta_{jki} - \eta_{kij}] + \tfrac{1}{5}[\delta_{ij}\eta^{S}_{kpp} + \delta_{jk}\eta^{S}_{ipp} + \delta_{ki}\eta^{S}_{jpp}]$$

In the above equations, δ_{ij} is the permutation tensor and η^S represents the symmetric part of η,

$$\eta^{S}_{ijk} = \tfrac{1}{3}[\eta_{ijk} + \eta_{jki} + \eta_{kij}] \tag{18}$$

The effective strain gradient is then defined as

$$l\eta = \sqrt{l_1^2\eta^{(1)}_{ijk}\eta^{(1)}_{ijk} + l_2^2\eta^{(2)}_{ijk}\eta^{(2)}_{ijk} + l_3^2\eta^{(3)}_{ijk}\eta^{(3)}_{ijk}} \tag{19}$$

Where l_1, l_2, l_3 are three constitutive lengths, and can be determined by fitting the experimental data. The couple stress theory of strain gradient plasticity by Fleck and Hutchinson (1993) corresponds to the following choice

$$l_1 = 0, \quad l_2 = \tfrac{1}{2}l, \quad l_3 = \sqrt{\tfrac{5}{24}}l \tag{20}$$

where the effective strain gradient can be related to the curvature tensor χ_{ij} as

$$\eta = \sqrt{\tfrac{2}{3}\chi_{ij}\chi_{ij}} \tag{21}$$

The relationship between χ_{ij} and η_{ijk} is given as

$$\chi_{ij}\chi_{ij} = \frac{3}{8}\eta_{ijk}^{(2)}\eta_{ijk}^{(2)} + \frac{5}{16}\eta_{ijk}^{(3)}\eta_{ijk}^{(3)} \tag{22}$$

$$\chi_{ij}\chi_{ji} = \frac{3}{8}\eta_{ijk}^{(2)}\eta_{ijk}^{(2)} - \frac{5}{16}\eta_{ijk}^{(3)}\eta_{ijk}^{(3)} \tag{23}$$

where $\eta_{ijk}^{(2)}$ and $\eta_{ijk}^{(3)}$ are associated with the rotational gradients, while $\eta_{ijk}^{(1)}$ is associated with the stretch gradients.

2.3 Gao et al. (1999)

Gao et al. (1999) proposed a mechanism-based strain gradient (MSG) theory of plasticity within a multiscale framework, namely:

(a) At the microscale, the Taylor formula of the flow strength, suitably modified to account for both SSD (statistically stored dislocation) and GND (geometrically necessary dislocation) , is written as

$$\sigma_{\text{flow}} = \sigma_Y \sqrt{f^2(\varepsilon) + l\eta} \tag{24}$$

where $l = 3\alpha^2(\frac{\mu}{\sigma_Y})^2 b$ is identified as the material length introduced by Fleck and Hutchinson (1993, 1997). For a typical metallic material which has the ratio of $\mu/\sigma_Y = 100$, the material length l is on the order of $10^4 b$ which is in the order of microns, in agreement with the experimental estimation.

(b) At the mesoscale, it is sufficiently large to connect the notion of geometrically necessary dislocation to the gradient of strain field and to institute the constitutive framework based on the Taylor dislocation model. The microscale and mesoscale are linked by the plastic work equality within a mesoscale cell,

$$\int_{V_{\text{cell}}} \bar{\sigma}'_{ij}\delta\bar{\varepsilon}_{ij}\,\mathrm{d}V = (\sigma'_{ij}\delta\varepsilon_{ij} + \tau'_{ijk}\delta\eta_{ijk})V_{\text{cell}} \tag{25}$$

where $\bar{\sigma}$, $\bar{\varepsilon}$ represent the stress and strain tensor at micro level, while the stress σ, strain ε, the higher order stress τ and strain gradient η are the mesoscale variables. The deviatoric part of microscale stress $\bar{\sigma}_{ij}$ is given as:

$$\bar{\sigma}'_{ij} = \frac{2\bar{\varepsilon}_{ij}}{3\bar{\varepsilon}}\,\bar{\sigma}_e \tag{26}$$

where $\bar{\sigma}_{\text{e}} = \sigma_{\text{flow}}$ which is given by Eq. (24). Consider a unit cell on the mesoscale with the length of all edges equal to l_ε. Gao et al. (1999) showed that, when the cell size l_ε is sufficiently small, the microscale strain tensor $\bar{\varepsilon}_{ij}$ can be related to the mesoscale strain ε_{ij} and the strain gradient tensor η_{ijk} as

$$\bar{\varepsilon}_{ij} = \varepsilon_{ij} + \tfrac{1}{2}(\eta_{kij} + \eta_{kji})x_k \tag{27}$$

Where the x_k represents the local coordinates. The substitution of Eq. (26) and Eq. (27) into Eq. (25) will finally yield the constitutive equations for the MSG theory.

There is requirement of the cell size which should be sufficiently small to ensure the strain gradient calculated in the cell is accurate. On the other hand, the cell also needs to be large enough to contain a sufficient number of dislocations to ensure the accuracy of the flow stress. Gao et al. (1999) defined the cell size as

$$l_\varepsilon = \beta L_{\text{yield}} = \beta\frac{\mu\, b}{\sigma_Y} \tag{28}$$

where L_{yield} is the mean spacing between statistically stored dislocations at yielding and β is a constants which is larger than 1. For a typical structural material which has the material properties: $\mu/\sigma_Y = 100$, $b = 0.1nm$, the mean spacing L_{yield} is around 10 nm, while the cell size is in the range 10-100 nm for the coefficient β taken to be 1-10.

Gao et al. (1999) also determined the constants in Eq. (16) from three dislocation models: plane strain bending, pure torsion and 2-D axisymmetric void growth, such as

$$c_1 = 0,\ c_2 = \frac{1}{4}, c_3 = 0 \tag{29}$$

The substitution of Eq. (26) into Eq. (16) gives the effective strain gradient as

$$\eta = \sqrt{\frac{1}{4}\eta_{ijk}\eta_{ijk}} \tag{30}$$

2.4 Acharya and Bassani (2000)

Acharya and Bassani (2000) and Bassani (2001) proposed a gradient theory which does not involve higher-order stresses.

In the continuum theory, the crystal lattice is assumed to distort only elastically during plastic flow, while the elastic deformation is not compatible with a regular displacement field. The incompatible lattice distortion is attributed to the presence of geometrically necessary dislocations. The incompatibility can be measured in terms of the gradient of plastic strain as

$$\alpha_{ij} = e_{jkl}\varepsilon^{\mathrm{P}}_{il,k} \tag{31}$$

For the isotropic material, the hardening-rate is assumed to depend on both the von Mises effective plastic strain and the second invariant of the incompatibility parameter, i.e.

$$\alpha^2 = 2\alpha_{ij}\alpha_{ji} \tag{32}$$

The constitutive relation is

$$\dot{\sigma}_{ij} = C_{ijkj}(\dot{\varepsilon}_{ij} - \dot{\varepsilon}^P_{ij}) \tag{33}$$

$$\dot{\varepsilon}^P_{ij} = (\frac{\dot{\gamma}^P}{2\tau})\sigma'_{ij} \tag{34}$$

where τ is the von Mises effective shear stress, $\tau = \sqrt{\sigma'_{ij}\sigma'_{ij}/2}$; γ^P is the effective plastic strain that is work conjugate to τ. The relation of τ and γ^P is given by hardening law as

$$\dot{\tau} = h(\gamma^P, \alpha)\dot{\gamma}^P \tag{35}$$

where h is the hardening modulus that is taken to depend both on the effective plastic strain and the incompatibility parameter (or strain gradient). A simple hardening function that incorporates an increase in hardening rate due to strain gradient is

$$h(\gamma^P, \alpha) = h_0(\frac{\gamma^P}{\gamma_0} + 1)^{N-1}\left[1 + \frac{l^2(\alpha/\gamma_0)^2}{1 + c(\gamma^P/\gamma_0)^2}\right]^{1/2} \tag{36}$$

where l is the material length scale. The term in the numerator of the square bracket represents the increase of hardening due to GND. The term in the denominator is introduced to account for a significant gradient effect at the initial stage of deformation.

It is clear that the gradient effect is introduced into the constitutive relation via the hardening modulus. Only the ordinary Cauchy stress presented in the formulation, the higher-order stresses are not required.

2.5 Huang et al. (2004)

Huang et al. (2004) proposed a conventional theory of mechanism-based strain gradient plasticity based on the Taylor dislocation model.

The dislocation model of Taylor (1934, 1938) and Bailey and Hirsch (1960) gives the shear flows tress τ in terms of the dislocation density ρ as

$$\tau = \alpha\mu b\sqrt{\rho_{\mathrm{T}}} = \alpha\mu b\sqrt{\rho_{\mathrm{S}} + \rho_{\mathrm{G}}} \tag{37}$$

where μ is the shear modulus, b is the magnitude of the Burgers vector, α is an empirical coefficient around 0.3, ρ_{T} is the total dislocation density, ρ_{S} is the density of statistically stored dislocations, ρ_{G} is the density of geometrically necessary dislocations, and ρ_{G} can be related to the effective plastic strain gradient η^{p}, by

$$\rho_{\mathrm{G}} = \bar{r}\frac{\eta^{\mathrm{p}}}{b} \tag{38}$$

where $\bar{r}$ is the Nye-factor and is around 1.90 for face-centered-cubic (fcc) polycrystals.

The tensile flow stress σ_{flow} is related to the shear flow stress τ by

$$\sigma_{\mathrm{flow}} = M\tau = M\alpha\mu b\sqrt{\rho_{\mathrm{S}} + \bar{r}\frac{\eta^{\mathrm{p}}}{b}} \tag{39}$$

where M is Taylor factor and $M = 3.06$ for fcc metals.

In the absence of the strain gradient term, (39) degenerates to the classical plasticity law

$$\sigma_{\mathrm{flow}} = M\alpha\mu b\sqrt{\rho_{\mathrm{S}}} = \sigma_{\mathrm{Y}} f(\varepsilon^{\mathrm{p}}) \tag{40}$$

where σ_{Y} is the initial yield stress, f is a non-dimensional function of plastic strain ε^{p}, and $\sigma_{\mathrm{Y}} f(\varepsilon^{\mathrm{p}})$ represents the stress – plastic strain curve in uniaxial tension.

The combination of (39) and (40) gives the flow stress accounting for the nonuniform plastic deformation associated with geometrically necessary dislocations as

$$\sigma_{\text{flow}} = \sqrt{[\sigma_{\text{Y}} f(\varepsilon^{\text{p}})]^2 + M^2 \bar{r} \alpha^2 \mu^2 b \eta^{\text{p}}} = \sigma_{\text{Y}} \sqrt{f^2(\varepsilon^{\text{p}}) + l \eta^{\text{p}}} \tag{41}$$

where

$$l = M^2 \bar{r} \alpha^2 \left(\frac{\mu}{\sigma_{\text{Y}}} \right)^2 b = 18 \alpha^2 \left(\frac{\mu}{\sigma_{\text{Y}}} \right)^2 b \tag{42}$$

is the intrinsic material length in strain gradient plasticity. For typical metallic materials the Burgers vector b is on the order of one tenth of a nanometer, μ/σ_{Y} is on the order of 10^2, and α is around 0.3. These give l on the order of microns, which is indeed the length scale at which the size effects are observed in micro-indentation experiments.

The constitutive law for the conventional plasticity theory gives the elastic strain rate $\dot{\varepsilon}_{ij}^{e}$ and plastic strain rate $\dot{\varepsilon}_{ij}^{p}$ as

$$\dot{\varepsilon}_{ij}^{e} = \frac{1}{2\mu} \dot{\sigma}'_{ij} + \frac{\dot{\sigma}_{kk}}{9K} \delta_{ij} \tag{43}$$

$$\dot{\varepsilon}_{ij}^{p} = \frac{3 \dot{\varepsilon}^{p}}{2 \sigma_e} \sigma'_{ij} \tag{44}$$

where μ and K are shear and bulk moduli, respectively, and $\dot{\sigma}'_{ij}$ is the deviatoric stress rate. $\sigma_{\text{e}} = \sqrt{\frac{3}{2} \sigma'_{ij} \sigma'_{ij}}$ is the von Mises effective stress, and $\dot{\varepsilon}^{p} = \sqrt{\frac{2}{3} \dot{\varepsilon}_{ij}^{p} \dot{\varepsilon}_{ij}^{p}}$ is the equivalent plastic strain rate.

One way to determine the plastic strain rate, $\dot{\varepsilon}^p$, is to use a power-law viscoplastic model developed by Kok et al. (2002a, b, c)

$$\dot{\varepsilon}^p = \dot{\varepsilon}\left[\frac{\sigma_{\mathrm{e}}}{\sigma_{\mathrm{Y}} f(\varepsilon^{\mathrm{p}})}\right]^m \tag{45}$$

where $\dot{\varepsilon} = \sqrt{\frac{2}{3}\dot{\varepsilon}'_{ij}\,\dot{\varepsilon}'_{ij}}$, $\dot{\varepsilon}'_{ij}$ is the deviatoric strain rate, and m is the rate-sensitivity exponent which usually takes a large value (≥ 20). In the limit $m=\infty$, (45) is equivalent to $\sigma = \sigma_{\mathrm{Y}} f(\varepsilon^{\mathrm{p}})$ in uniaxial tension.

The effective plastic strain rate $\dot{\varepsilon}^p$ in (45), which involves the flow stress $\sigma_{\mathrm{Y}} f(\varepsilon^{\mathrm{p}})$ in uniaxial tension, has not been accounted for the strain gradient effect. In order to introduce the strain gradient effect, Huang et al. (2004) replaced the uniaxial flow stress $\sigma_{\mathrm{Y}} f(\varepsilon^{\mathrm{p}})$ in (45) by the flow stress σ_{flow} based on the Taylor dislocation model, eqn. (24), to yield

$$\dot{\varepsilon}^p = \dot{\varepsilon}\left(\frac{\sigma_e}{\sigma_{flow}}\right) = \dot{\varepsilon}\left(\frac{\sigma_e}{\sigma_Y\sqrt{f^2\left(\varepsilon^p\right)+l\eta^p}}\right)^m \tag{46}$$

The substitution of (46) into (43) and (44) gives the strain rate

$$\dot{\varepsilon}_{ij} = \frac{1}{2\mu}\dot{\sigma}'_{ij} + \frac{\dot{\sigma}_{kk}}{9K}\delta_{ij} + \frac{3\dot{\varepsilon}}{2\sigma_e}\left(\frac{\sigma_e}{\sigma_Y\sqrt{f^2\left(\varepsilon^p\right)+l\eta^p}}\right)^m \sigma'_{ij} \tag{47}$$

The effective plastic strain gradient η^{p} in (47) is defined as

$$\eta^p = \int \dot{\eta}^p dt, \quad \dot{\eta}^p = \sqrt{\frac{1}{4}\dot{\eta}^p_{ijk}\,\dot{\eta}^p_{ijk}}, \quad \dot{\eta}^p_{ijk} = \dot{\varepsilon}^p_{ik,j} + \dot{\varepsilon}^p_{jk,i} - \dot{\varepsilon}^p_{ij,k} \tag{48}$$

This constitutive relation (48) accounts for the strain gradient effect but does not involve the higher-order stress or additional boundary conditions.

Huang et al. (2004) showed that the conventional theory of mechanism-based strain gradient plasticity (CMSG) gives the same results with the higher-order MSG plasticity theory (Gao et al., 1999; Huang et al., 2000a,b) except within a thin boundary layer of the solid.

Recently, a critical issue in the strain gradient plasticity has been the ongoing discussion of the energetic and dissipative nature of the dislocation network that accounts for many plasticity phenomena (Cermelli and Gurtin, 2002; Fleck and Willis, 2009a, b; Gurtin, 2003; Gurtin et al., 2007; Voyiadjis and Deliktas, 2009). The plastic deformation has been treated as a dissipative thermodynamic process in the literature by a number of authors (e.g. Hansen and Schreyer, 1994; Lemaitre, 1985; Naderi et al., 2010) while different invariances are feasible regarding the stored energy and the rate of entropy production, leading to different symmetry with respect to the non-dissipative and dissipative response (Rajagopal and Srinivasa, 2004a, b). In other words, when the material deforms plastically it exhibits two types of thermodynamic processes such as the energetic and dissipative processes based on the dislocation mechanisms that is affected by the plastic deformation. The source of dissipation process can be attributed to the

movement of the mobile dislocations. For example, newly formed dislocation pileups near the obstacles give rise to the size dependent material strengthening. Dislocations that appear in the crystal lattice reduce its energy. Motion of dislocations yields the dissipation of the energy which, in turn, results in resistance to the dislocation motion and increases in the yield strength due to size effects.

From the standpoint of in the phenomenological formulation of the strain gradient plasticity by Mroz and Oliferuk (2002), the energetic process attributed to the dislocation network can be characterized by plastic strain gradients that are introduced as state variable in the free energy; while the dissipative process attributed to dislocation movement can be described by the plastic strain rate gradient that is introduced as a kinematic variable into the flow rule in order to provide more resistance to flow.

Some recent research has been focused to incorporate the effects of these two processes into modeling in order to have a better understanding of the hardening and strengthening mechanisms for micro/nano structured materials.

2.6 Gurtin (2004)

Gurtin (2004) proposed a generalized theory with gradient dissipation based on a free energy potential of the form,

$$\psi = \psi(\mathrm{E}^{\mathrm{e}}, \mathrm{G}) \tag{49}$$

where E^{e} is the elastic strain, and $(\mathrm{G})_{\mathrm{ij}} = (\mathrm{curl}\,\mathrm{H}^{\mathrm{p}})_{ij} = e_{ipq} H^{\mathrm{p}}_{jq,p}$, where H^{p} represents the plastic strain, and can be decomposed into plastic stretching E^{P} and plastic rotation Ω^{P},

$$\mathrm{H}^{\mathrm{p}} = \mathrm{E}^{\mathrm{p}} + \Omega^{\mathrm{p}} \tag{50}$$

Then, the internal work within a solid body has the form of

$$W = \int (\mathrm{T} : \dot{\mathrm{E}}^{\mathrm{e}} + \mathrm{T}^{\mathrm{p}} : \dot{\mathrm{H}}^{\mathrm{p}} + S : \mathrm{curl}\dot{\mathrm{H}}^{\mathrm{p}})\, dV \tag{51}$$

where S is a microscopic stress introduced to work in conjunction with the rate of Burgers vector as characterized by $\dot{\mathrm{G}} = \mathrm{curl}\dot{\mathrm{H}}^{\mathrm{p}}$.

The second law that the free energy of a body increases at a rate not greater than the external work gives the free-energy inequality as

$$\dot{\psi} - \mathrm{T} : \dot{\mathrm{E}}^{\mathrm{e}} - \mathrm{T}^{\mathrm{p}} : \dot{\mathrm{H}}^{\mathrm{p}} - S : \mathrm{curl}\dot{\mathrm{H}}^{\mathrm{p}} \le 0 \tag{52}$$

which finally leads to the constitutive relation for the micro stress S,

$$S = \frac{\partial \psi(\mathrm{E}^{\mathrm{e}}, \mathrm{G})}{\partial \mathrm{G}} \tag{53}$$

In order to introduce the strain gradient effect, Gurtin (2004) rewrite the Eq. (51) by a more general relation

$$W = \int (\mathrm{T} : \dot{\mathrm{E}}^{\mathrm{e}} + \mathrm{T}^{\mathrm{p}} : \dot{\mathrm{H}}^{\mathrm{p}} + K \vdots \nabla \dot{\mathrm{H}}^{\mathrm{p}})\, dV \tag{54}$$

where $K \vdots \nabla \dot{\mathrm{H}}^{\mathrm{p}} = K_{ijk}\, \dot{H}^{P}_{ij,k}$. The free-energy inequality (52) is then rewritten as

$$\mathrm{T}^{\mathrm{p}} : \dot{\mathrm{H}}^{\mathrm{p}} + R \vdots \nabla \dot{\mathrm{H}}^{\mathrm{p}} \ge 0 \tag{55}$$

where T^{p} and R are given as

$$\mathrm{T}^{\mathrm{p}} = Y(d^{\mathrm{p}})(\dot{\mathrm{E}}^{\mathrm{p}} + \chi \dot{\Omega}^{\mathrm{p}}), \quad R = Y(d^{\mathrm{p}}) h^2 \nabla \dot{\mathrm{E}}^{\mathrm{p}}. \tag{56}$$

The parameter Y is dependent on the effective strain rate $d^{\mathrm{p}} = \sqrt{(\dot{\mathrm{E}}^{\mathrm{e}})^2 + \kappa(\dot{\Omega}^{\mathrm{p}})^2}$ with the constant $\kappa \geqslant 0$. Submitting Eq. (56) into the micro force balance yields the flow rule

$$\mathrm{T}' = \underbrace{\mathrm{dev}\,\mathrm{curl}(S^T)}_{1} + \underbrace{Y(d^{\mathrm{p}})(\mathrm{E}^{\mathrm{p}} - \kappa\,\Omega^{\mathrm{p}}) - \mathrm{div}[Y(d^{\mathrm{p}})h^2\nabla\dot{\mathrm{E}}^{\mathrm{p}}]}_{2} \tag{57}$$

where T' is the deviatoric stress. Term 1 at the right side of Eq. (54) corresponds to the hardening due to energetic backstress, while term 2 corresponds to the dissipative hardening which is dependent on the rate of strain gradient $\nabla\dot{\mathrm{E}}^{\mathrm{p}}$.

2.7 Fleck and Willis (2009b)

Fleck and Willis (2009b) considered a continuum plasticity model with the presence of interfaces. For simplicity, here we disregard the interfaces. For the bulk material, Fleck and Willis (2009b) proposed a free energy potential in the form

$$\psi = \psi_{\mathrm{e}}(\varepsilon^{\mathrm{e}}) + \psi_{\mathrm{h}}(\varepsilon^{\mathrm{p}}, \nabla\varepsilon^{\mathrm{p}}) \tag{58}$$

where $\varepsilon^{\mathrm{e}}, \varepsilon^{\mathrm{p}}$ are the elastic strain and plastic strain, $\nabla\varepsilon^{\mathrm{p}}$ is the plastic strain gradient. The energetic stresses $\sigma^{\mathrm{E}}, \tau^{\mathrm{E}}$ are defined as

$$\sigma^{\mathrm{E}} = \partial\psi_h / \partial\varepsilon^{\mathrm{P}}, \qquad \tau^{\mathrm{E}} = \partial\psi_h / \partial(\nabla\varepsilon^{\mathrm{P}}) \tag{59}$$

The free energy inequality can be written as

$$\sigma^{\mathrm{D}} : \dot{\varepsilon}^{\mathrm{p}} + \tau^{\mathrm{D}} : \nabla\dot{\varepsilon}^{\mathrm{p}} \geq 0 \tag{60}$$

where $\sigma^{\mathrm{D}}, \tau^{\mathrm{D}}$ are the dissipative stresses which have the following relation with the energetic stresses:

$$\sigma^{\mathrm{D}} = \sigma - \sigma^{\mathrm{E}}, \qquad \tau^{\mathrm{D}} = \tau - \tau^{\mathrm{E}} \tag{61}$$

Fleck and Willis (2009b) admit a viscoplastic model with higher order dissipation mechanisms, for which they suggest a power-law potential of the form

$$\phi = \frac{\sigma_0 \dot{\varepsilon}_0}{N+1}\left(\frac{\dot{E}^{\mathrm{p}}}{\dot{\varepsilon}_0}\right)^{N+1} = \frac{\Sigma \dot{E}^{\mathrm{p}}}{N+1} \tag{62}$$

Where $\dot{E}^{\mathrm{p}}$ is an overall effective strain rate which has the form $(\dot{E}^{\mathrm{p}})^2 = A_{IJ}\,\dot{e}_I\,\dot{e}_J$, where $\dot{e}_I$ is a 20-dimensional vector which is defined as $(\dot{e}_I) = (\dot{\varepsilon}_{ij}^{\mathrm{p}}, \dot{\varepsilon}_{ij,k}^{P})$. Meanwhile, the vector work-conjugate with $\dot{e}_I$ is defined as $(r_I) = (\sigma_{ij}, \tau_{ijk})$ which can be divided into an energetic part (r_I^E) and a dissipative part (r_I^D).

In Eq. (62), Σ is given as $\Sigma = \sigma_0(\dot{E}^{\mathrm{p}}/\dot{\varepsilon}_0)^N$, then the constitutive relation is

$$r_I^D = \frac{\partial \phi}{\partial \dot{e}_I} = \frac{\Sigma}{\dot{E}^{\mathrm{p}}} A_{IJ}\,\dot{e}_J \tag{63}$$

There is a controversial issue regarding the additional strength due to GNDs whatever it is energetic or dissipative. Gurtin (2004) argued that the density of GNDs is quantified by Nye's tensor (shown experimentally by Man et al., 2010) that leads to increase in the free energy. However, Fleck and Willis (2009a) assumed that the core energy of dislocations stored during plastic deformation is much smaller than the plastic work dissipated during dislocation motion. Based on this observation they concluded that both statistically stored and geometrically necessary dislocations contribute more to the plastic dissipation than to the energy storage. Bardella and co-workers (Bardella, 2006, 2007; Bardella and Giacomini, 2008) also pointed out that modeling involving only energetic material length scales may not be sufficient to describe the size effects exhibited in metals. He reasoned the fact that energetic length scales, defined through a

function of Nye's dislocation density tensor, can only describe the increase in strain hardening accompanied with diminishing size, but cannot capture the related hardening. Bardella (2006, 2007) proposed that at least one dissipative length scale is required in modeling in order to predict the hardening effect.

In the strain gradient theories listed above, the CMSG theory proposed by Huang et al. (2004) could be the simplest one and therefore is easy for application. Unlike the higher order theories of strain gradient plasticity, CMSG does not involve the higher order stress such that the equilibrium equations and boundary conditions are the same as the classical plasticity theories. Only the constitutive model is modified to account for the plastic strain gradient effect. Therefore, CMSG does not require new finite elements (while the aforementioned higher order theories do), and it is easy and straightforward to implement CMSG in the finite element program by only using conventional finite elements. In fact, CMSG has been implemented into the ABAQUS finite element program through a user defined material subroutine UMAT. It has been shown that CMSG agrees well with the aforementioned micron and submicron scale experiments, such as micro-torsion and micro-bend experiments (Huang et al., 2004), cleavage cracking in ductile materials (Qu et al., 2004a), and particle-reinforced composite materials (Qu et al., 2005).

In the following, we will apply the CMSG theory to study some interesting issues related to the surface texturing of metallic material, e.g. the indentation on a rough surface, the rolling process of sheet metal and the surface texturing on a tensile specimen.

Chapter 3: The effect of rough surface on the indentation hardness

In this chapter, we carry out a detailed numerical study of the effect of rough surface on nano-indentation hardness.

3.1 Finite element model of nano-indentation

The computational model for nano-indentation involves a conical indenter and the indented material with a rough surface (Fig. 3.1). The conical indenter is assumed to be rigid and axisymmetric. The cone angle of the indenter is 70.3°, which is the equivalent angle for the Berkovich indenter. For simplicity, the rough surface is modeled as a regular wavy surface which has a sine profile. Contact between the indenter and the indented material is modeled by the finite sliding, hard contact model in ABAQUS. Both frictionless contact and frictional contact are included in our model.

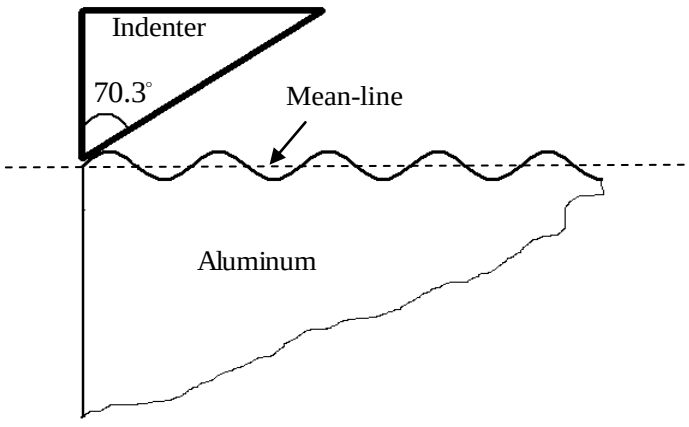

Figure 3.1: A schematic diagram of the indentation model.

3.2 Results and discussion

3.2.1 Material properties of aluminum

The indented material for our simulation is aluminum. The relation between flow stress σ_{flow} and plastic strain ε^{p} in uniaxial tension can be generally expressed via the power law as

$$\sigma_{flow} = \sigma_Y (1 + \frac{E\varepsilon^p}{\sigma_Y})^n \tag{64}$$

The material properties are as follows: The Young's modulus $E = 73\,\text{GPa}$, Poisson's ratio $v = 0.33$, plastic work hardening exponent $n = 0.1$, rate-sensitivity exponent $m = 20$, the initial yield stress is $\sigma_Y = 213\,\text{MPa}$. As reported by Zhang et al. (2007), the empirical coefficient α and Burgers vector b in Taylor dislocation model (37) are 0.248 and $0.283\,\text{nm}$ respectively.

3.2.2 Nano-indentation hardness

Fig. 3.2 shows the geometry and mesh for the sine surface with different aspect. The sine function for the initial surfaces in Fig. 3.2 can be written as $y = \delta_0 \sin\frac{2\pi x}{\lambda}$, where δ_0 represents the wave amplitude and λ is the wavelength. In Fig. 3.2, The wave amplitude is $\delta_0 = 10nm$; while λ are equal to $100\,nm$, $400\,nm$ and $800\,nm$ respectively. Therefore, the sine surfaces in Fig. 3.2 have different aspect ratios of wavelength to wave amplitude: λ/δ_0 = 10, 40 and 80 respectively. The mesh size in the surface region is sufficiently small in order to accurately predict the deformed surface during indentation. The size of smallest element is 10nm in the rough surface. Far away from the surface, the

axisymmetric infinite elements are used. It seems that, the numerical results predicted by CMSG theory are sensitive to the mesh size. When the smallest size of elements is reduced, the results would become higher. Therefore, we used the mesh with fixed size in the following study.

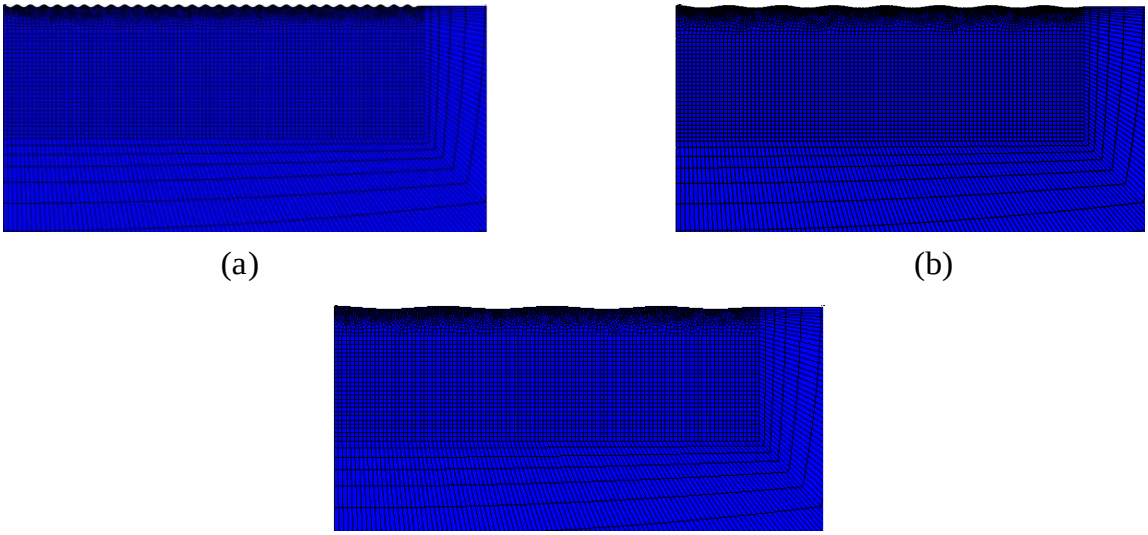

(a) (b)

(c)

Figure 3.2: The geometry and mesh for the rough surface with sine profile. The wave amplitude is $\delta_0 = 10nm$, while the wavelength equals to (a) $\lambda = 100nm$, (b) $\lambda = 400nm$, (c) $\lambda = 800nm$.

Fig. 3.3 shows the predicted contours of the equivalent plastic strain ε^p underneath the indenter for the rough surface with different wavelengths. It is seen that the contours of ε^p for different wavelengths are very similar, and almost have the same maximum value of ε^p (around 2.0) in the region close to the indenter tip for the indentation depth $h = 1000nm$ $(1\mu m)$.

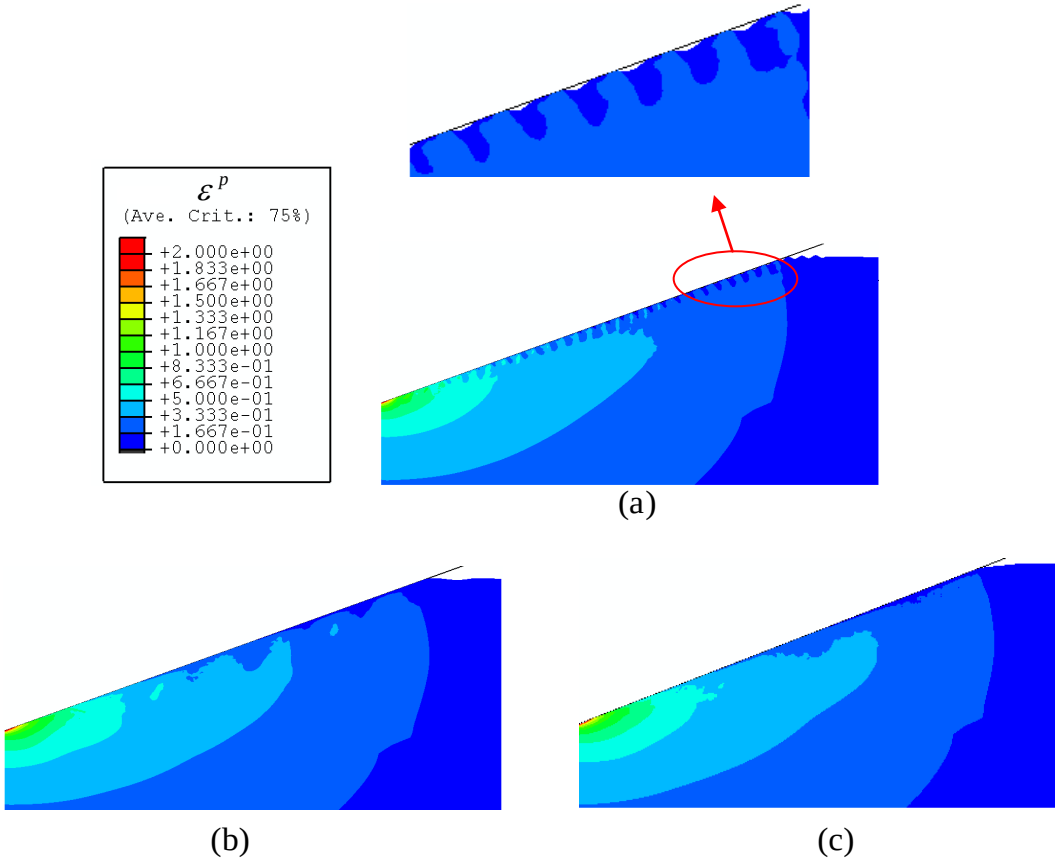

Figure 3.3: The predicted contours of the equivalent strain ε^p for the rough surface with wavelength equal to (a) $\lambda = 100nm$, (b) $\lambda = 400nm$, (c) $\lambda = 800nm$. The wave amplitude is $\delta_0 = 10nm$.

Fig. 3.3a also shows the magnified image of the deformed surface which clearly shows that the peaks on the rough surface have been flattened by the indenter. However, there still exist gaps between the indenter and the rough surface, while the rough surface is totally flattened and a complete contact between the indenter and the deformed surface could be achieved for wavelengths $400nm$ and $800nm$.

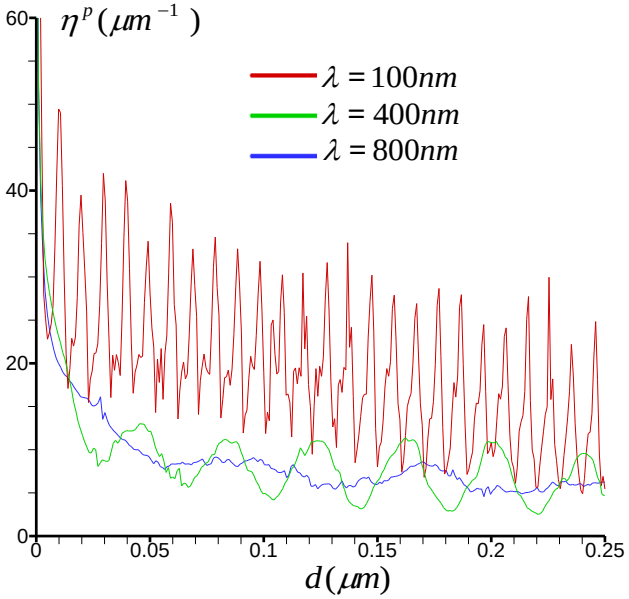

Fig. 3.4 The predicted equivalent plastic strain gradient η^p vs. the length along the indenter face d

Fig. 3.4 shows the predicted equivalent plastic strain gradient η^p for the rough surface with different wavelengths. It is seen that, the values of η^p for wavelength $\lambda = 100nm$ show significant oscillation, and the average value of η^p along the indenter face is in the range 20-30 μm^{-1}; while the average value of η^p is only around 10 μm^{-1} for wavelength $\lambda = 400nm$ and $\lambda = 800nm$. Therefore, the indented peaks become harder for $\lambda = 100nm$ due to a lager strain gradient. That is why the peaks in Fig. 3.3a could not be totally flattened.

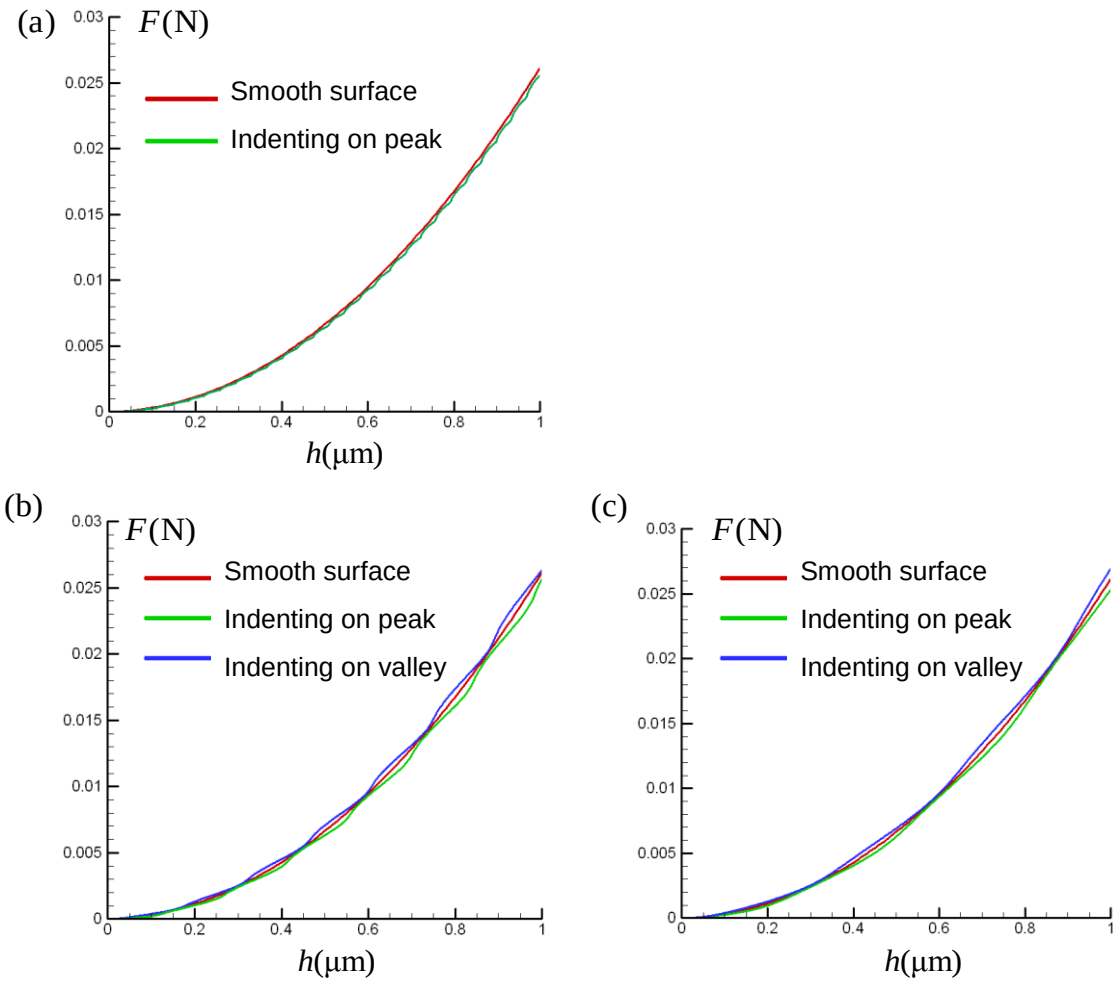

Figure 3.5: The predicted contact force F vs. the indentation depth h by strain gradient plasticity theory for the wavelength equal to (a) $\lambda = 100nm$, (b) $\lambda = 400nm$, (c) $\lambda = 800nm$. The wave amplitude is $\delta_0 = 10nm$.

Fig. 3.5 shows the predicted contact force F vs. the indentation depth h by strain gradient plasticity theory for the rough surfaces with different wavelengths. For comparison, the contact force for indenting on a smooth surface is also presented in the Figures by the red line. The indentation depth h is defined as the displacement of the initial contact point between the indenter tip and the surface. It should note that, there are

different indentation positions for indenting on a rough surface. The indenter tip could possibly indent on the peak, the valley or other positions of a rough surface. But, for the rough surface with a small wavelength ($\lambda < 200nm$), the indenter tip is not able to reach the valley. Therefore, Fig. 3.5a only shows the contact force for indenting on the peak of the rough surface with wavelength $\lambda = 100nm$; while Fig. 3.5b and Fig. 3.5c show the contact force for indenting on both peak and the valley for $\lambda = 400nm$ and $\lambda = 800nm$, respectively. It is interesting to see that, the curves for indenting on rough surface show significant oscillation, and the oscillation period is corresponding to the wavelength of the sine surface. The curve for indenting on the peak is below the curve for smooth surface, while the curve becomes higher when indenting on the valley. This is because of the differences in the areas of contact for the peak and valley indentations. For the peak indentation, the contact area is smaller, leading to smaller force values and vice versa for valley indentations.

To make accurate prediction of the indentation hardness, the contact areas of the indentations must be precisely measured. The contact area for the conical indenter with cone angle 70.3° can be obtained by the following function: $A_c = 24.5h_c^2$, which gives the same contact area as the Berkovich indenter at the same contact depth. The contact depth h_c is usually determined by the Oliver–Pharr method during the indentation experiment. In finite element simulation, the actual contact area could be output directly by ABAQUS/Standard. It should pointed out that, the actual contact area output from ABAQUS is exactly the area measured by using the experiment method (Oliver and

Pharr, 1992) only for a completely flattened rough surface. Otherwise, the actual contact area would be smaller than the experimentally measured value.

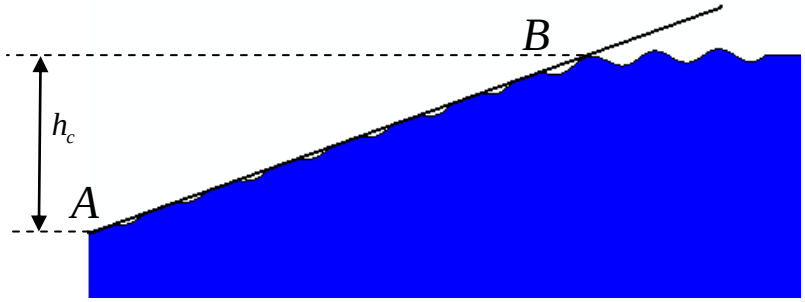

Figure 3.6: The schematic representation of the contact area between the indenter and the rough surface.

Fig. 3.6 shows the schematic representation of the contact area between the indenter and the rough surface. In Fig. 3.6, point A is located on the indenter tip, and point B is on the perimeter of the contact. The contact depth h_c is defined as the vertical distance between point A and B. Therefore, the contact area calculated by the formula $A_c = 24.5h_c^2$ should be the project area of the entire region between point A and the perimeter of contact. However, for the rough surface with small wavelength (e.g. $\lambda = 100nm$), Fig. 3.6 clearly shows that the actual contact area A_c' less than the experimentally measured area A_c due to the gap between the indenter and the deformed surface.

Fig. 3.7 shows the predicted contact area A_c vs. the indentation depth h by strain gradient plasticity theory for the rough surface with different wavelengths. The contact area for indenting on smooth surface is also shown by the red line. Similar to the curves of contact force in Fig. 3.5, the curves of the contact area show significant oscillation for

indenting on rough surfaces. The indentation position also has influence on the contact area. Fig. 3.7b and Fig. 3.7c show that the curves for indenting on the peak and the valley distribute at two sides of the red curve.

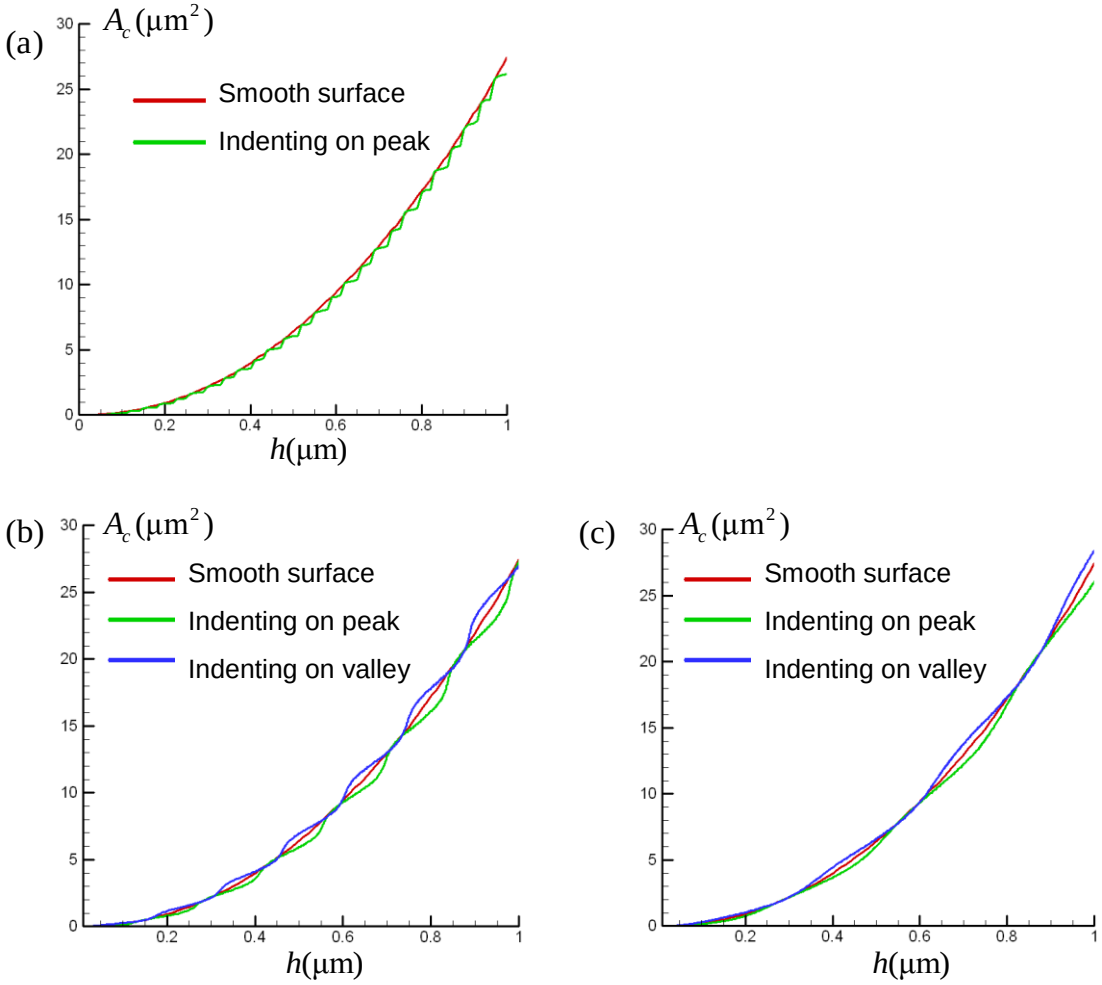

Figure 3.7: The predicted contact area A_c vs. the indentation depth h by strain gradient plasticity theory for the wavelength equal to (a) $\lambda = 100nm$, (b) $\lambda = 400nm$, (c) $\lambda = 800nm$. The wave amplitude is $\delta_0 = 10nm$.

Fig. 3.8 shows the predicted hardness $H\ (= F / A_c)$ vs. contact depth h_c by strain gradient plasticity theory for different wavelengths. The red dashed line is for the

hardness of indenting on smooth surface. Fig. 3.8b and Fig. 3.8c show that both the curves of the hardness for indenting on peak and valley oscillate around the red dashed line. It means that the measured hardness on the rough surface could either higher or lower than

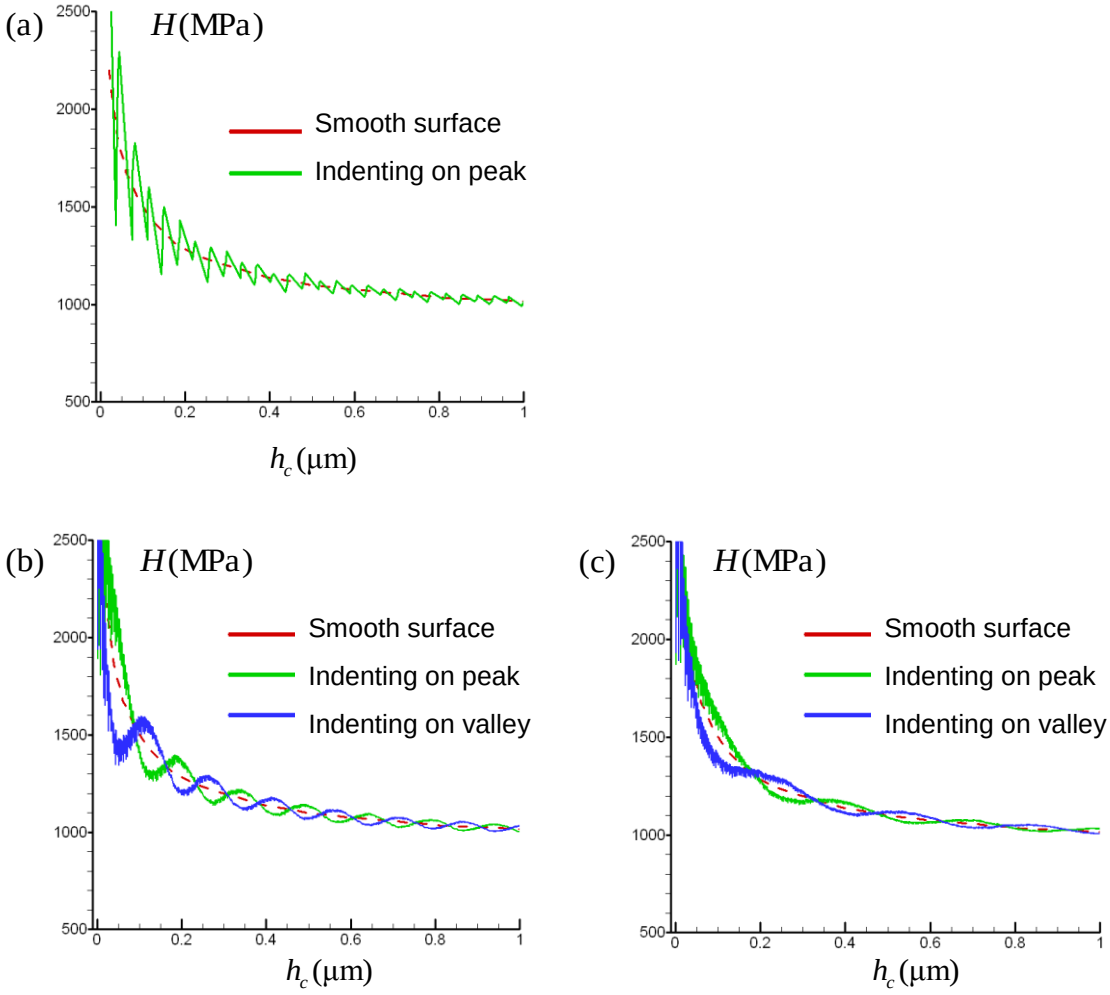

Figure 3.8: The predicted hardness H vs. contact depth h_c by strain gradient plasticity theory for the wavelength equal to (a) $\lambda = 100nm$, (b) $\lambda = 400nm$, (c) $\lambda = 800nm$. The wave amplitude is $\delta_0 = 10nm$.

that of smooth surface no matter where the indentation position is located. The frequency of the oscillation is corresponding to the wavelength of the rough surface. The curve in Fig. 3.8a also shows oscillation around the red dashed line, even though the oscillation seems a bit different from those in Fig. 3.8b and Fig. 3.8c. Such a difference is coming from the different methods of obtaining the contact area A_c. As illustrated in Fig. 3.6, for small wavelength $\lambda = 100nm$, the contact depth h_c was first measured and then the contact area was calculated using the formula $A_c = 24.5h_c^2$; while for wavelengths $\lambda = 400nm$ and $800nm$, A_c was obtained directly from ABAQUS.

Fig.3.9 shows the comparison of predicted hardness H for the rough surfaces with different wave amplitudes: $\delta_0 = 10nm$ and $20nm$. It shows that the oscillation amplitude of the hardness increases as δ_0 increases.

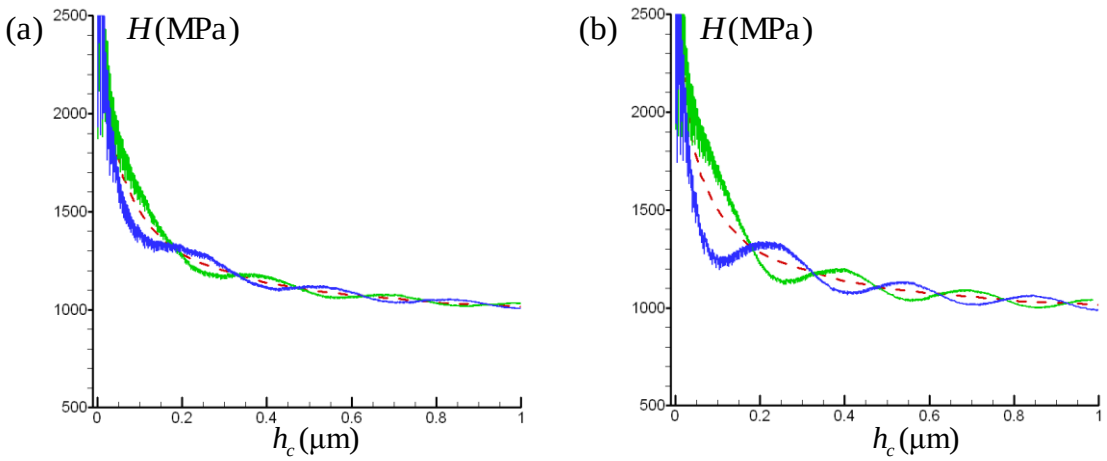

Figure 3.9: The comparison of predicted hardness H vs. contact depth h_c for the wave amplitude equal to (a) $\delta_0 = 10nm$, (b) $\delta_0 = 20nm$. The wavelength is $\lambda = 800nm$.

Fig.3.5, 3.7-3.9 were obtained by assuming a frictionless interface between the indenter and the rough surface. Fig. 3.10 shows the predicted hardness H for the rough surfaces with considering friction. The red dashed line shows the hardness of smooth surface without friction; while the red solid line is for the case with friction. It is clear that, when considering friction, the hardness of the smooth surface becomes higher compared to that without friction; the hardness for rough surface still shows oscillation around the hardness of the smooth surface.

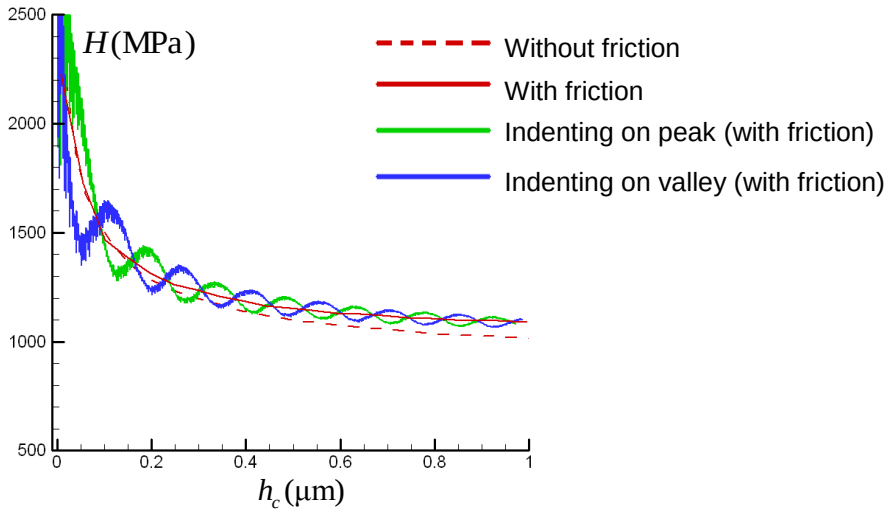

Figure 3.10: The predicted hardness H vs. contact depth h_c for the rough surface with considering friction. The frictional coefficient $\mu = 0.2$. The wave amplitude equals to $\delta_0 = 10nm$, and the wavelength is $\lambda = 400nm$.

The above results are all based on the rough surface with single wavelength. However, a real surface ususlly includes a multiude of different wavelengths with one or two having dominant effect. The function of the rough surface with mutiple wavelength can be expressed as $y = \sum_{i=1}^{n} \delta_i \sin \frac{2\pi x}{\lambda_i}$. Fig. 3.11 shows geometry and mesh for the rough

surfaces with multiple wavelengths. Both the rough surfaces in Fig.3.11a and Fig. 3.11b have two wavelengths, and both have the wavelength $\lambda_1 = 1.6\mu m$. For comparison, the rough surface with only $\lambda_1 = 1.6\mu m$ is considered in Fig. 4.11c.

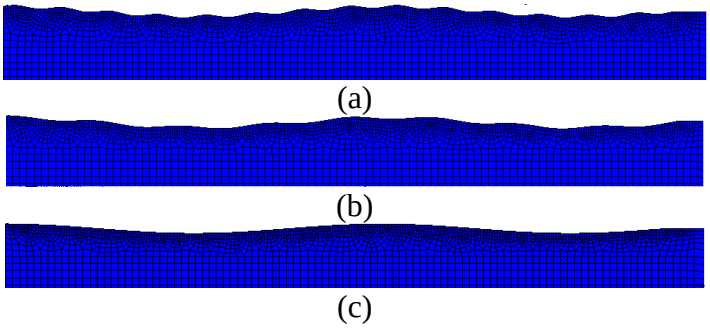

Figure 3.11: The geometry and mesh for the rough surface with a multitude of different wavelengths: (a) with wavelengths $\lambda_1 = 1.6\mu m$ and $\lambda_2 = 0.2\mu m$; (b) with wavelengths $\lambda_1 = 1.6\mu m$ and $\lambda_2 = 0.4\mu m$; (c) only with wavelength $\lambda_1 = 1.6\mu m$. The wave amplitude equals to $\delta_0 = 10nm$

Fig. 3.12 shows the predicted hardness H for the rough surfaces with multiple wavelengths. Similar to the previous results, the hardness of the rough surface shows oscillation around the hardness of the smooth surface. Fig. 3.12a and Fig. 3.12b show that the oscillation of the hardness includes multiple frequencies which correspond to the wavelengths of the rough surface.

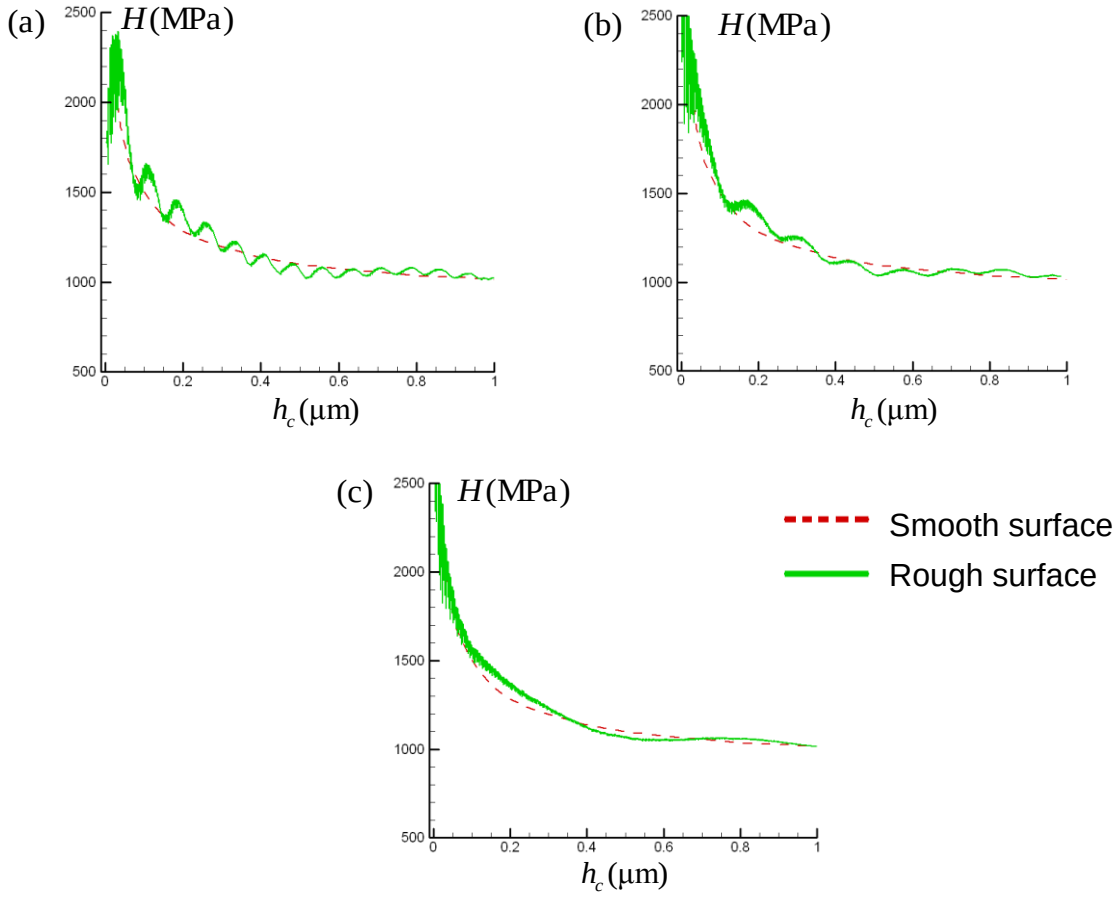

Figure 3.12: The predicted hardness H vs. contact depth h_c for the rough surface with a multitude of different wavelengths as shown in Figure 18.

Fig. 3.13 shows the predicted hardness H of the rough surfaces by conventional plasticity theory. The red dashed line is the hardness of the smooth surface, and shows a constant value around 820 MPa (In Fig. 3.8, when the indentation depth is extended to larger than 1000 μm, the hardness of the smooth will be close to 820 MPa as well).

It is clear that, the hardness of the rough surface also shows oscillation around the hardness of the smooth surface. It is interesting to see that, the hardness for indenting on peak and valley predicted by conventional plasticity theory is significantly lower at

shallow indentation depth (h_c less than 0.2 μm), and the overall profiles show the trend of increase with the indentation depth; while the overall profiles predicted by strain gradient plasticity shows the opposite trend. The reason can be explained as follows: The simulation for the nano-indentation has instability at the beginning and the results for the hardness at h_c less than 0.2 μm are not reliable.

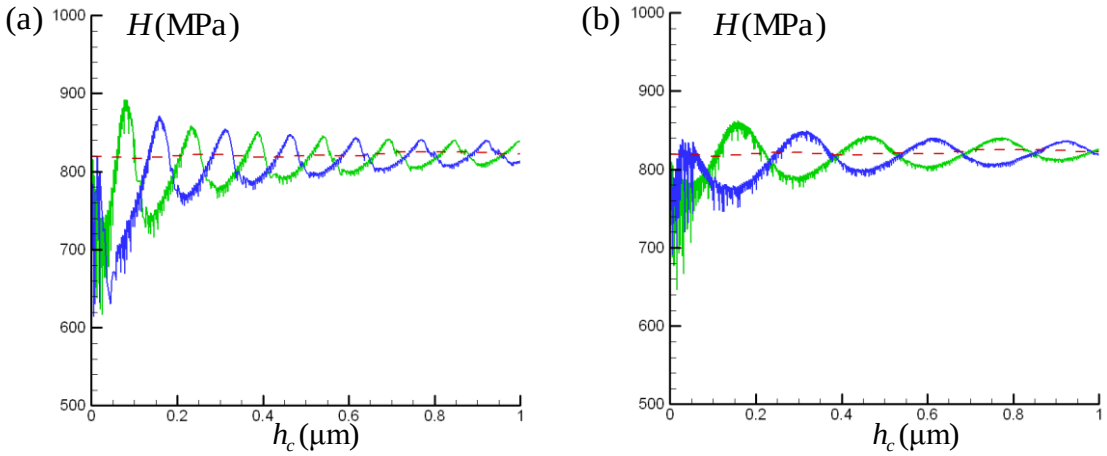

Figure 3.13: The predicted hardness H vs. contact depth h_c by conventional plasticity theory for the wavelength equal to (a) $\lambda = 400nm$, (b) $\lambda = 800nm$. The wave amplitude is $\delta_0 = 10nm$.

Some further discussion is presented in the following. As aforementioned, for the rough surface with small wavelength, the surface cannot be completely flattened by the indenter. Therefore, the actual contact area A_c' is less than the experimentally measured area A_c. Fig. 3.14a shows the actual contact area A_c' for wavelength $\lambda = 100nm$; Fig. 3.14b shows the predicted hardness H' based on the actual contact area. It is seen that, H' is higher than the hardness of the smooth surface during the entire range of the indentation depth. This is because the indented peaks become much harder due to strong

strain gradient effect as shown in Fig. 3.3a. It is to be noted once again that the curve for indenting on the peak is below the curve for smooth surface, while the curve becomes higher when indenting on the valley. The explanation for this was provided earlier.

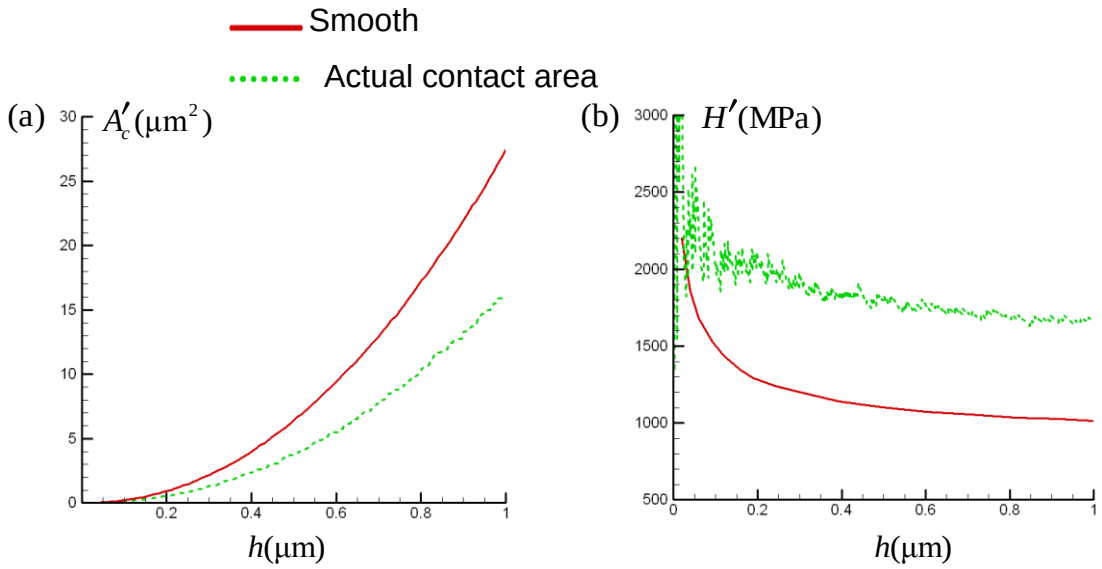

Figure 3.14: The predicted (a) actual contact area A_c' and (b) hardness H' vs. the indentation depth h for the wavelength equal to $\lambda = 100nm$. The wave amplitude is $\delta_0 = 10nm$.

Chapter 4: The effect of textured surface on the necking of tensile sheet

In this chapter, we concerned about the effect of change in the material property on the surface region via surface texturing on the onset of necking. During surface texturing, the stiffness of the material on the surface region could be increased due to strain and strain gradient hardening, resulting in the delay in the onset of necking for the whole sheet.

A finite element model is developed to simulate the tensile test of the sheet with smooth surface and textured surface. A textured surface is prepared through the indention on the sheet surface. The indentation depth is less than 1% of the sheet thickness in order not to change the total mechanical property of the sheet. The strain gradient plasticity theory (CMSG) is used in our model to predict the gradient effect during surface texturing and subsequent tensile deformation.

4.1 Finite element model of tensile test

The equilibrium equations, strain–displacement relation, and boundary conditions in CMSG are identical to those in the classical theory of plasticity. Only the constitutive model is modified to account for the effect of plastic strain gradient, which is implemented in the ABAQUS finite element program via its USER-MATERIAL subroutine UMAT. The plastic strain gradient is obtained by interpolating the plastic strain increment within each element via the values at Gaussian integration points in the

isoparametric space, and by determining the gradient of plastic strain increment via the differentiation of the shape function.

Figure 4.1 shows the finite element model of surface texturing for the sheet metal with initial length L_0 and initial thickness h_0. The problem is considered as a 2D plane-strain case. The mesh with reduced integration element CPE8R, which has 8 nodes and 4 integration points, is employed in the FE model. The mesh size in the surface region is sufficiently small in order to accurately predict the deformed surface during texturing. The size of smallest element in the sheet surface is 10 nm. As mentioned before, the results predicted by CMSG theory are sensitive to the mesh size. The magnitude of the results would be different by reducing the mesh size, however the trend of the results are always the same.

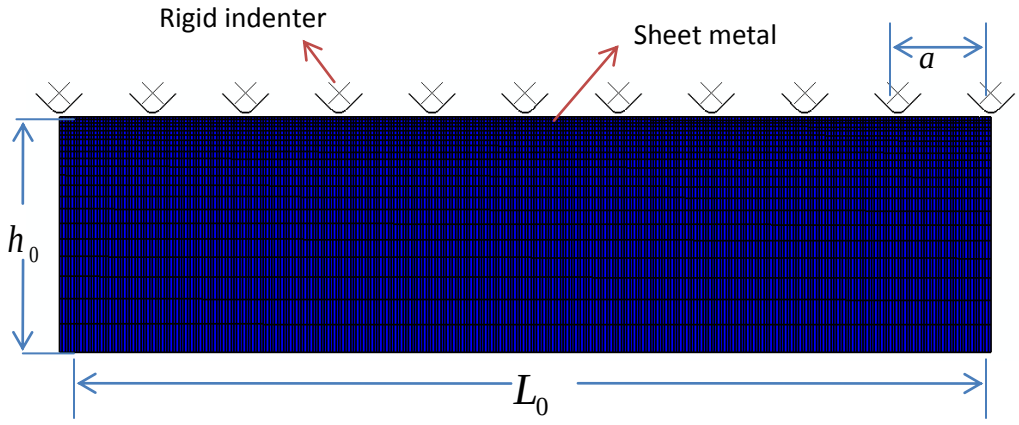

Figure 4.1: The model of surface texturing for the sheet metal.

The surface of the sheet is assumed to be smooth at initial stage. This surface is textured via the indentation with rigid indenters which have spherical tips. The interval between two indenters is noted as a, which determines the number of indentation on the

sheet surface, as shown in Figure 4.1. This indented textured surface is then subjected to uniaxial tension.

In the following, we will study the tensile deformation of the sheet with rigid grips at one end (the other end is the symmetric axis of the sheet). The sheet cannot contract in the direction orthogonal to the tensile direction at the ends so that no initial imperfection is needed for the development of necking. Both of the sheets with smooth surface and textured surface will be studied.

4.2 Results and discussion

4.2.1 Material properties of tensile sheet

The tensile calculation was carried out for the set of parameters: aspect ratio of $L_0 / h_0 = 4$, the interval of the indenter $a = 0.1L_0$, and the radius of indenter $r = 0.01L_0$.

The material behavior of the sheet is described by the power hardening law:

$$\sigma = \sigma_y + k\left(\varepsilon^p\right)^n \tag{65}$$

where the σ_y is the initial yield stress and ε^p is the plastic strain. The material properties used are as follows: the ratio of initial yield stress to Young's modulus $\sigma_y / E = 0.0072$, the Poisson's ratio is $1/3$, the working hardening exponent $n = 0.3$, and the coefficient k in Eqn.(65) is taken to be $k / E = 0.01$. The parameters related to the CMSG theory are the empirical coefficient α and the Burgers vector b in the Taylor dislocation model. Here, we set α and b equal to 0.3 and $0.25\,nm$, respectively.

4.2.2 Tensile test of sheet with textured surface

First, we will study the tensile deformation of the sheet by using the conventional plasticity theory. The initial thickness of the sheet is 10 μm. Figure 4.2 shows the contour of Mises stress for the deformed sheet with rigid grips in uniaxial tension.

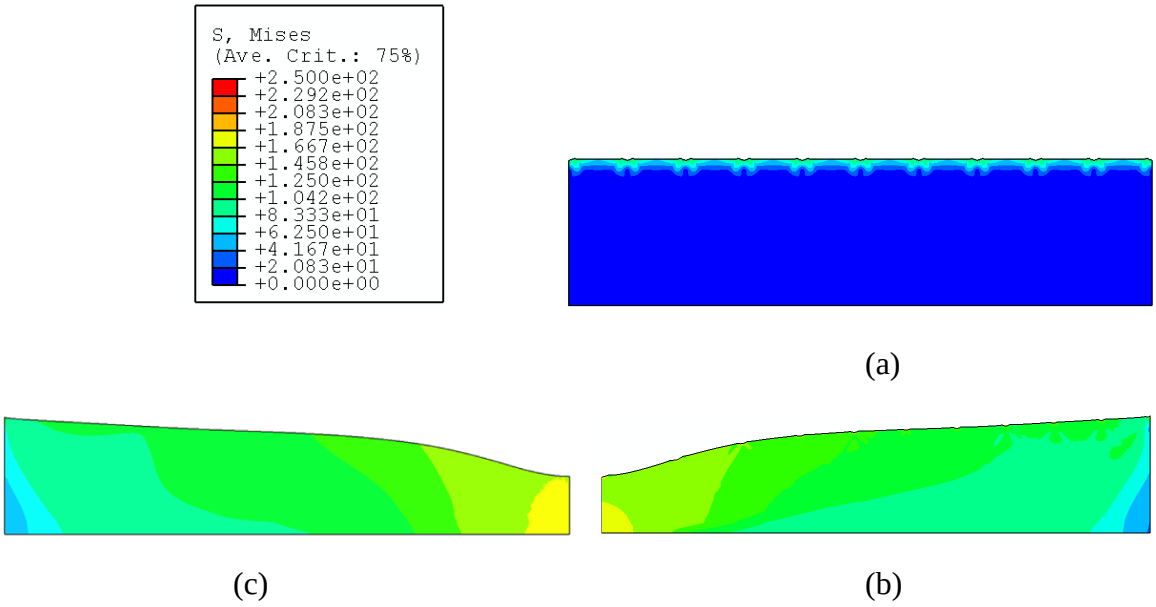

Figure 4.2: The contour of Mises stress for the tensile sheet with rigid grips at the end. (a) The textured sheet without elongation; (b) The textured sheet with elongation $\varepsilon = 0.223$; (c) The sheet with smooth surface at elongation $\varepsilon = 0.223$.

For the tensile test of the sheet with textured surface, the first step is the preparation of textured surface by the indenting process. Fig. 4.2a shows the contour of the textured sheet which has a series of indentations on the surface. The indentation depth d is only 1% of the sheet thickness: $d/h_0 = 1\%$, so that the indentation will not change the total mechanical property of the sheet. As shown in Fig. 4.2a, the residual stress after the indentation is indeed confined in the surface region. Fig. 4.2b shows the deformed

contour of the textured sheet for the stage of elongation at $\varepsilon = 0.223$. For comparison, the deformed contour of the sheet with smooth surface is shown in Fig. 4.2c for the same stage of elongation. Both Fig. 4.2b and Fig. 4.2c show that, neck took place in the region near the symmetric axis of the sheet due to the constraints at the end with rigid grips. The current area of neck is defined as the minimum cross-section area $A_{\min}$.

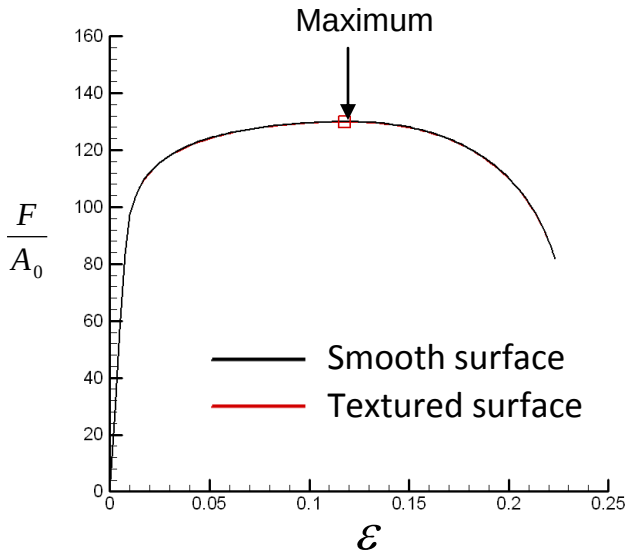

Figure 4.3: The normalized tensile force vs. the true strain ε.

Fig. 4.3 shows the predicted normalized tensile force vs. the true strain ε for the tensile deformation in Fig. 4.2. The true strain ε is defined as $\varepsilon = \ln(1+U/L_0)$, where U is the displacement of the end of the sheet. The black line represents the case of the sheet with smooth surface, while the red line is for the sheet with textured surface. Fig. 4.3 shows that the tensile forces for these two types of surface are quite close, and decrease quickly after the maximum loading point (marked by the square symbol). The necking should occur at the same instant that the load on the sheet reaches the maximum point. So, the true strain at the onset of necking (or the maximum loading point) is about

$\varepsilon_n = 0.117$ for both the sheets with smooth surface and textured surface. Fig. 4.4 shows the normalized minimum area $A_{\min} / A_0$ vs. the true strain ε. The onset point of necking is shown in the Figure as well. In Fig. 4.4, the overlap of the curves for both smooth surface and textured surface reveals that, the textured surface almost has no effect on the development of necking predicted by the conventional plasticity theory.

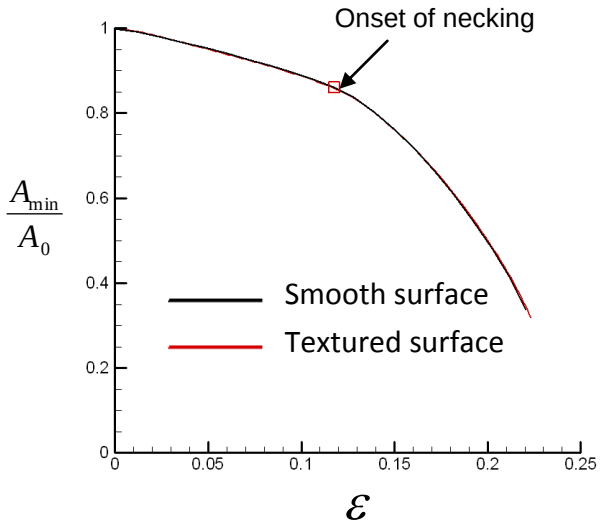

Figure 4.4: The normalized minimum area $A_{\min} / A_0$ vs. the true strain ε.

The tensile deformation of the sheet based on the strain gradient theory has been studied in the following. Two different values of intrinsic material length: l_* / h_0 =0.2 and 0.4 are considered in our simulation.

Figure 4.5 shows the deformed mesh of the sheets with smooth surface and textured surface for different stages of the tensile deformation: $\varepsilon = 0.161$, 0.193 and 0.223. The material length l_* / h_0 =0.4, while the other parameters are the same as those in Fig.4.2. Since the intrinsic material length l_* is usually on the order of micron for most metals, the material with l_* / h_0 =0.4 has the initial thickness on the order of 10 μm.

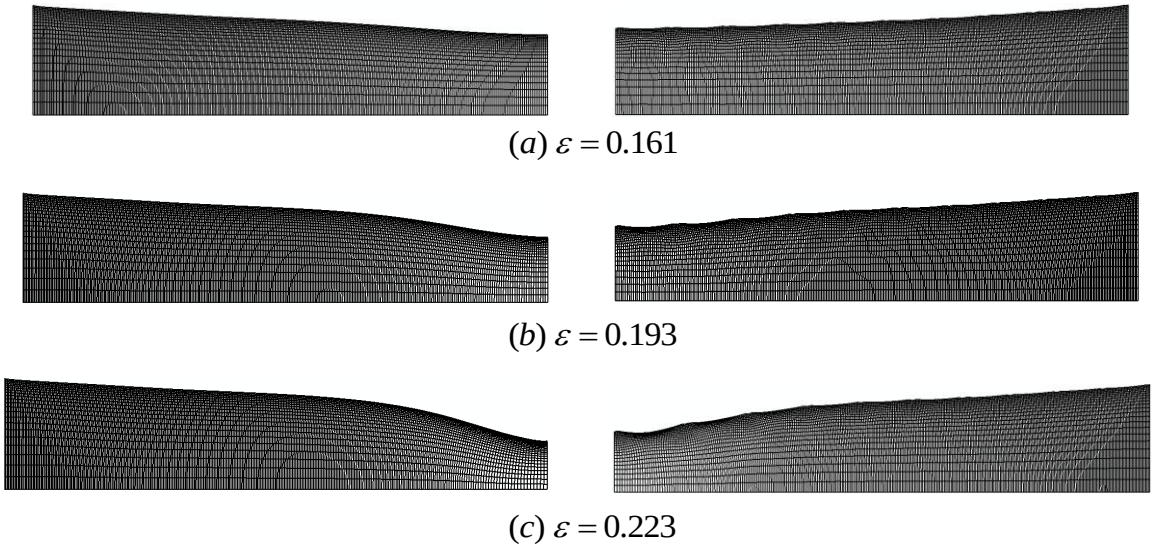

(a) $\varepsilon = 0.161$

(b) $\varepsilon = 0.193$

(c) $\varepsilon = 0.223$

Figure 4.5: Deformed mesh of the sheet with (a) smooth surface (left) and textured surface (right); (b) smooth surface (left) and textured surface (right); (c) smooth surface (left) and textured surface (right).The material length l_* / h_0 =0.4.

Fig. 4.6 shows the plot of the deformed surface profiles of the sheet (with initial thickness $h_0 = 10\mu m$) in Fig. 4.5. The horizontal coordinate x represents the length of the sheet, and the vertical coordinate y represents the thickness of the sheet. It is clear that the sheet with textured surface has a lower tendency to neck compared to the sheet with smooth surface, as shown in Fig. 4.6. This could be explained as follows: the textured surface becomes much harder due to the strong gradient effect in the indentation, and has a significant influence on the delay of necking. It is seen that, a series of tiny necks take place between the indentations for the textured surface. The circle symbols in Fig. 4.6c show the positions at which the minimum area of the neck could be measured.

For the sheet with textured surface, the minimum area does not occur at the symmetric plane of the sheet, but at somewhere between the first two indentations.

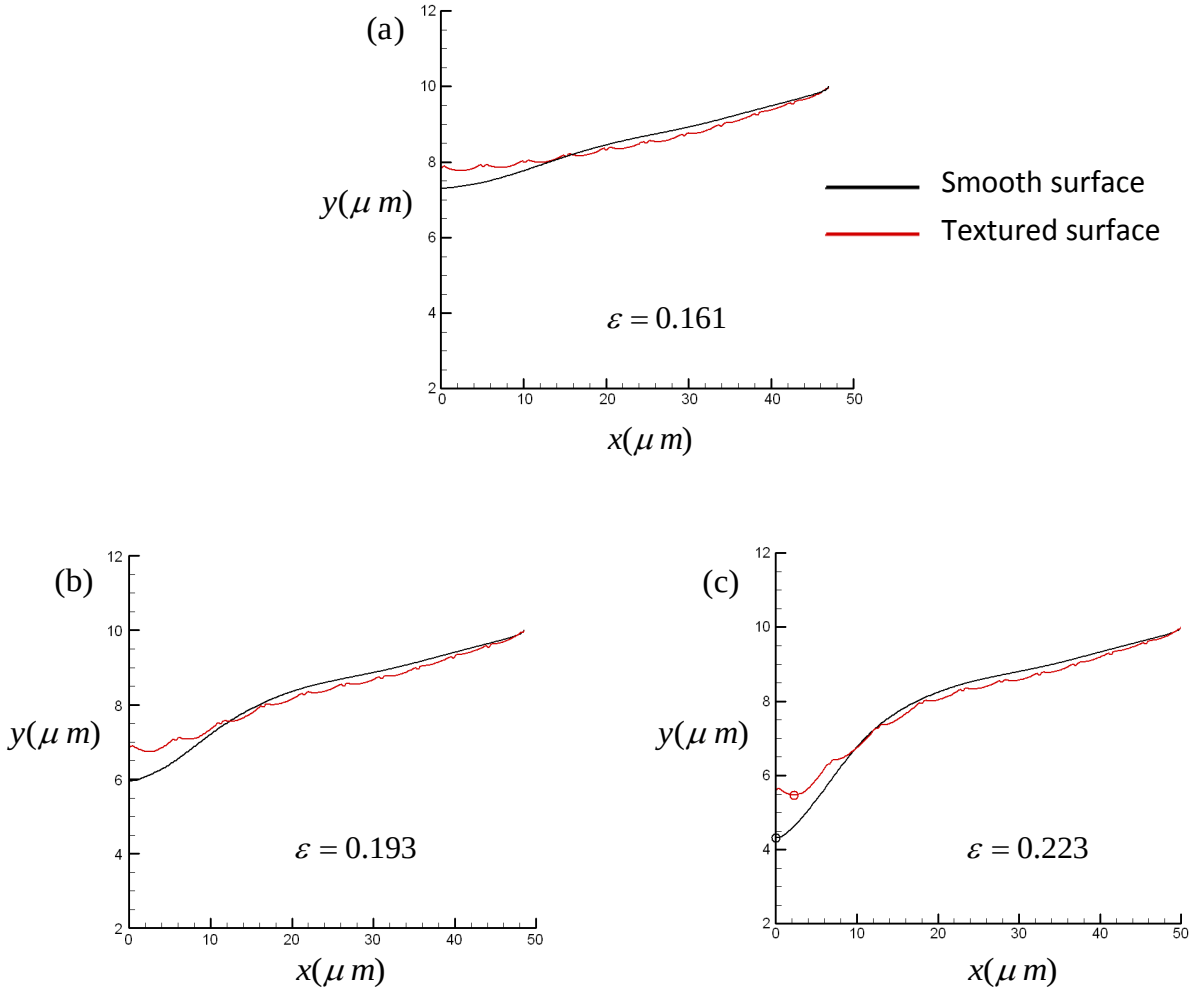

Figure 4.6: The deformed profiles of smooth surface and textured surface.

Fig. 4.7 shows the normalized tensile force F / A_0 and the minimum area $A_{\min} / A_0$ vs. axial strain ε for the intrinsic material length: l_* / h_0 =0.2, and 0.4. In Fig. 3.7a, for l_* / h_0 =0.2, the tensile forces reach the same maximum point (marked by the square

symbol) for both the sheet with smooth surface and textured surface; However, for l_* / h_0=0.4, the maximum loading point occurs at a larger strain for the textured surface

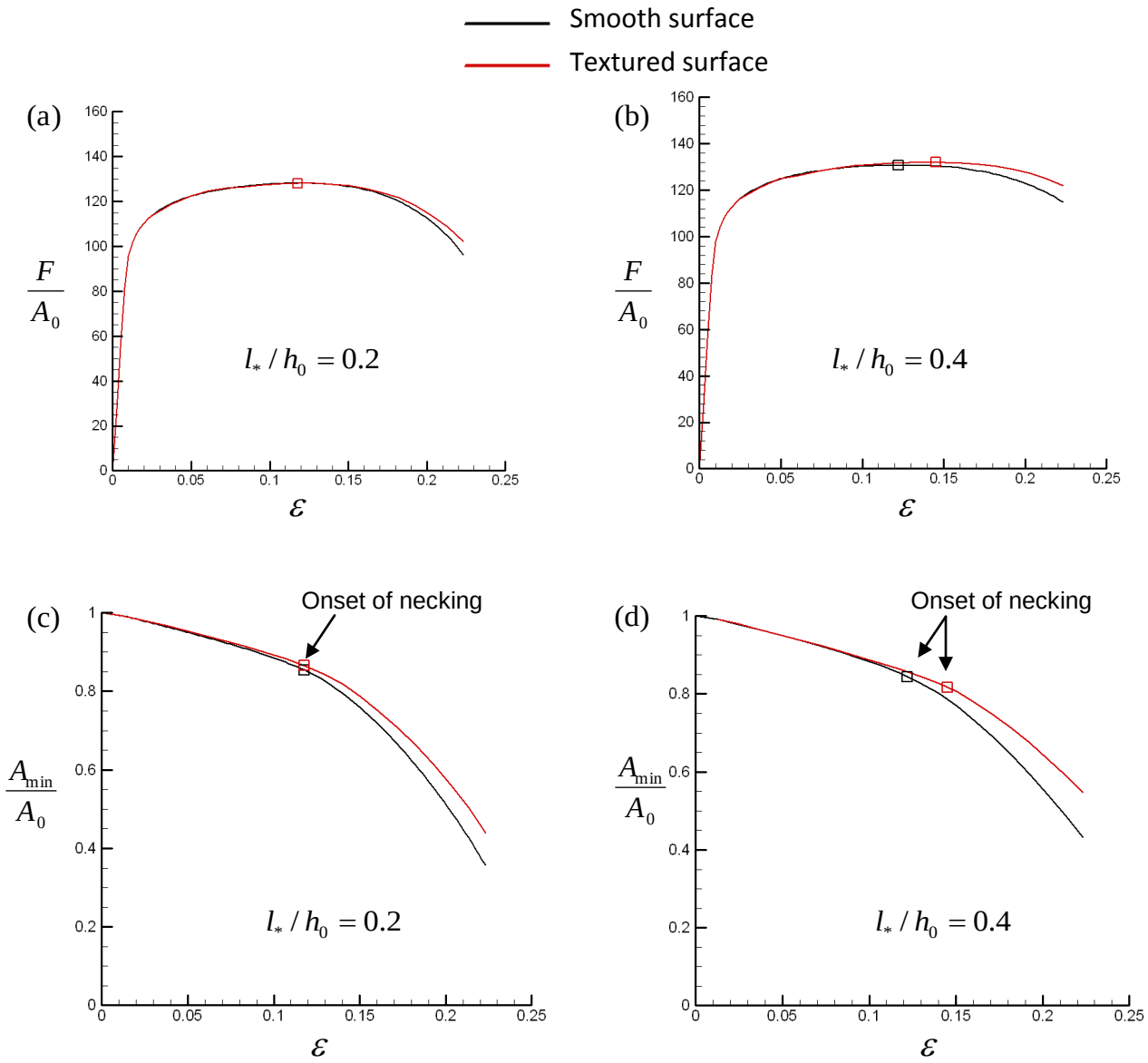

Figure 4.7: The normalized tensile force F / A_0 for (a) l_* / h_0=0.2, (b) l_* / h_0=0.4; and the minimum area A_{min} / A_0 for material length (c) l_* / h_0=0.2, (d) l_* / h_0=0.4.

compared to the smooth surface as shown in Fig. 4.7b. Fig. 4.7c shows that, for l_* / h_0=0.2, the textured surface almost has no influence on the onset of necking (the necking strain $\varepsilon_n = 0.117$, corresponding to the strain at maximum loading point in Fig. 4.7a); while for l_* / h_0=0.4, the textured surface can significantly delay the onset of necking (the necking strain $\varepsilon_n = 0.122$, and 0.145 for smooth surface and textured surface, respectively) as shown in Fig. 4.7d. Fig. 4.7d also shows that the textured surface can significantly delay the decrease of the minimum area $A_{\min}$ at the stage of post-necking.

Fig. 4.8 shows that the normalized tensile force F / A_0 and the minimum area $A_{\min} / A_0$ for different intervals between the indenter: a / L_0=0.05, 0.1 and 0.2. Fig. 4.8a shows the deformed profiles of the sheet surface for the tensile strain $\varepsilon = 0.223$. The positions at which the minimum area located are noted by the circle symbol. Fig. 4.8b shows that the tensile force increases as the interval a / L_0 decreases, because the decrease of the interval implies the increase of the indentation number, and then causes more surface region to be harden. Fig. 4.8c shows that the textured surface with a / L_0=0.1 obviously has a better effect on the delay of necking compared to that for a / L_0=0.2; However, there is almost no difference between the curves for a / L_0=0.05 and a / L_0=0.1. It means that the delay has a limitation for decreasing the interval between the indenter (a / L_0=0.1 could be considered as the critical value for the delay reaches the limitation).

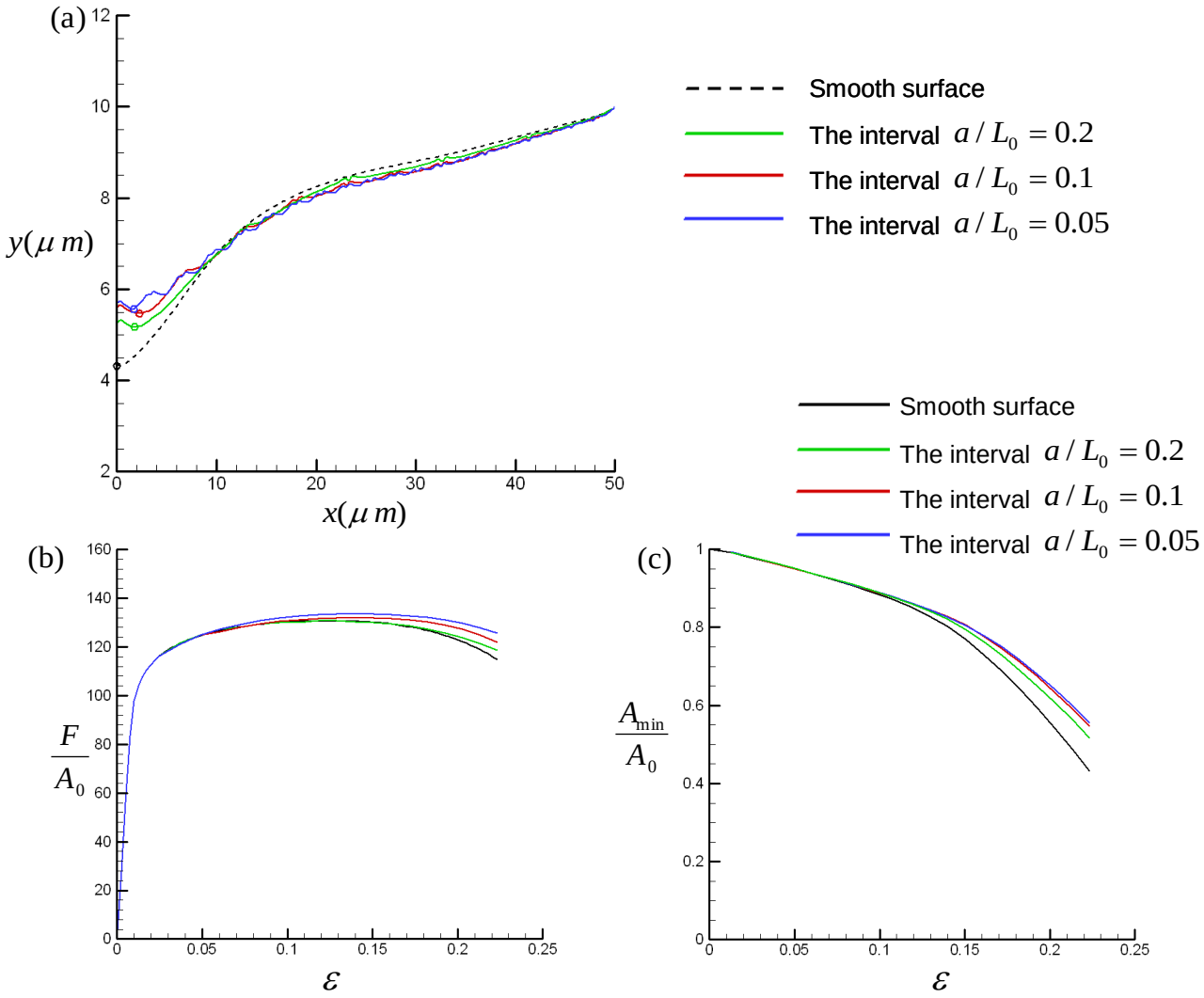

Figure 4.8: The normalized tensile force F / A_0 and the minimum area A_{min} / A_0 for different interval between the indenter: a / L_0=0.05, 0.1 and 0.2. The material length l_* / h_0=0.4.

Fig. 4.9 shows the normalized tensile force F / A_0 and the minimum area A_{min} / A_0 for different radius of the indenter tip: r / L_0=0.01 and 0.05. For comparison, the results for smooth surface are also shown in Fig. 4.9 by the black line. It seems that the change of the tip radius has little effect on the numerical results when the indentation depth keeps

at $d/h_0 = 1\%$. Actually, the deformed elements underneath the indenter with tip radius r/L_0 =0.05 has lower strain gradient value than that for the tip radius r/L_0 =0.01, however, they are sufficiently hard to resist the stretch along the tensile direction (the stretched elements are mainly the ones far away from the indentation). The resistance to stretch for the indented elements could be the main reason for the delay of necking.

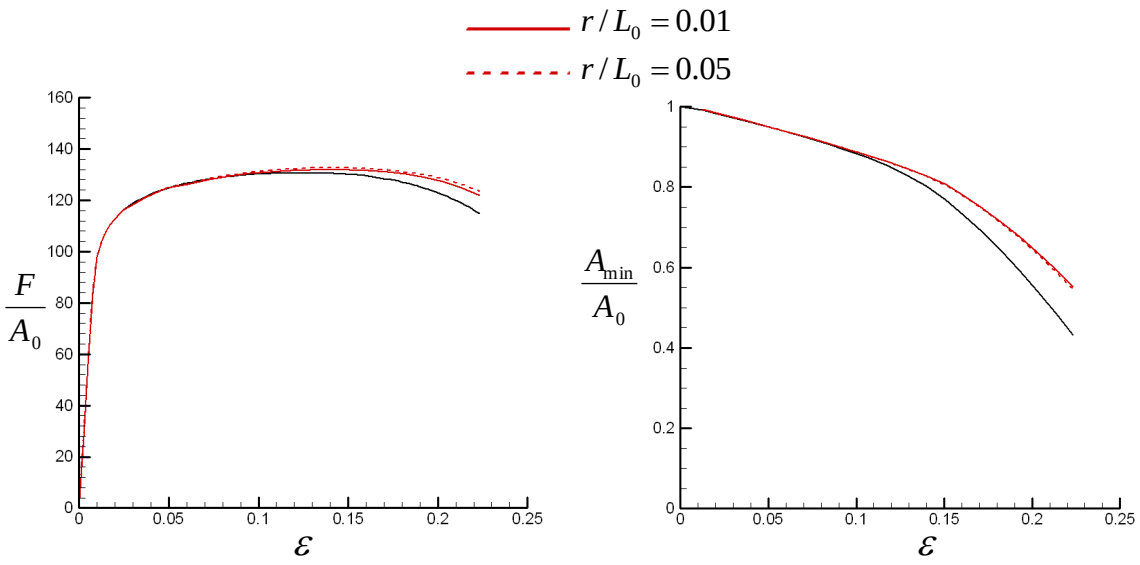

Figure 4.9: The normalized tensile force F/A_0 and the minimum area A_{min}/A_0 for different radius of the indenter tip: r/L_0 =0.01 and 0.05. The material length l_*/h_0 =0.4.

Fig. 4.10 shows the normalized tensile force F/A_0 and the minimum area A_{min}/A_0 for different indentation depth: d/h_0 =1%, 0.5%, and 0.2%. It is seen that, the indentation depth has significant influence on the delay of necking. As the indentation depth decreases, the delay of necking decreases. When the indentation depth decreases to

zero, the results for textured surface degenerate to those for a smooth surface as shown by the black lines in Fig. 4.10.

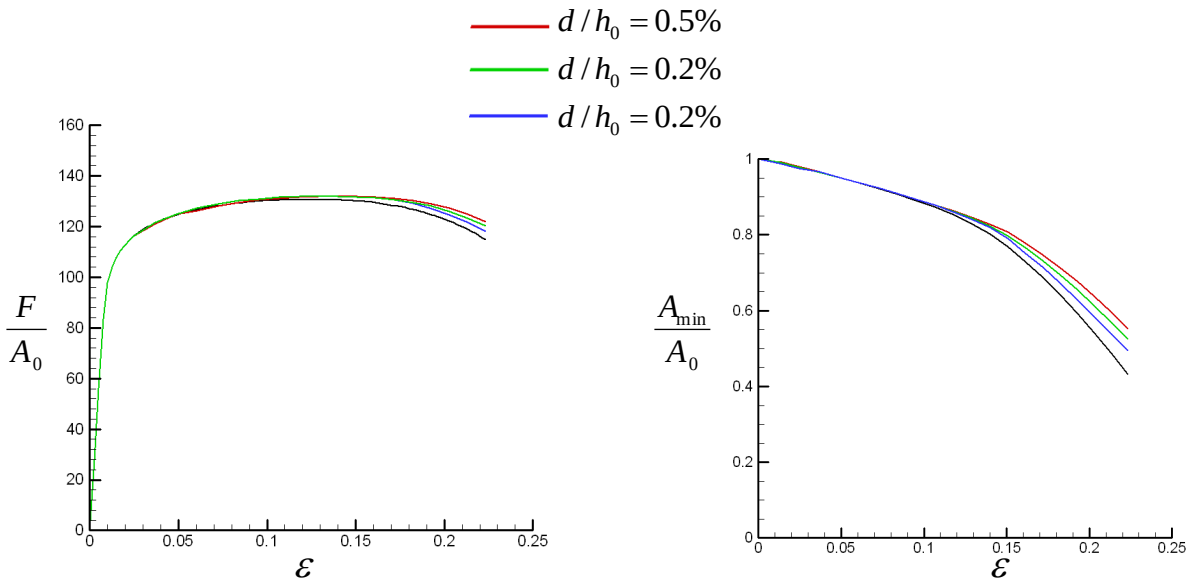

Figure 4.10: The normalized tensile force F/A_0 and the minimum area $A_{\min}/A_0$ for different indentation depth: d/h_0=1%, 0.5%, and 0.2%. The material length l_*/h_0=0.4.

The above results are all obtained based on the case that the indentations distribute on the whole surface for a textured surface. The following section will study the case of a textured surface with indentations only on a portion region of the surface.

Fig. 4.11 shows the predicted contours of Mises stress by strain gradient theory for different numbers of indentation. All the contours are shown for the same tensile strain $\varepsilon = 0.223$. Fig. 4.11a and Fig. 4.11d correspond to the case shown in Fig. 4.5c. Fig. 4.11b and Fig. 4.11c show the deformed contour of textured sheets with indentation number equals to $N = 3$ and $N = 6$. The difference from the case of $N = 11$ is that, the

indentations in Fig. 4.11b and Fig. 4.11c only show up on the surface near to the symmetric plane. The interval of indentation is $a = 0.1L_0$ for all the cases in Fig. 4.11.

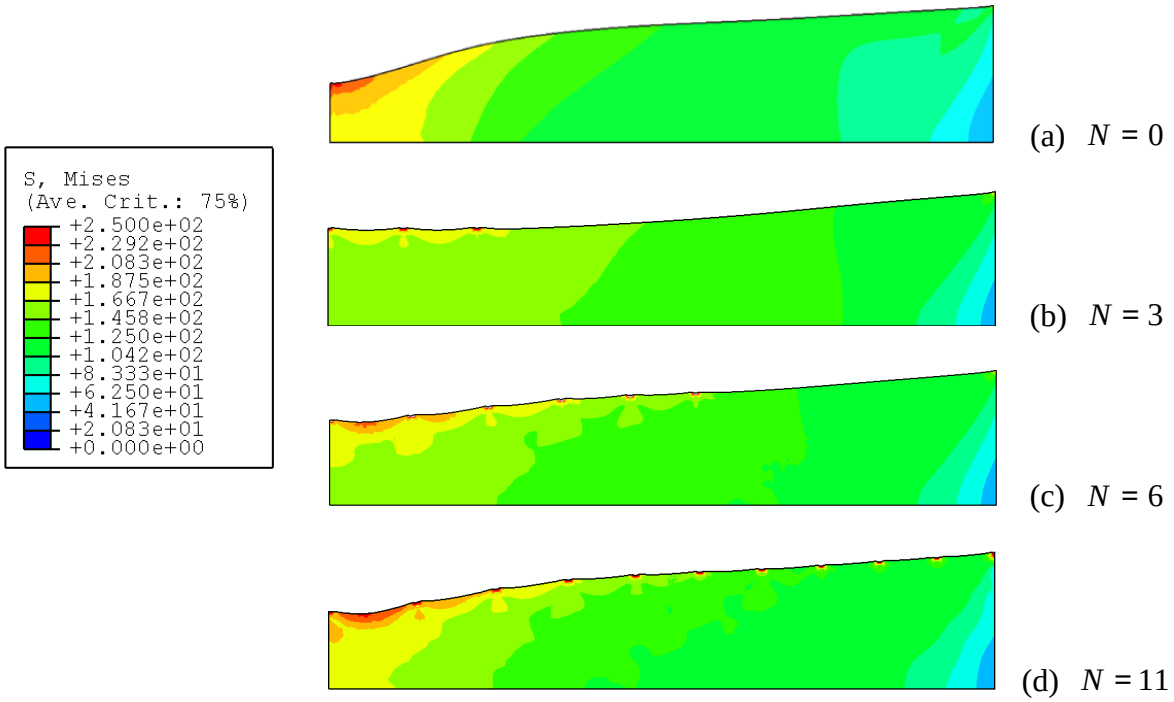

Figure 4.11: the predicted contours of Mises stress by strain gradient theory for different numbers of indentation. Intrinsic material length l_* / h_0 =0.4.

Fig. 4.12 shows the deformed profiles of smooth surface and textured surface. The blue line is for the textured surface with indentation number $N = 3$; for comparison, the results for $N = 0$ (smooth surface), and $N = 11$ are also shown in Fig. 4.12. In Fig. 4.12a, the blue line shows that necking firstly occurs at one position (pointed out by the blue arrow) which is far from the symmetric plane for the case of $N = 3$. This is typically different from red line and the black line, which have the onset of necking near the symmetric plane. As tensile strain increases, the neck for the blue line becomes more

significant at where it occurs as show in Fig. 4.12b. As the tensile strain continues to increase, an interesting thing happens: for the blue line, the neck disappears at the initial position, and then shows up at the region near to the symmetric plane as shown in Fig. 4.12c and Fig. 4.12d. In Fig. 4.12d, the positions for the minimum area of the neck are noted by the circle symbols.

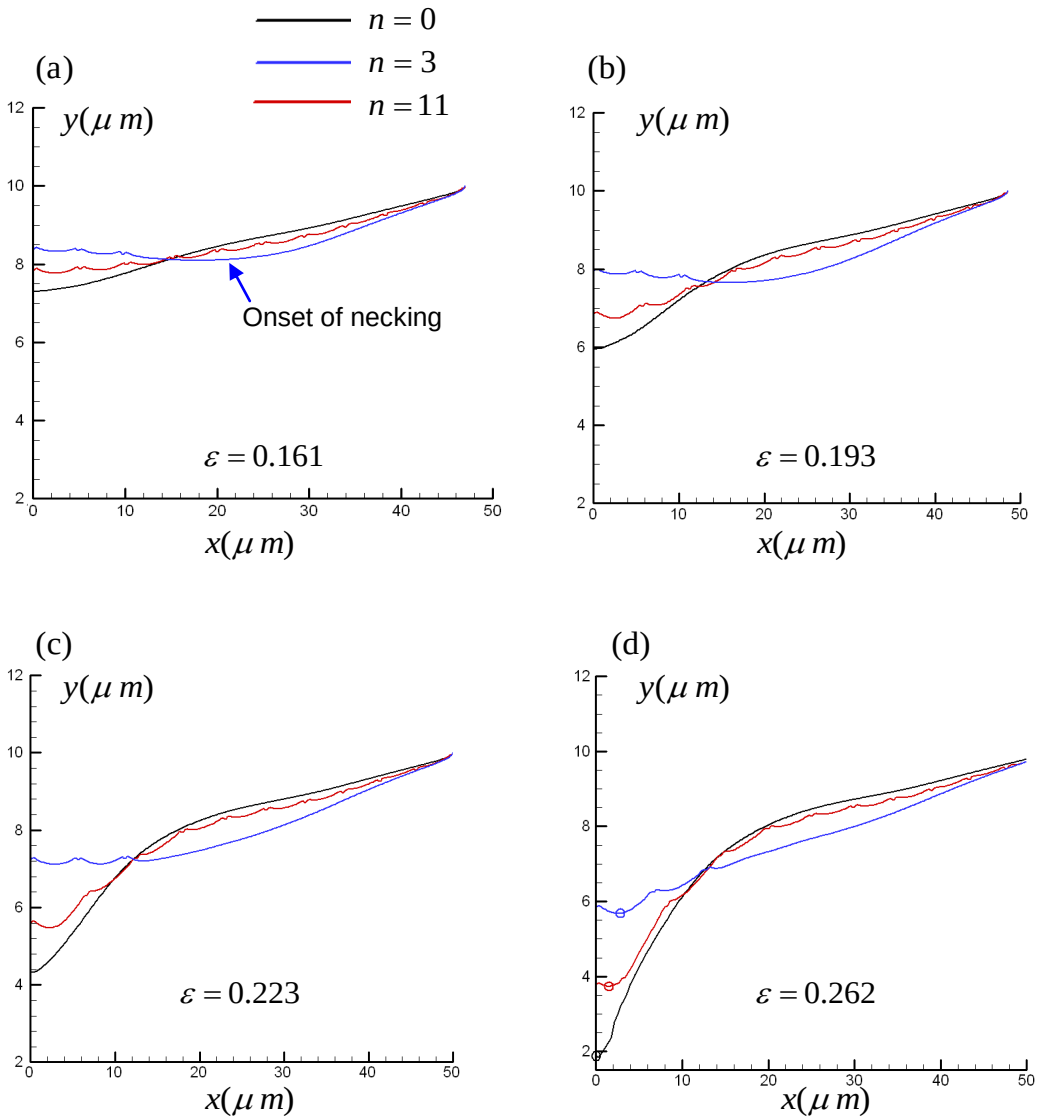

Figure 4.12: The deformed profiles of smooth surface and textured surface.

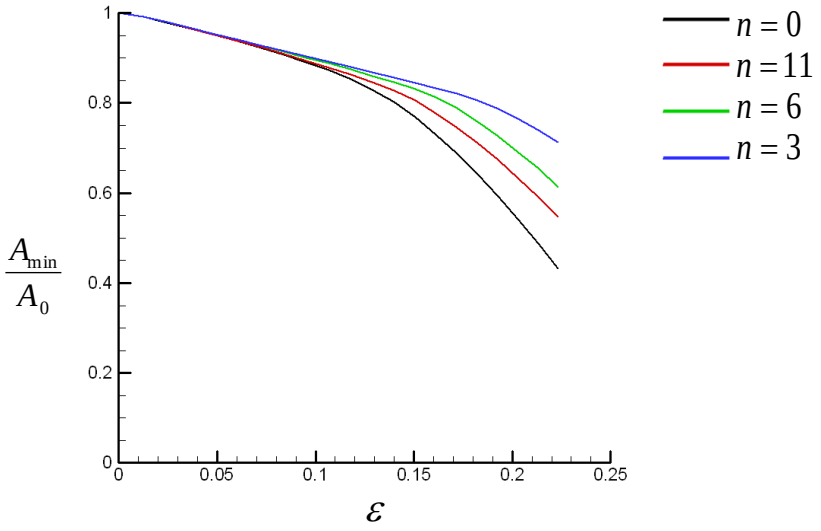

Figure 4.13: The normalized minimum area A_{min} / A_0 for different numbers of indentation. The material length l_* / h_0 =0.4.

Fig. 4.13 shows the normalized minimum area A_{min} / A_0 for different indentation number: N = 0 , 3, 6 and 11. It clearly shows that as indentation number decreases from N = 11 to N = 3 , the delay effect of necking increases significantly. The reason could be explained as follows: For the tensile deformation of the sheet with rigid grips, the necking occurs at the region near the symmetric plane due to the increased constraint at the end. The material at the neck region becomes softer compared to that at the end. So, we could say, the difference of the material stiffness between the neck region and the end causes the development of neck. Therefore, minimizing this difference could efficiently delay necking. That is why the textured surface with indentations only on the necking region has better effect on the delay.

Fig. 4.14 shows the normalized tensile force F/A_0 and the minimum area A_{min}/A_0 for different number of indentations. Fig. 4.14a shows that the curve for $N = 3$ reaches the maximum loading point at a larger strain compared to the curves for $N = 0$ and $N = 11$. Fig. 4.14b shows the onset of necking (the necking strains are $\varepsilon_n = 0.122$, 0.145 and 0.161 for $N = 0$, $N = 11$ and $N = 3$, respectively).

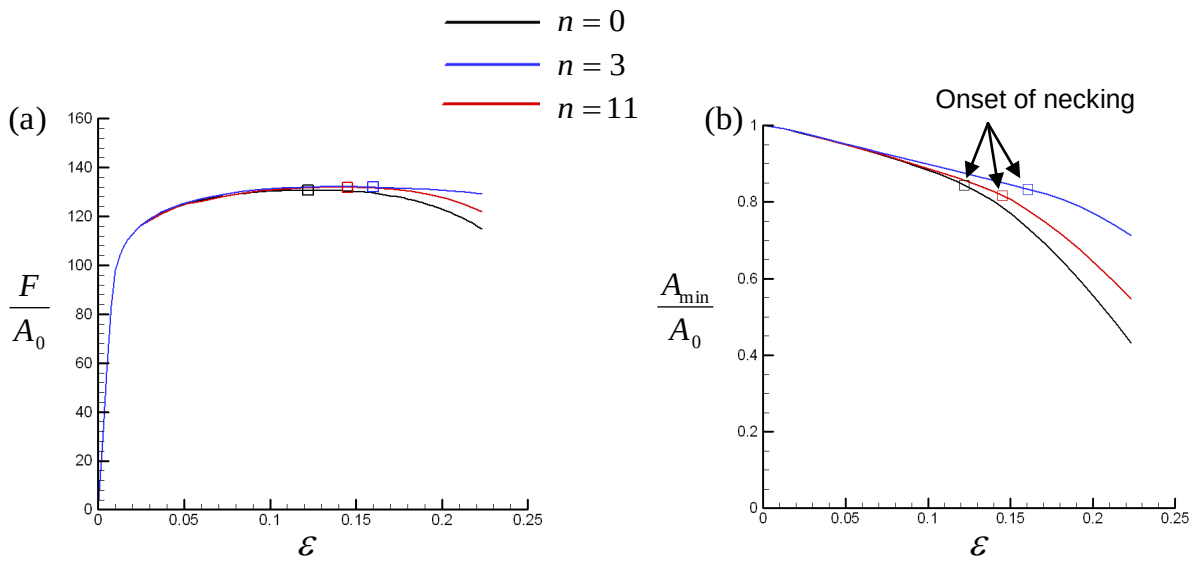

Fig. 4.14 The normalized tensile force F/A_0 and the minimum area A_{min}/A_0 for different numbers of indentation. The material length l_*/h_0=0.4.

Chapter 5: FE simulation of Zero cold reduction surface texturing

5.1 Surface texturing

One of the main objectives in the production process of sheet metal is the adjustment of the surface feature. The surface feature does not only influence the mechanical behavior in further process but also the optical appearance of the finished product, and therefore it has a deceive influence on the quality of the product. Therefore, Surface texturing gains more and more importance in the production process of sheet metal. Surface texturing is a metal finishing process to modify characteristic features on the sheet surface. During surface texturing, the applied deformation by work rolls is confined to the sheet surface only. There are two types of surface texturing. The first is called Zero Cold Reduction Surface Texturing (ZCRST); the second is Discrete Feature Embossing (DFE).

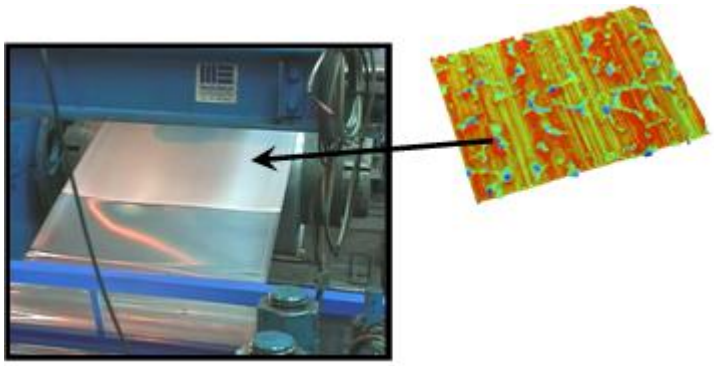

Figure 5.1: A metal finishing process: zero cold reduction surface texturing (ZCRST).

Zero Cold Reduction Surface Texturing or Tandem Surface Texturing (TST) is a method by which the topography of conventional mill-finish surfaces can be modified/replaced without the need for cold reduction (see e.g. Andersson et al., 2006; Ike et al., 2002). A possible tandem approach to surface texturing could be via a sequence of small diameter/textured work rolls (Fig. 5.2). The thickness and shape as well as the overall mechanical properties of a sheet must not be changed by TST. Applied deformation by work rolls should be confined to the sheet surface only. A necessary condition to do so is that applied forces never cause the through-thickness yield.

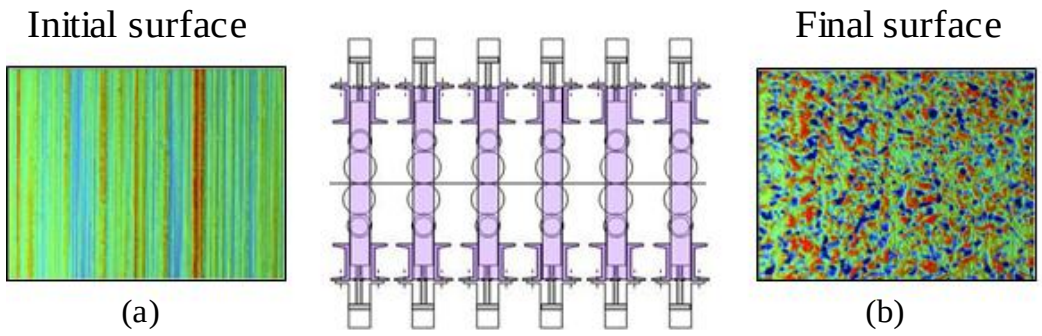

Figure 5.2: Typical six-stand tandem cold rolling mill.

Finite element method (FEM) has been widely used to simulate many kinds of rolling processes, such as slab rolling (Okado et al., 1981, Nikaido et al., 1984, Huisman, et al., 1985) and strip rolling (Jiang et al., 1998, 2000). Bunten et al. (1996) developed a FEM model to analyze the transfer behaviour of sheet surface by using the electron-beam texturing technique (EBT). The numerical results reveal some basic transfer mechanism (e.g. penetration processes and reverse extrusion phenomena) and applied a substitute profile model to explain the transfer behaviour. Huart et al. (2004) developed a model to predict the

local behaviour of surface asperities during cold rolling and found that the forward slip and reduction ratio has important influence on the plastic deformation of the asperity through pressure and shear force.

We have developed a finite element model, based on the classical Von Mises plasticity theory, to simulate TST. An initial surface topography was measured and implemented into the FEM as the starting free surface. The measured surface topography showed a significant band-type thickness distribution along the rolling direction (Fig. 23a). The deformed surface after TST was calculated and compared to the initial surface topography to evaluate the efficiency of the TST. From the preliminary numerical study, it seems that based on a detailed parametric study by using the FEM we could optimize the TST process and could reduce the number of stands needed to achieve "full" textural conversion. Except for the number of stands, the final feature of sheet surface (Fig. 23b) is mainly influenced by the two factors: (1) the surface feature of the work rolls; (2) contact conditions between the work rolls and sheet (e.g. friction contact or frictionless contact).

The purpose of this research is to find an optimized textured roller which results in lower surface roughness and lower directionality of surface profile. For comparison, the numerical results of deformed surfaces by smooth roller are presented as well.

5.2 Finite element model of rolling

Fig. 24 shows a 3D model of rolling on a sheet metal with rough surface. The roller is modeled as a smooth, rigid circle with the radius of 10mm as shown in Fig. 24a. Due to the symmetry, only half of the sheet is shown in our model, and half thickness of

the sheet is h =0.5mm. Fig. 24b shows the mesh and geometry of the sheet, and Fig. 24c shows the sheet surface, which is assumed to have a regular wavy profile. The colors in Fig. 24c represent different heights of the surface, and the amplitude of the wavy surface is 1 μm. Therefore, the height of rough surface is in the range from 0.499mm to 0.501mm. Contact between the roller and the wavy surface is modeled by the finite-sliding contact in ABAQUS/Explicit.

The material of the sheet is aluminum alloy. First, we consider the Von Mises plasticity theory for the surface deformation. The mechanical properties of aluminum are as follows: The Young's modulus $E = 73\,\text{GPa}$, Poisson's ratio $v = 0.33$, plastic work hardening exponent $n = 0.1$, and the initial yield stress is $\sigma_Y = 213\,\text{MPa}$.

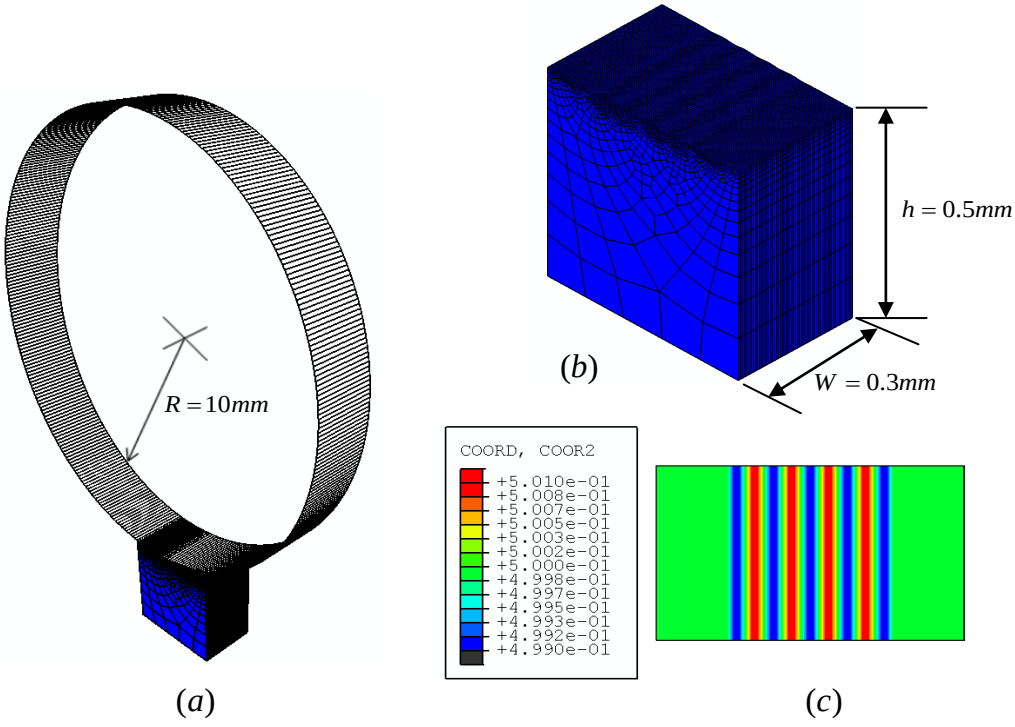

Figure 5.3: A model for rolling on wavy surface by a smooth roller.

5.3 Results and discussion

5.3.1 Rolling on a regular wawy surface

Fig. 5.4 shows the predicted contours of deformed surfaces for different rolling heights: h_c =10.5mm, 10.499mm and 10.498mm. The rolling height is defined as the distance from the roller center to the bottom of the sheet (see Fig. 5.4). When h_c equals to 10.5mm, it means that the bottom of roller is tangential with the mean line of the surface profile. The rolling direction is from left to right, so the coordinate x represents the rolling direction (RD), and z represents the tranverse direction (TD). We can see that, the height of the surface has been reduced after rolling, especially the peak value of the height. As h_c decreases, the average height of the deformed surface decreases. However, we can still see the band-type feature in all these figures.

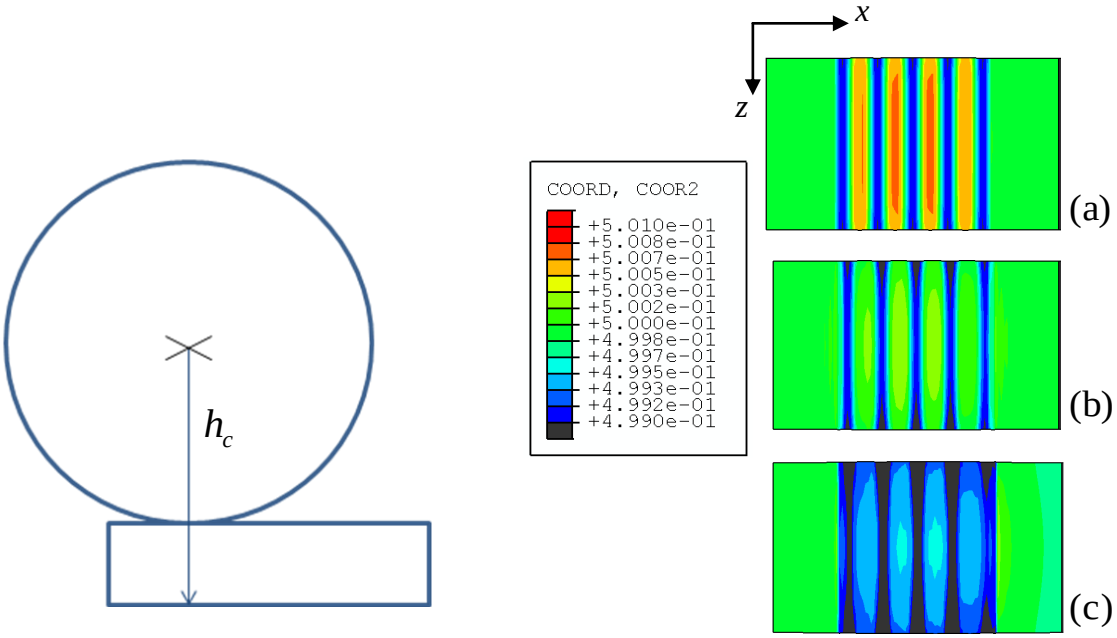

Figure 5.4: The predicted contours of deformed surfaces for rolling heights equal to (a) h_c =10.5mm, (b) 10.499mm, and (c) 10.498mm.

Fig. 5.5 shows the averaged thickness variation $\overline{h_z}$ over the width (Fig. 5.5a) and the predicted contact force F (Fig. 5.5b) for different rolling height. The definition of $\overline{h_z}$ is given by

$$\overline{h_z} = \frac{1}{N}\sum_{i=1}^{N} h_z(i)$$

which is the average height of sheet surface along the transverse direction (z direction). $\overline{h_z}$ is used to reflect the directionality of the surface profile.

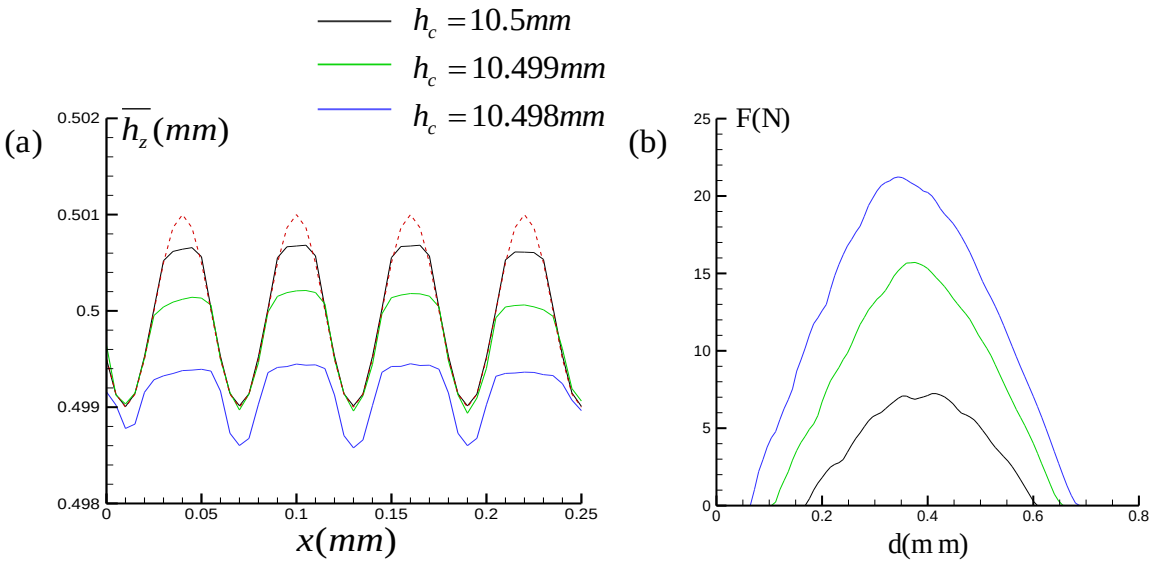

Figure 5.5: A plot of (a) the averaged thickness variation $\overline{h_z}$ over the width and (b) the predicted contact force F for different rolling height.

The $\overline{h_z}$ values of deformed profiles for different rolling height are shown in Fig. 5.5a. The horizontal coordinate x represents the length along the rolling direction. For comparison, the $\overline{h_z}$ value of initial surface is also presented by the red dashed line, which shows a regular wavy profile. The wave amplitude of the $\overline{h_z}$ profile reflects the degree of

the band-type feature. Fig. 5.5a shows that, the $\overline{h_z}$ values of deformed profiles still exhibit significant variation along the rolling direction. This means that the smooth roller can not destroy the band-type feature.

Fig.5.6 shows the predicted contours of equivalent plastic strain ε^p for different rolling height. It is seen that, as the rolling height h_c decreases, the plastic strain is not only confined in the surface region, but expends to the inner of the sheet. However, the deformed surfaces (Fig.5.4) still show the band-type feature. So, the smooth roller cannot destroy the band-type feature without causing large plastic yield region.

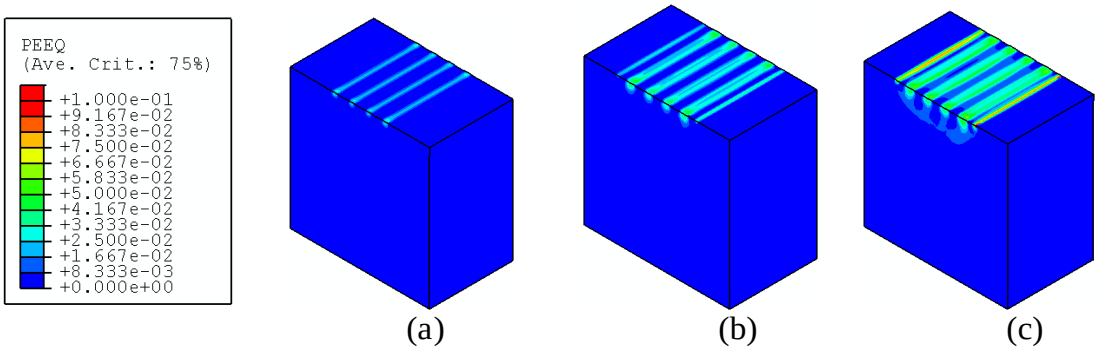

Figure 5.6: The predicted contours of equivalent plastic strain ε^p for different rolling height: (a) h_c =10.5mm, (b) 10.499mm, and (c) 10.498mm.

A possible method to destroy the band-type feature is using textured rollers as shown in Fig. 5.7. There are plateau features bonded on the surface of the roller. Two types of plateau shape are modeled: spherical plateau and conical plateau, which have the sizes on the order of micron.

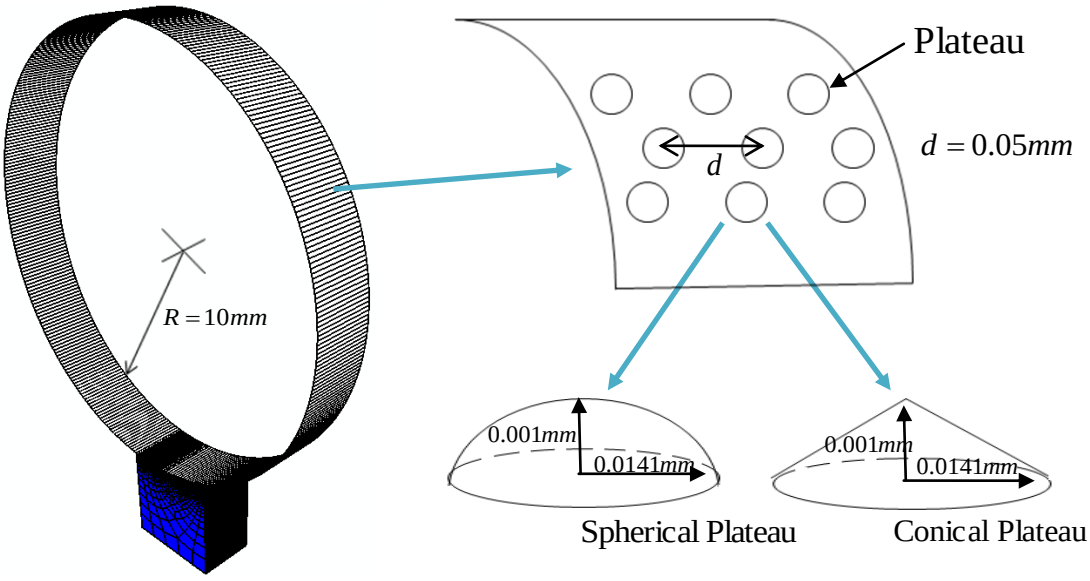

Figure 5.7: A model of rolling on a rough surface by a textured roller.

Fig. 5.8 shows the predicted contours of deformed surface by rolling with different type of roller. The rolling height is fixed at h_c =10.499mm for all the cases. The Figures in the left column show the case without considering friction, while the right column shows the case with friction (the frictional coefficient equals to μ =0.2). Fig. 5.8a shows the deformed surface for passing through a smooth roller, which still shows the band-type feature as shown before. Fig. 5.8b shows the deformed surface for passing through a textured roller with spherical plateaus. Usually, there is relative slip between the roller and the sheet surface according to the experiment. During the rolling process, the plateaus first contacted with the sheet surface, and then slide for a distance. Therefore the plateaus would leave a couple of scratches on the sheet surface (there are six plateaus along the width of the roll/sheet, so six scratches can be seen in Fig. 5.8b). The blue horizontal lines In Fig. 5.8b represent the scratches, which cross and destroy the band-

type feature along the rolling direction (RD). Fig. 5.8c shows the result for rolling by a textured roller with conical plateaus. We can also see the scratches on the deformed surface even though they are not as significant as those in Fig. 5.8b. It seems that the textured roller is efficient for destroying the initial band-type feature. However, the problem is, when considering friction, new band-type features show up along the transverse direction (TD) as clearly shown in Fig. 5.8b.

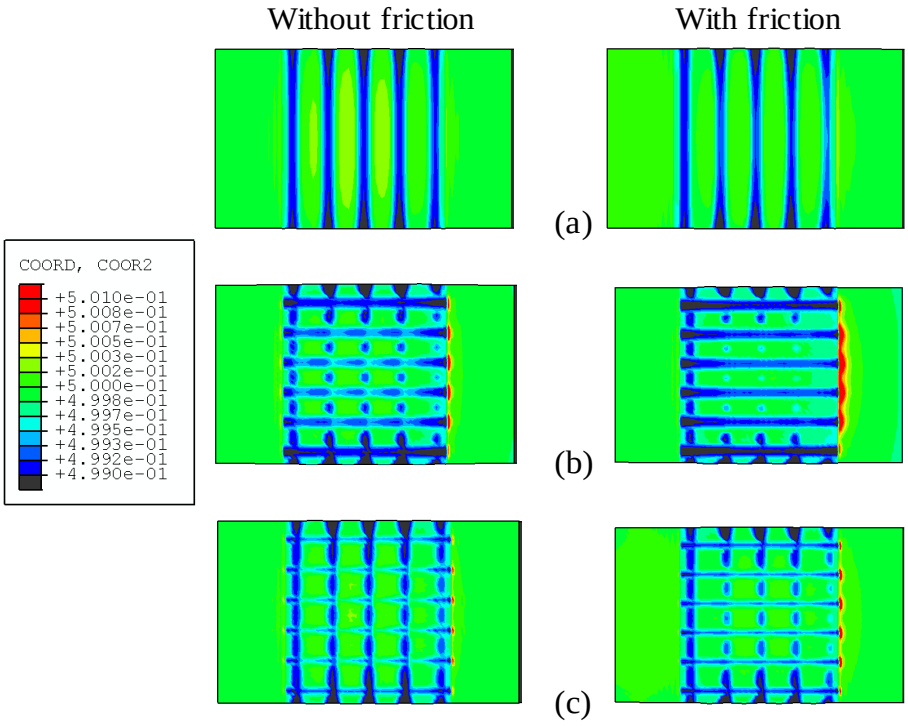

Figure 5.8: The predicted contours of deformed surface by rolling with different types of roller: (a) smooth roller, (b) textured roller with spherical plateaus and (c) textured roller with conical plateaus. The hight of the roller is h_c =10.499mm.

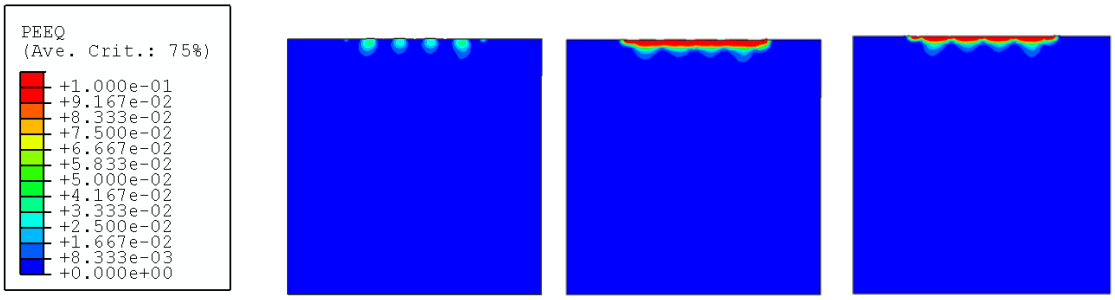

Figure 5.9: predicted contour of equivalent plastic strain ε^p for different type of roller. The hight of the roller is h_c =10.499mm.

Fig. 5.9 shows the predicted contours of equivalent plastic strain ε^p for different type of roller. Fig. 5.9b and Fig. 5.9c show that, for h_c equals to 10.499mm, the textured rollers with plateaus can produce larger plastic strain (marked by the red color) compared to the result for the smooth roller (Fig. 5.9a). However, the plastic region is still confined within the sheet surface.

Fig. 5.10 shows the predicted $\overline{h_z}$ values of deformed surface by using the different type of roller. Fig. 5.10a shows that compared to the result of smooth roller, the roller with plateaus can significantly reduce the wave amplitude of $\overline{h_z}$ profile for the rough surface with band-type feature. The roller with spherical plateau has a better effect than the roller with conical plateau on reducing the wave amplitude of the $\overline{h_z}$ profile. Fig. 5.10b shows the comparison of results with considering friction and without friction. It is seen that, friction has a positive effect on reducing the wave amplitude of $\overline{h_z}$. The reason can be explained as follows: During the sliding on the rough surface, the plateaus contact and then push the material on the peak forward to fill in the valley. When considering

friction, there is another portion of material to be taken from the peak to the valley by the frictional force, resulting in a better effect on eliminating the band-type feature.

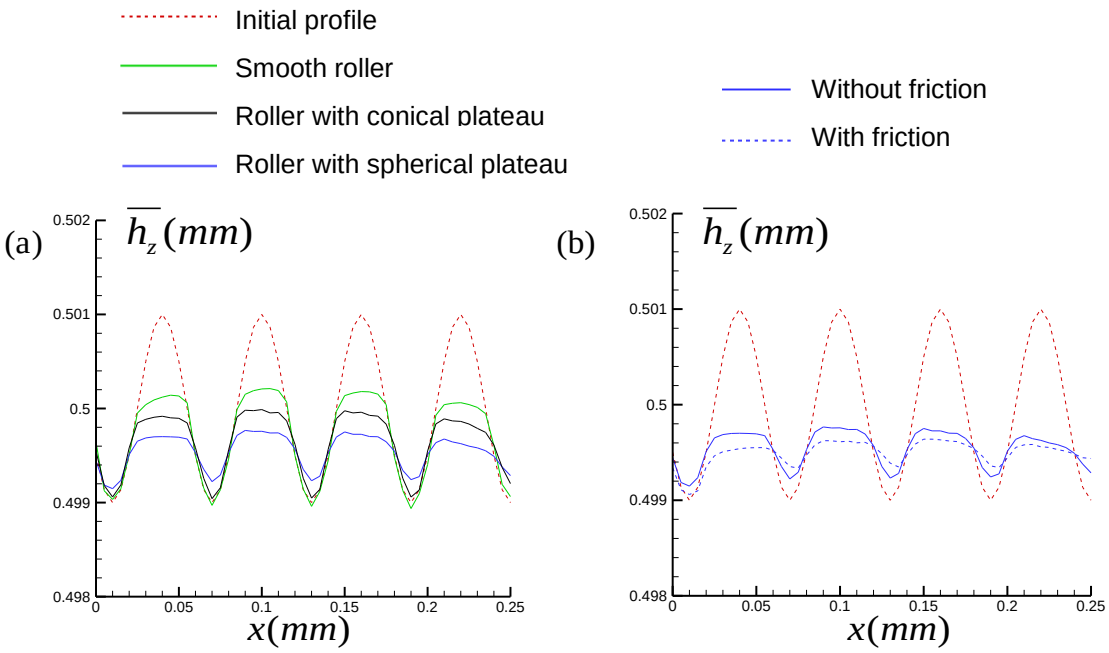

Figure 5.10: predicted the averaged thickness variation $\overline{h_z}$ over the width for different type of roller.

The average roughness $Ra = 0.637 \mu m$ for the initial surface profile, and is reduced to 0.405 μm for the smooth roller with the rolling height h_c =10.499mm. By using the textured roller with the same rolling height, Ra can be reduced to 0.324 μm and 0.330 μm for the roller with spherical plateau and conical plateau, respectively. Therefore, for such a regular wavy surface, the textured roller can greatly reduce the $\overline{h_z}$ value and the surface roughness.

In the above models for the textured roller, we assume that there are only six plateaus interacting with the rough surface. In the following, the number of the plateaus is increased to 12 and 24 to see how the results change for the deformed surfaces.

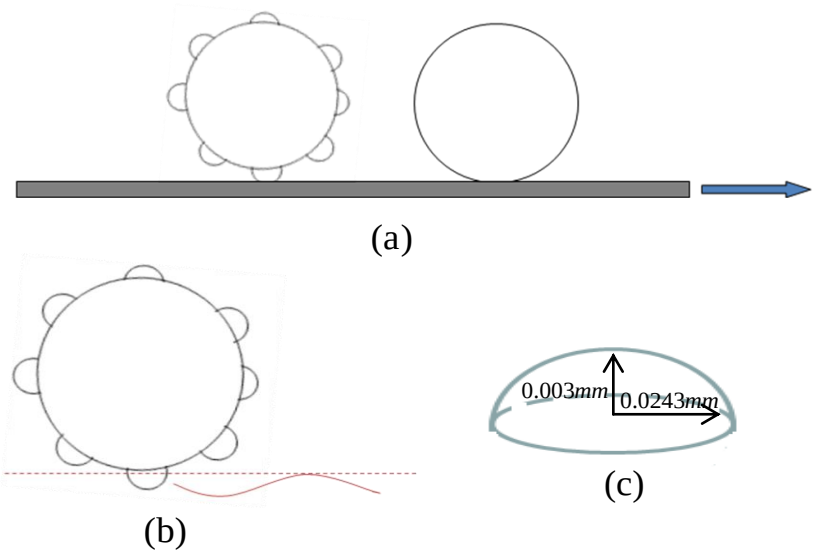

Figure 5.11: A rolling process using a textured roller and a smooth roller.

The rolling process for the roller with large number of plateaus is different from the previous one. Here, we use a rolling system including a textured roller and a smooth roller as shown in Fig. 5.11. First, the sheet passes through a textured roller with plateaus bonded on the roller surface. In this process, as shown in Fig. 5.11b, only the plateaus contact with the sheet, the roller surface does not. Otherwise large distortion would occur in our simulation results when the roller has a large number of plateaus. Second, we use a smooth roller to process the sheet surface in order to obtain a relative smooth appearance of the surface.

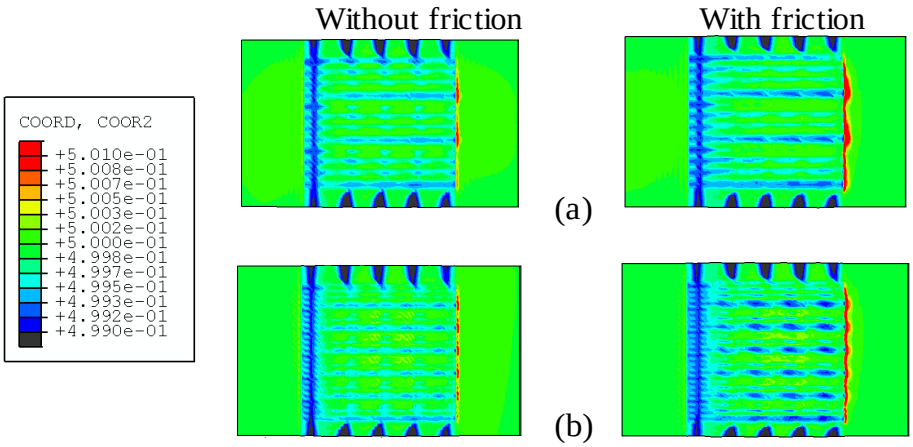

Figure 5.12: The predicted contours of deformed surface by textured rollers with spherical plateaus: (a) 12 plateaus and (b) 24 plateaus.

Fig. 5.12 shows the predicted contours of deformed surfaces by textured rollers with spherical plateaus. Fig. 5.12a shows the results for roller with 12 plateaus while Fig. 5.12b is for the roller with 24 plateaus. It is seen that, for the case without friction, the band-type features have been greatly destroyed along the rolling direction, and the deformed surfaces achieve a better appearance than the initial surface. For the case with friction, the scratches become more significant due to the frictional force and the deformed surfaces seem to be rougher compared to those without friction.

Fig. 5.13 shows the averaged thickness variation $\overline{h_z}$ (over the width) for textured rollers with spherical plateaus. Similar to the results shown before, Fig. 5.13a shows that the textured rollers can greatly reduce the wave amplitude of $\overline{h_z}$ curve. The curve of $\overline{h_z}$ for roller with 24 plateaus is close to that for 12 plateaus, which means that the effect of increasing plateau numbers on the deformed surface has a limitation. Fig. 5.13b shows that the comparison of the results with considering friction and without friction. The friction is benefit for reducing the wave amplitude of $\overline{h_z}$ value, which is the same as the

previous results. However, for the textured roller with 24 plateaus, the roughness Ra can be reduced to 0.267 μm without friction, while it is around 0.315 μm with considering friction. Therefore, the friction would increase the surface roughness.

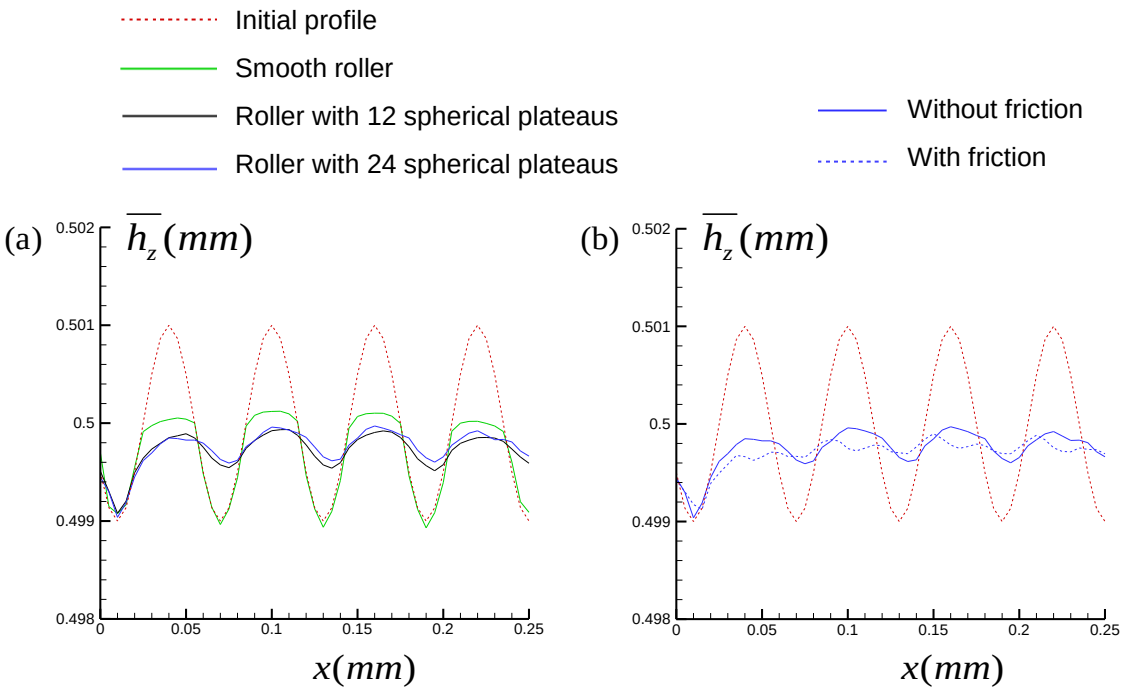

Figure 5.13: predicted the averaged thickness variation $\overline{h_z}$ over the width for textured rollers with sperical plateaus.

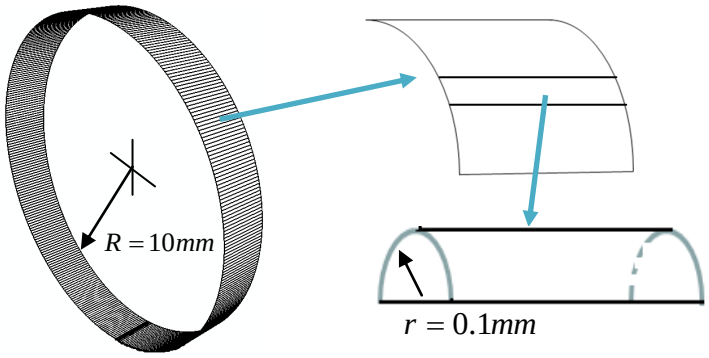

Figure 5.14: A model of textured roller with cylindrical plateau.

Also considered is the model of textured roller with cylindrical plateaus as shown in Fig. 5.14. The radius of the cylindrical plateaus is 0.1mm.

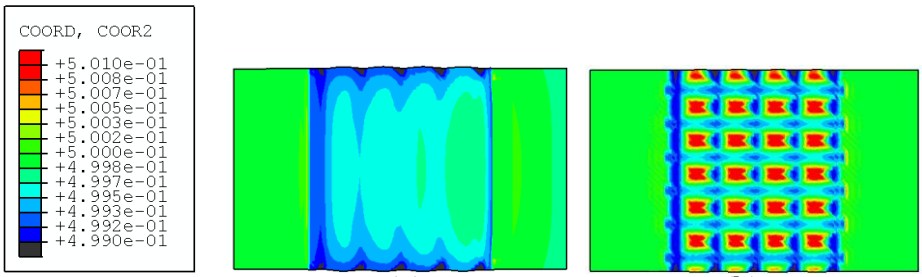

Figure 5.15: The predicted contours of deformed surfaces by textured rollers with (a) cylindrical plateaus and (b) spherical plateaus. Both case without frition and the rolling heigth h_c =10.599mm.

Fig. 5.15a shows the deformed surface for roller with the cylindrical plateaus. The rolling height is set as h_c =10.599mm, so that the bottom of the cylindrical plateaus is tangential with the valley of wavy surface and only the plateaus can contact with sheet surface. And we also assume that there is relative slip between the contacts. Fig. 5.15a shows that the band-type feature is greatly reduced by the cylindrical plateaus. It should point out that, Fig. 5.15a only shows the case without friction. When friction is considered, there is large shear force between the contacts, and the elements on the sheet surface would be greatly distorted. Therefore the simulation results with friction are not reliable and therefore are not shown here. For comparison, the deformed surface for the roller with spherical plateau is also shown in Fig. 5.15b. Also, only the spherical plateaus contact with the sheet surface, and the spherical plateaus reaches the same depth in the sheet surface as that for the cylindrical plateaus.

Fig. 5.16 shows the predicted contour of equivalent plastic strain ε^p for textured rollers with cylindrical plateaus and spherical plateaus. The region for large plastic strain (marked by red color) in both Fig. 5.16a and Fig. 5.16b are confined in the surface.

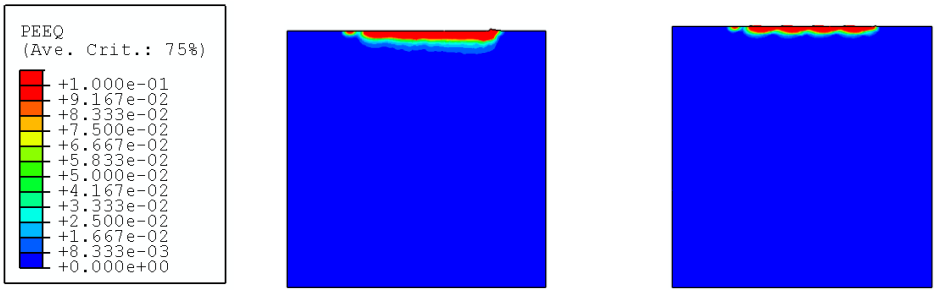

Figure 5.16: The predicted contour of equivalent plastic strain ε^p for textured rollers with (a) cylindrical plateaus and (b) spherical plateaus.

Fig. 5.17 shows the predicted contact force F and averaged thickness variation $\overline{h_z}$ for textured rollers with cylindrical plateaus and spherical plateaus.

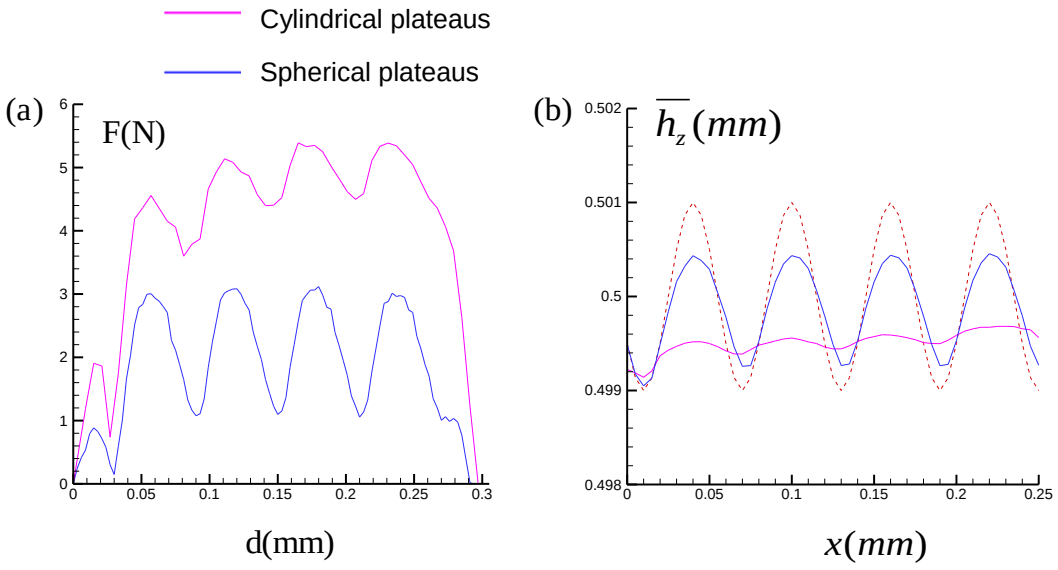

Figure 5.17: The predicted contact force F (a) and averaged thickness variation $\overline{h_z}$ (b) for textured rollers with cylindrical plateaus and spherical plateaus.

Fig. 5.17a shows that contact force for cylindrical plateaus is higher than that for spherical plateaus due to a larger contact area. Fig. 5.17b shows that the cylindrical plateaus can greatly reduce the wave amplitude of $\overline{h_z}$ curve and the surface roughness (The roughness of the deformed surface in Fig. 5.15a and Fig. 5.15b equal to 0.166 μm and 0.528 μm, respectively).

It seems that the cylindrical plateau is better for obtaining a much smoother surface. However, this is only the case without friction. If considering friction, as we have mentioned before, large distortion of the elements on the sheet surface would happen. Moreover, there is another drawback of using cylindrical plateau.

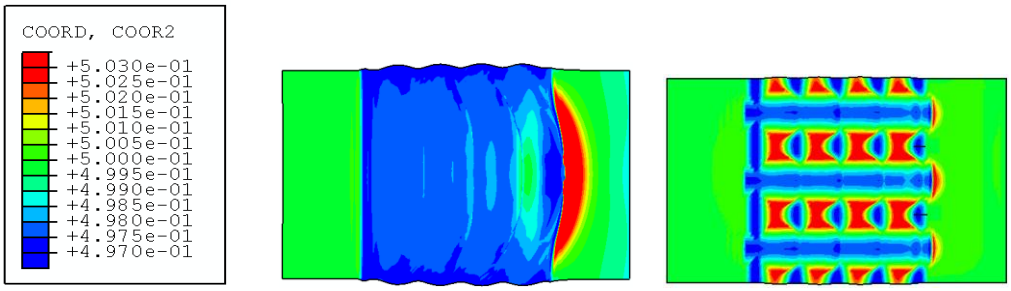

Fig. 5.18 The predicted contours of deformed surfaces by textured rollers with cylindrical plateaus (a) and spherical plateaus (b). The wave amplitude of the initial rough surface is $\delta_0 = 3\mu m$.

Fig. 5.18a shows the predicted contours of deformed surfaces by rollers with cylindrical plateaus for the initial rough surface with large wave amplitude $\delta_0 = 3\mu m$. It is seen that, the material on the sheet surface has been pushed forward and squeezed aside by the cylindrical plateau. Finally, a volume of material piles up in front of the plateau (as shown by the red color in Fig. 5.18a), which is like to deteriorate the surface

appearance. However, if we use the textured roller with spherical plateau, such phenomenon could be avoided as shown in Fig. 5.18b.

5.3.2 Rolling on real surface

The above results are all based on the simplified surface model, which has a regular wavy profile. In the following, we will study the rolling problem by using a real rough surface.

Fig. 5.19 shows the measured initial surface topography. The surface topography was measured experimentally and the data were imported into ABAQUS via the input File. The smallest size of the element is about $10\mu m$ in the sheet surface and the total element number is 78118. The material is aluminum alloy and the material properties are given in section 5.2.

Fig. 5.19a shows the 3D feature of the sheet surface, while Fig. 5.19b shows the 2D feature viewed from the top of the sheet. Fig. 5.19 shows that the surface indeed exhibits band-type feature along the rolling direction.

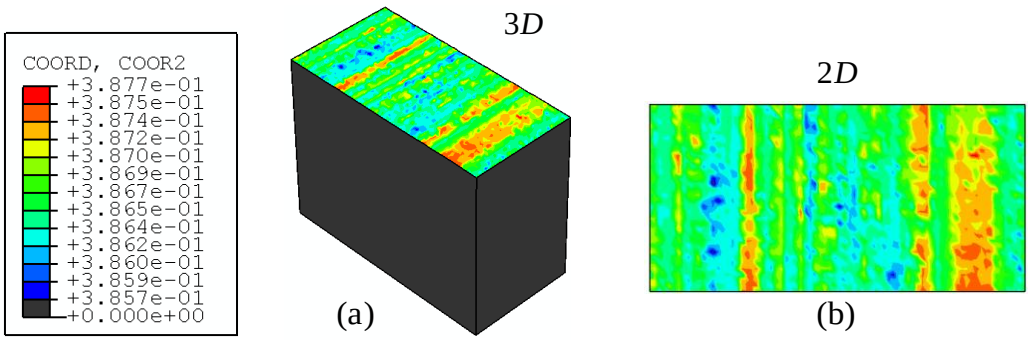

Figure 5.19: The measured initial surface topography

Fig. 5.20 shows the predicted contours of deformed surface by using smooth roller for rolling height (a) h_c =10.386mm and (b) h_c =10.385mm. We can still see the band-type feature in the deformed surfaces. The surface roughness Ra =0.211 μm and 0.113 μm for Fig. 5.20a and Fig. 5.20 b, respectively.

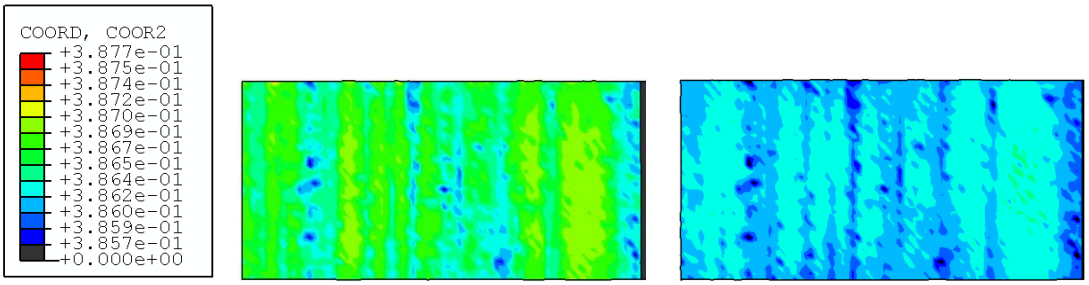

Figure 5.20: The predicted contours of deformed surface by using smooth roller for rolling height (a) h_c =10.386mm and (b) h_c =10.385mm.

Fig. 5.21 shows the predicted contours of deformed surface by using textured roller with spherical plateaus. The rolling height h_c =10.386mm, the same as that in Fig. 5.20a. The size of the spherical plateaus is shown in Fig.28. It is seen that, the deformed surface shows a random feature. The surface roughness Ra =0.260 μm for the deformed surface in Fig. 5.7.

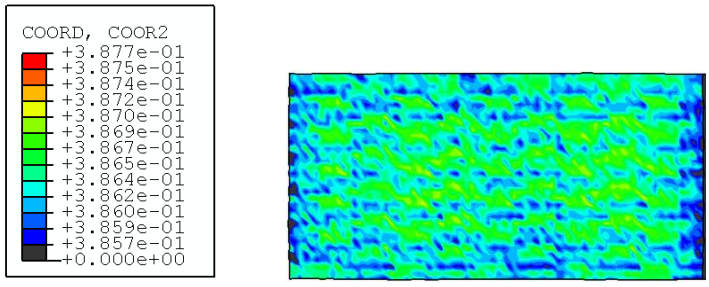

Figure 5.21: The predicted contours of deformed surface by using textured roller with spherical plateaus. The rolling height is h_c =10.386mm, and the size of spherical plateaus is shown in Figure 28.

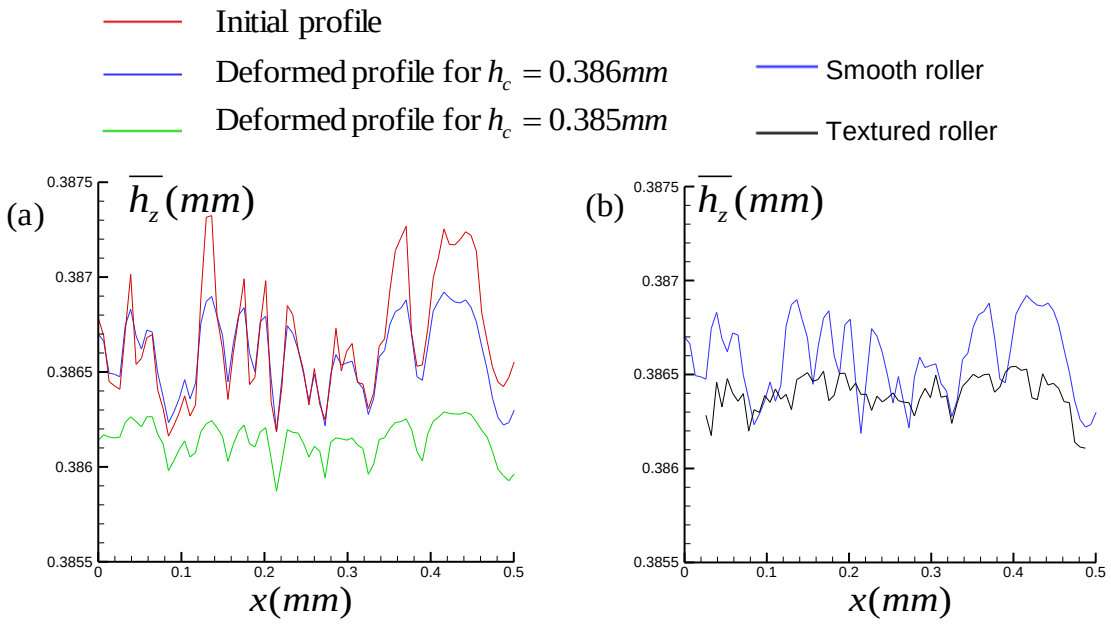

Figure 5.22: The predicted averaged thickness variation $\overline{h_z}$ for (a) smooth rollers and (b) textured roller.

Fig. 5.22a shows the predicted averaged thickness variation $\overline{h_z}$ for the smooth rollers with rolling height h_c =10.386mm and 10.385mm. The initial value of $\overline{h_z}$ is shown by the red line. Fig. 5.22b shows the value of $\overline{h_z}$ for textured roller with spherical plateaus. For comparison, the result for smooth roller at the same rolling height (h_c =10.386mm) is also shown in Fig. 5.22b. It is seen that, compared to the smooth roller, the textured roller can significantly reduce the wave amplitude of $\overline{h_z}$ value.

The results above are all based on the conventional plasticity theory. As mentioned before, the deformation of the sheet surface during rolling process is on the order of microns, so the size effect must be significant and should be taken into account. Here, we repeat the simulation of rolling with a smooth roller (the case shown in Fig.

5.4b) by using the strain gradient plasticity theory (CMSG). The material parameters for the UMAT of CMSG theory are the same as those used in the simulation of nano-indentation (the parameters can be found in section 3.2.1).

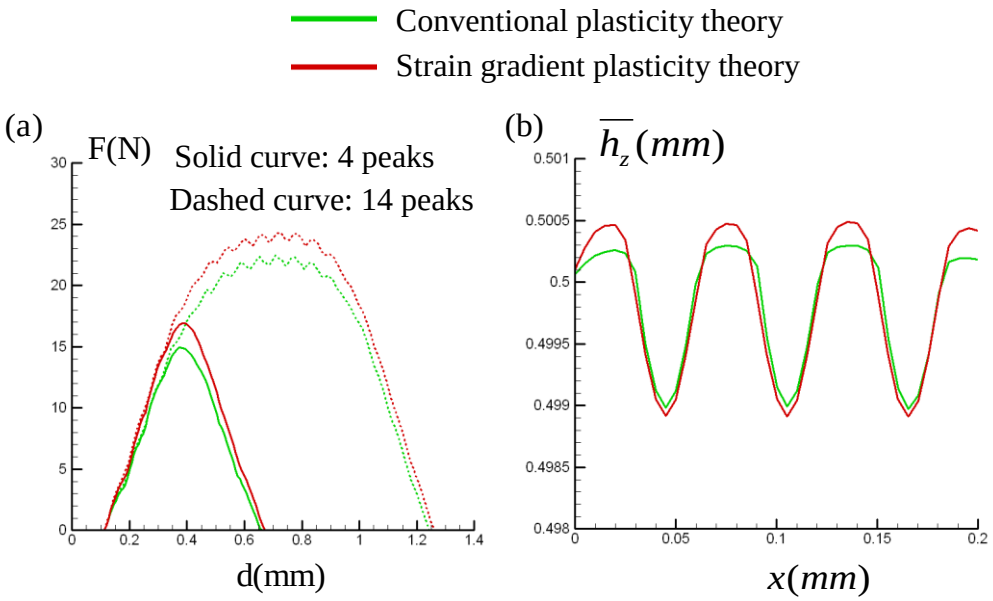

Figure 5.23: (a) the predicted contact force F and (b) the averaged thickness variation $\overline{h_z}$ by using the strain gradient plasticity theory.

Fig. 5.23a shows the predicted contact force F between the roller and the deformed surface. The green solid curve shows the force for the rough surface which has four peaks (as shown in Fig. 5.4) by using the conventional plasticity theory; while the red solid curve is for the case using strain gradient plasticity theory. It is seen that, the red curve is indeed higher than the green one. We extended the model of rough surface to include more peaks, and the results are shown in Fig. 5.23a by the dashed line. Also, the force is higher for the case with considering gradient effect. Fig. 5.23b shows the averaged thickness variation $\overline{h_z}$ for the deformed surface. It is clear that the peak value of $\overline{h_z}$ predicted by strain gradient plasticity is higher because the surface becomes harder

due to the gradient effect and therefore is not easy to be flattened by the roller. Even though the magnitude of the results predicted by strain gradient plasticity is larger than those predicted by conventional plasticity, there is no intrinsic difference for these two results. Therefore, we will not repeat all the simulation by using the strain gradient plasticity.

Chapter 6: Conclusions

(1) A computational model has been developed to study the nano-indentation on a rough surface, which has a simplified sine profile. The conventional theory of mechanism-based strain gradient plasticity is utilized in the model to predict the nano-indentation hardness. Different wavelength and amplitudes of the sine surface, as well as the indentation positions have been taken into account in the model. The numerical results show that, indentation hardness of a rough surface shows significant oscillation around the hardness of the smooth surface, and therefore it could either be higher or lower than the hardness of smooth surface. However, if considering the actual contact area, the hardness of a rough surface which is not completely flattened would be significant higher than the hardness of smooth surface.

(2) A FEM model has been developed to simulate the rolling process: Zero cold reduction surfaces texturing (ZCRST). The numerical results show that, the smooth roller can not destroy the band-type feature without causing a large plastic yield region; while, the textured roller with plateau features on the roller surface could significantly reduce the wave amplitude of the $\overline{h_z}$ curve, which reflects the directionality of the surface profile. Textured rollers with different shape of plateaus have been considered. It seems that, the spherical plateaus can be most efficient on destroying the band-type feature without causing large distortion of the elements on the surface, compared to the conical plateaus and the cylindrical plateaus. The effect of the plateaus number on the deformed surface has also been studied. Finally, we studied the surface texturing by using a measured initial surface topography. Similar to the results based on the simplified surface

model, the textured roller with spherical plateaus can produce a random rough surface with a significant elimination of the band-type feature.

(3) A FEM model has been developed to study the tensile deformation of the sheet with smooth surface and textured surfaces. The numerical results show that, the textured surface has no effect on the development of necking based on the conventional plasticity theory (the indentation depth is no more than 1% of the initial thickness of the sheet). However, by using the strain gradient theory, the textured surface could significantly delay necking due to the gradient hardening of the sheet surface via the indentation. The effect of the interval of the indenter, the tip radius, and the indentation depth on the delay has been considered in our model. Moreover, we found that, the indentation region has important influence on the delay. Compared to the textured surface with indentions on the whole surface, the textured surface with indentations only on a small region near the neck has a better effect on the delay.

Reference

Acharya, A. Bassani, J.L., 2000. Lattice incompatibility and a gradient theory of crystal plasticity. J. Mech. Phys. Solids 48, 1565-1595.

Andersson, P., Wild, M., Leven, J., Hemming, B., 2006. Transfer of surface texture from silicon nitride rolls to stainless steel wire in cold-rolling. Journal of Materials Processing Technology 173, 394–400.

Arsenlis, A., Parks, D.M., 1999. Crystallographic aspects of geometrically-necessary and statistically-stored dislocation density. Acta Mater. 47, 1597-1611.

Ashby, M.F., 1970. The deformation of plastically non-homogeneous alloys. Philos. Mag. 21, 399-424.

Aspinwall, D.K., Wise, M.L.H., Stout, K.J., Goh, T.H.A., Zhao, F.L., El-Menshawy, M.F., 1992. Electrical discharge texturing. Int. J. Mach. Tools Manuf. 32, 183-193.

Bardella, L., 2006. A deformation theory of strain gradient crystal plasticity that accounts for geometrically necessary dislocations. Journal of the Mechanics and Physics of Solids 54 (1), 128–160.

Bardella, L., 2007. Some remarks on the strain gradient crystal plasticity modelling, with particular reference to the material length scales involved. International Journal of Plasticity 23 (2), 296–322.

Bardella, L., Giacomini, A., 2008. Influence of material parameters and crystallography on the size effects describable by means of strain gradient plasticity. Journal of the Mechanics and Physics of Solids 56 (9), 2906–2934.

Barlat, F., 1987. Crystallographic texture, anisotropic yield surfaces and forming limits of sheet metals. Mater. Sci. Eng. 91, 55-72.

Bassani, J.L., 2001. Incompatibility and a simple gradient theory of plasticity. Journal of the Mechanics and Physics of Solids 49 (9), 1983 – 1996.

Bobji, M.S., Biswas, S.K., 1999. Deconvolution of hardness from data obtained from nanoindentation of rough surfaces. Journal of Materials Research 14, 2259-2268.

Bobji, M.S., Biswas, S.K., 1999. Estimation of hardness by nanoindentation of rough surfaces. Journal of Materials Research 13, 3227-3233.

Brinckmann, S., Siegmund, T., Huang, Y., 2006. A dislocation density based strain gradient model. International Journal of Plasticity 22, 1784–1797.

Brunig, M., 1998. Numerical analysis and modeling of large deformation and necking behavior of tensile specimens. Finite Elements in Analysis and Design 28, 303-319.

Brunet, M., Mguil, S., Morestin, F., 1998. Analytical and experimental studies of necking in sheet metal forming processes. J. Mater. Process. Technol. 80-81, 40-46.

Brunet, M., Morestin, F., 2001. Experimental and analytical necking studies of anisotropic sheet metals. J. Mater. Process. Technol. 112, 214-226.

Bunten, R., Steinhoff, K., Rasp, W., Kopp, R., Pawelski, O., 1996. Development of a FEM-model for the simulation of the transfer of surface structure in cold-rolling processes. J. Mater. Process. Technol. 60, 369-376.

Cabezas, E.E., Celentano, D.J., 2004. Experimental and numerical analysis of the tensile test using sheet specimens. Finite Elements in Analysis and Design 40, 555-575.

Cermelli, P., Gurtin, M.E., 2002. Geometrically necessary dislocations in viscoplastic single crystals and bicrystals undergoing small deformations. International Journal of Solids and Structures 39 (26), 6281–6309, PII: S0020-7683(02)00491-2.

Chen, S.H., Wang, T.C., 2000. A newhardening law for strain gradient plasticity. Acta Materialia 48 (16), 3997 – 4005.

Chen, S.H., Wang, T.C., 2002. A newdeformation theory with strain gradient effects. International Journal of Plasticity 18 (8), 971 – 995.

Cleveringa, H.H.M., VanderGiessen, E., Needleman, A., 1997. Comparison of discrete dislocation and continuum plasticity predictions for a composite material. Acta Materialia 45 (8), 3163 – 3179.

Cleveringa, H.H.M., VanderGiessen, E., Needleman, A., 1998. Discrete dislocation simulations and size dependent hardening in single slip. Journal de Physique IV 8 (P4), 83 – 92.

Cleveringa, H.H.M., VanderGiessen, E., Needleman, A., 1999a. A discrete dislocation analysis of bending. International Journal of Plasticity 15 (8), 837 – 868.

Cleveringa, H.H.M., VanderGiessen, E., Needleman, A., 1999b. A discrete dislocation analysis of residual stresses in a composite material. Philosophical Magazine A 79 (4), 893 – 920.

Cottrell, A.H., 1964. The mechanical Properties of Materials. J. Wiley, NewYork. p. 277.

Douglass, M.R., 1998. Lifetime estimates and unique failure mechanisms of the digital micromirror device (DMD). In: Annual Proceedings ‐ Reliability Physics Symposium (Sponsored by IEEE), 31 March ‐ 2 April 1998, pp. 9 ‐ 16.

Durst, K., Backes, B., Goken, M., 2005. Indentation size effect in metallic materials: correcting for the size of the plastic zone. Scr. Mater. 52, 1093-1097.

Etsion, I., Halperin, G., Brizmer, V., Kligerman, Y., 2004. Experimental investigation of laser surface textured parallel thrust bearings. Tribology Letter 17, 295-300.

Feng, G., Nix W, D., 2004. Indentation size effect in MgO. Scr. Mater. 51, 599-603.

Fjeldly, A., Søreng, A., Roven, H.J., 2001. Strain localisation in solution heat treated Al–Zn–Mg alloys. Mater. Sci. Eng. A 300, 165-170.

Fleck, N.A., Hutchinson, J.W., 1993. A phenomenological theory for strain gradient effects in plasticity. Journal of the Mechanics and Physics of Solids 41 (12), 1825 ‐ 1857.

Fleck, N.A., Hutchinson, J.W., 1997. Strain gradient plasticity. In: Hutchinson, J.W., Wu, T.Y. (Eds.), Advances in Applied Mechanics, Vol. 33. Academic Press, NewYork, pp. 295 ‐ 361.

Fleck, N.A., Hutchinson, J.W., 2001. A reformulation of strain gradient plasticity. Journal of the Mechanics and Physics of Solids 49 (10), 2245 ‐ 2271.

Fleck, N.A., Muller, G.M., Ashby, M.F., Hutchinson, J.W., 1994. Strain gradient plasticity: theory and experiments. Acta Metallurgica et Materialia 42 (2), 475 ‐ 487.

Fleck, N.A., Willis, J.R., 2009a. A mathematical basis for strain-gradient plasticity theory – Part I: Scalar plastic multiplier. Journal of the Mechanics and Physics of Solids 57 (1), 161–177.

Fleck, N.A., Willis, J.R., 2009b. A mathematical basis for strain-gradient plasticity theory. Part II: Tensorial plastic multiplier. Journal of the Mechanics and Physics of Solids 57 (7), 1045–1057.

Gao, H., Huang, Y., Nix, W.D., Hutchinson, J.W., 1999. Mechanismbased strain gradient plasticity–I. Theory. J. Mech. Phys. Solids 47, 1239-1263.

Geiger, M., Popp, U., Engel, U., 2002. Excimer laser micro texturing of cold forging tool surfaces-Influence on tool life. CIRP Annals: Manufacturing Technology 51, 231–234.

Graf, A., Hosford, W.F., 1990. Calculations of forming limit diagrams. Metall. Trans. 21A, 87-94.

Gurtin, M.E., 2000. On the plasticity of single crystals: free energy, microforces, plastic-strain gradient. Journal of the Mechanics and Physics of Solids 48 (5), 989 – 1036.

Gurtin, M.E., 2002. A gradient theory of single-crystal viscoplasticity that accounts for geometrically necessary dislocations. Journal of the Mechanics and Physics of Solids 50 (1), 5 – 32.

Gurtin, M.E., 2003. On a framework for small-deformation viscoplasticity: free energy, microforces, strain gradients. International Journal of Plasticity 19 (1), 47–90, PII: S0749-6419(01)00018-3.

Gurtin, M.E., 2004. A gradient theory of small-deformation isotropic plasticity that accounts for the Burgers vector and for dissipation due to plastic spin. J. Mech. Phys. Solids 52, 2545–2568.

Gurtin, M.E., Anand, L., 2007. A gradient theory for single-crystal plasticity. Modelling and Simulation in Materials Science and Engineering 15 (1), S263–S270.

Hansen, N.R., Schreyer, H.L., 1994. A thermodynamically consistent framework for theories of elastoplasticity coupled with damage. International Journal of Solids and Structures 31 (3), 359–389.

Haque, M.A., Saif, M.T.A. Strain gradient effect in nanoscale thin films. Acta Materialia, S1 (11), 3053 – 3061.

Holmberg, S., Enquist, B., Thilderkvist, P., 2004. Evaluation of sheet metal formability. Journal of Materials Processing Technology 145, 72-83.

Huang, Y., Gao, H., Nix, W.D., Hutchinson, J.W., 2000a. Mechanism-based strain gradient plasticity—II. Analysis. Journal of the Mechanics and Physics of Solids 48 (1), 99 – 128.

Huang, Y., Xue, Z., Gao, H., Nix, W.D., Xia, Z.C., 2000b. A study of microindentation hardness tests by mechanism-based strain gradient plasticity. Journal of Materials Research 15 (8), 1786 – 1796.

Huang, Y., Qu, S., Hwang, K.C., Li, M., Gao, H., 2004. A conventional theory of mechanism-based strain gradient plasticity. Int. J. Plast. 20, 753-782.

Huang, Y., Zhang, F., Hwang, K.C., Nix, W.D., Pharr, G.M., Feng, G., 2006. A model of size effects in nano-indentation. Journal of the Mechanics and Physics of Solids 54, 1668-1686.

Huart, S., Dubar, M., Deltombe, R., Dubois, A. Dubar, L., 2004. Asperity deformation, lubricant trapping and iron fines formation mechanism in cold rolling processes. Wear 257, 471-480.

Hwang, K.C., Jiang, H., Huang, Y., Gao, H., Hu, N., 2002. A finite deformation theory of strain gradient plasticity. Journal of the Mechanics and Physics of Solids 50 (1), 81 – 99.

Hwang, K.C., Jiang, H., Huang, Y., Gao, H., 2003a. Finite deformation analysis of mechanism-based strain gradient plasticity: torsion and crack tip field. International Journal of Plasticity 19 (2), 235 – 251.

Hwang, K.C., Yun, G., Huang, Y., 2003b. A reformulation of mechanism-based strain gradient (MSG) plasticity.

Ike, H., Tsuji, K., Takase, M., 2002. In situ observation of a rolling interface and modeling of the surface texturing of rolled sheets. Wear 252, 48-62.

Inal, K., Wu, P.D., Neale, K.W., 2002. Finite element analysis of localization in FCC polycrystalline sheets under plane stress tension. International Journal of Solids and Structures 39, 3469-3486.

Kajberg, J., Lindkvist, G., 2004. Characterisation of materials subjected to large strains by inverse modeling based on in-plane displacement fields. International Journal of Solids and Structures 41, 3439-3459.

Kang, K., Pelow, C., Witham, L., 2008. Analysis of changes in 3D surface texture anisotropy ratio parameter and friction during sheet rolling campaigns. Wear 264, 434-438.

Kim J., Kang, S., Lee, J., Jang, J., Lee, Y.H., Kwon D., 2007. Influence of surface-roughness on indentation size effect. Acta materialia 55, 3555-3562.

Kijima, H., Bay, N., 2008a. Skin-pass rolling I—studies on roughness transfer and elongation under pure normal loading, International Journal of Machine Tools and Manufacture 48, 1313-1317.

Kijima, H., Bay, N., 2008b. Skin-pass rolling II—studies on roughness transfer under combined normal and tangential loading. International Journal of Machine Tools and Manufacture 48, 1308-1312.

Koc, P., Stok, B., 2004. Computer-aided identification of the yield curve of a sheet metal after onset of necking. Computational Materials Science 31, 155-168.

Komori, K., 2002. Simulation of tensile test by node separation method. Journal of Materials Processing Technology 125–126, 608-612.

Kovalchenko, A., Ajayi, O., Erdemir, A., Fenske, G., Etsion, I., 2005. The effect of laser surface texturing on transitions in lubrication regimes during unidirectional sliding contact. Tribology International 38, 219-225.

Kuroda, M., Tvergaard, V., 2000. Forming limit diagrams for anisotropic metal sheets with different yield criteria. Int. J. Solids Struct. 37, 5037-5059.

Kumar, C.P., Menezes, P.L., Kailas, S.V., 2008. Role of surface texture on friction under boundary lubricated conditions. Tribology Online 3, 12-18.

Lademo, O.-G., Pedersen, K.O., Berstad, T., Furu, T., Hopperstad, O.S., 2008. An experimental and numerical study on the formability of textured AlZnMg alloys. European Journal of Mechanics A/Solids 27, 116-140.

Lemaitre, J., 1985. Coupled elasto-plasticity and damage constitutive-equations. Computer Methods in Applied Mechanics and Engineering 51 (1–3), 31–49.

Liewald, M., Wagner, S., Becker, D., 2010. Influence of surface topography on the tribological behaviour of aluminium alloy 5182 with EDT surface. Tribology Letter 39, 135-142.

Lim, Y.Y., Chaudhri, M.M., 1999. The effect of the indenter load on the nanohardness of ductile metals: an experimental study on polycrystalline work-hardened and annealed oxygen-free copper. Philos. Mag. A-Phys. Condens. Matter Struct. Defects Mech. Properties 79, 2979-3000.

Lloyd, D.J., 1994. Particle reinforced aluminum and magnesium matrix composites. International Materials Reviews 39, 1 – 23.

Ma , Q., Clarke, D.R., 1995. Size dependent hardness of silver single crystals. J. Mater. Res. 10, 853-863.

Ma, B., Tieu, A.K., Lu, C., Jiang, Z., 2002. An experimental investigation of steel surface characteristic transfer by cold rolling. Journal of Materials Processing Technology 125–126, 657-663.

Man, C.-S., Gao, X., Godefroy, S., Kenik, E.A., 2010. Estimating geometric dislocation densities in polycrystalline materials from orientation imaging microscopy. International Journal of Plasticity 26 (3), 423–440.

Marciniak, Z., Kuczynski, K., 1967. Limit strains in the processes of stretch-forming sheet metal. Int. J. Mech. Sci. 9, 609-620.

McElhaney, K.W., Vlasssak, J.J., Nix, W.D., 1998. Determination of indenter tip geometry and indentation contact area for depthsensing indentation experiments. J. Mater. Res. 13, 1300-1306.

McGinty, R.D., McDowell, D.L., 2004. Application of multiscale crystal plasticity models to forming limit diagrams. J. Eng. Mater. Technol. 126, 285-291.

Merklein, M., Lechler, J., Geigner, M., 2006. Characterisation of the flow properties of the quenchenable ultra high strength steel 22MnB5. Annals of the CIRP 1, 229-232.

Miller, W.S., Zhuang, L., Bottema, J., Wittebrood, A., De Smet, P., Haszler, A., Vieregge, A., 2000. Recent development in aluminium alloys for the automotive industry. Materials Science and Engineering A 280, 37-49.

Mindlin, R.D., 1964. Micro-structure in linear elasticity. Archive Rational Mechanics Analysis 16, 51 – 78.

Mindlin, R.D., 1965. Second gradient of strain and surface tension in linear elasticity. International Journal of Solids and Structures 1, 417 – 438.

Naderi, M., Amiri, M., Khonsari, M.M., 2010. On the thermodynamic entropy of fatigue fracture. Proceedings of the Royal Society A – Mathematical Physical and Engineering Sciences 466 (2114), 423–438.

Needleman, A., 1972. A numerical study in circular cylindrical bars. J. Mech. Phys. Solids 20, 111-127.

Niordson, C.F., Redanz, P., 2004. Size-effects in plane strain sheet-necking. Journal of the Mechanics and Physics of Solids 52, 2431-2454.

Nix, W.D., 1989. Mechanical properties of thin films. Mater. Trans. 20A, 2217-2245.

Nix, W.D., 1997. Elastic and plastic properties of thin films on substrates: nanoindentation techniques. Materials Science and Engineering A 234, 37 – 44.

Nix, W.D., Gao, H., 1998. Indentation size effects in crystalline materials: a law for strain gradient plasticity. J. Mech. Phys. Solids 46, 411-425.

Nye, J.F., 1953. Some geometrical relations in dislocated crystals. Acta Metall. Mater. 1,

Okazawa, S., 2010. Structural bifurcation for ductile necking localization. International Journal of Non-Linear Mechanics 45, 35-41.

Poole, W.J., Ashby, M.F., Fleck, N.A., 1996. Micro-hardness of annealed and work-hardened copper polycrystals. Scripta Mater. 34, 559-564.

Qu, S., Huang, Y., Nix, W.D., Jiang, H., Zhang, F., Hwang, K.C., 2004. Indenter tip radius effect on the Nix-Gao relation in micro- and nanoindentation hardness experiments. J. Mater. Res. 19, 3423-3434.

Rajagopal, K.R., Srinivasa, A.R., 2004a. On the thermomechanics of materials that have multiple natural configurations – Part I: viscoelasticity and classical plasticity. Zeitschrift Fur Angewandte Mathematik Und Physik 55 (5), 861–893.

Rajagopal, K.R., Srinivasa, A.R., 2004b. On the thermomechanics of materials that have multiple natural configurations – Part II: twinning and solid to solid phase transformation. Zeitschrift Fur Angewandte Mathematik Und Physik 55 (6), 1074–1093.

Safikhani, A.R., Hashemi, R., Assempour, A., 2009. Some numerical aspects of necking solution in prediction of sheet metal forming limits by strain gradient plasticity. Materials and Design 30, 727-740.

Simão, J., Aspinwall, D.K., Wise, M.L.H., El-Menshawy, M.F., 1994. Mill roll texturing using EDT. J. Mater. Process. Technol. 45, 207-214.

Simão, J., Aspinwall, D.K., Wise, M.L.H., Subari., K., 1996. Surface texture transfer in simulated tandem and temper mill rolling using electrical discharge textured rolls. J. Mater. Process. Technol. 56, 177-189.

Stelmashenko, N.A., Walls, A.G., Brown, L.M., Milman, Y.V., 1993. Microindentation on W and Mo oriented single crystals: An STM study. Acta Metall. Mater. 41, 2855-2865.

Stolken, J.S., Evans, A.G., 1998. A microbend test method for measuring the plasticity length scale. Acta Materialia 46 (14), 5109 – 5115.

Suresh, S., Nieh, T.G., Choi, B.W., 1999. Nano-indentation of copper thin films on

Swadener, J.G., George, E.P., Pharr, G.M., 2002. The correlation of the indentation size effect measured with indenters of various shapes. Journal of the Mechanics and Physics of Solids 50 (4), 681-694.

Tang, C.Y., Fan, J.P., Lee, T.C., 2003. Simulation of necking using a damage coupled finite element method. Journal of Materials Processing Technology 139, 510-513.

Tao, H., Zhang, N., Tong, W., 2009. An iterative procedure for determining effective stress–strain curves of sheet metals. International Journal of Mechanics and Materials in Design 5, 13-27.

Tobiyama, Y., Abotani, K., 2004. Hot-Dip Galvanized Steel Sheet with Excellent Surface Quality for Automotive Outer Panels, JFE Technical Report 4, 55-60.

Tvergaard, V., Needleman, A., 1984. Analysis of the cup-cone fracture in a round tensile bar. Acta Metall. 32, 157-169.

Vermeulen, M., Scheers, J., De Mare, C., De Coomanocas, B., 1995. 3D-characterisation of EBT-steel sheet surfaces. Int. J. Mach. Tools Manufact. 35, 273-280.

Voyiadjis, G.Z., Deliktas, B., 2009. Formulation of strain gradient plasticity with interface energy in a consistent thermodynamic framework. International Journal of Plasticity 25 (10), 1997–2024.

Wan, Y., Xiong, D.S., 2008. The effect of laser surface texturing on frictional performance of face seal. Journal of Materials Processing Technology 197 (1-3), 96-100.

Wang, H., Zou, M., Jackson, R.L., Larson, P.R., Johnson, M.B., 2010. Nanoindentation modeling of a nanodot-patterned surface on a deformable substrate. International Journal of Solids and Structures 47, 3203-3213.

Wei, Y.G., Wang, X.Z., Zhao, M.H., 2004. Size effect measurement and characterization in nanoindentation test. J. Mater. Res. 19, 208-217.

Wu, P.D., MacEwen, S.R., Lloyd, D.J., Neale, K.W., 2004. Effect of cube texture on sheet metal formability. Mater. Sci. Eng. A 364, 182-187.

Wu, P.D., Neale, K.W., van der Giessen, E., Jain, M., Makinde, A., MacEwen, S.R., 1998. Crystal plasticity forming limit diagram analysis of rolled aluminum sheets. Metall. Mater. Trans. 29A, 527-535.

Xie, H.C., Chen, D.R., Kong, X.M., 1999. An analysis of the three-dimensional surface topography of textured cold-rolled steel sheets, Tribol. Int. 32, 83-87.

Yao, H., Cao, J., 2002. Prediction of forming limit curves using an anisotropic yield function with prestrain induced backstress. Int. J. Plast. 18, 1013-1038.

Zhang, T.Y., Xu, W.H., Zhao, M.H., 2004. The role of plastic deformation of rough surfaces in the size-dependent hardness. Acta Materialia 52, 57-68.

Zhang, Z.L., Hauge, M., Odegard, J., Thaulow, C., 1999. Determining true stress-strain curve from tensile specimens with rectangular cross-section. International Journal of Solids and Structures 36, 3497-3516.

Zhou, R., Cao, J., Wang, Q., J., Meng, F., Zimowski, K., Xia, Z.C., 2011. Effect of EDT surface texturing on tribological behavior of aluminum sheet. Journal of Materials Processing Technology 211, 1643-1649.